INFLUENCE OF MICROSTRUCTURE ON THE METAL DUSTING BEHAVIOUR OF SELF-FLUXING NiCrBSi ALLOYS

Teză destinată obţinerii
titlului ştiinţific de doctor inginer
la
Universitatea Politehnica Timişoara
în domeniul INGINERIA MATERIALELOR
de către

M.Sc. Carsten Strübbe

Conducători ştiinţifici:	prof.univ.dr.ing. Waltraut Brandl prof.univ.dr.ing. Viorel-Aurel Şerban
Referenţi ştiinţifici:	prof.univ.dr.ing. Doina Frunzăverde prof.univ.dr.ing. Ioan Vida-Simiti prof.univ.dr.ing. Ion Mitelea

Ziua susţinerii tezei: 10.02.2015

BUPT

Seriile Teze de doctorat ale UPT sunt:

1. Automatică
2. Chimie
3. Energetică
4. Ingineria Chimică
5. Inginerie Civilă
6. Inginerie Electrică
7. Inginerie Electronică şi Telecomunicaţii
8. Inginerie Industrială
9. Inginerie Mecanică
10. Ştiinţa Calculatoarelor
11. Ştiinţa şi Ingineria Materialelor
12. Ingineria sistemelor
13. Inginerie energetică
14. Calculatoare şi tehnologia informaţiei
15. Ingineria materialelor
16. Inginerie şi Management

Universitatea Politehnica Timişoara a iniţiat seriile de mai sus în scopul diseminării expertizei, cunoştinţelor şi rezultatelor cercetărilor întreprinse în cadrul şcolii doctorale a universităţii. Seriile conţin, potrivit H.B.Ex.S Nr. 14 / 14.07.2006, tezele de doctorat susţinute în universitate începând cu 1 octombrie 2006.

Copyright © Editura Politehnica – Timişoara, 2015

Această publicaţie este supusă prevederilor legii dreptului de autor. Multiplicarea acestei publicaţii, în mod integral sau în parte, traducerea, tipărirea, reutilizarea ilustraţiilor, expunerea, radiodifuzarea, reproducerea pe microfilme sau în orice altă formă este permisă numai cu respectarea prevederilor Legii române a dreptului de autor în vigoare şi permisiunea pentru utilizare obţinută în scris din partea Universităţii Politehnica Timişoara. Toate încălcările acestor drepturi vor fi penalizate potrivit Legii române a drepturilor de autor.

România, 300159 Timişoara, Bd. Republicii 9,
tel. 0256 403823, fax. 0256 403221
e-mail: editura@edipol.upt.ro

BUPT

Foreword

This work was partially supported by the strategic grant POSDRU, Project ID77265 (2010), and co-financed by the European Social Fund – Investing in People, within the Sectoral Operational Programme Human Resources Development 2007-2013.

The present thesis was accomplished through my activities at the Politehnica University of Timişoara, Romania in cooperation with the Westphalian University Gelsenkirchen, Germany.

This scientific work dealt with the morphological study of three differently melted self-fluxing materials considering their suitability under metal dusting conditions.

I would like to express my sincere gratitude to my scientific supervisors for their support in this process. To, Prof. Dr. Eng. Waltraut Brandl, from the Westphalian University Gelsenkirchen, Germany, and also to Prof. Dr. Eng. Viorel-Aurel Şerban from Politehnica University of Timişoara, Romania, for their leadership and inspiration throughout the completion of my PhD thesis.

My deepest gratitude also goes to Dr. Eng. Gabriela Mărginean from the Westphalian University Gelsenkirchen, for her inestimable and unwavering support during the experimental investigations and theoretical considerations.

Likewise, I would like to pay my sincere thanks to my colleague Dr. Eng. Veronica Pirvulescu, for her skill and acumen during the experimental process.

The support of M. Sc. Roxana Muntean, M. Sc. Pascal Dragoş, B. Eng. Petru Valean, Dr. Eng. Ionuţ Secoşan, M. Eng. Markus Kiryc, B. Eng. Mustafa Özbek and B. Eng. Christian Schwabe was also indispensable and vital, for which I am eternally grateful.

Many thanks also go to the general manager of Karl Schumacher GmbH Dipl. Eng. Thomas Conrad, to Dipl. Eng. Hans-Peter Hinz, and of course, to all the other employees involved with the production of the thermal sprayed and flame fused self-fluxing coatings.

I would like to take this opportunity to also thank Dr. Eng. Carmen Opriş, Dr. Eng. Georgiana Melcioiu and Dr. Eng. Ion-Dragoş Uţu from Politehnica University of Timişoara for exceptional handling of organisational matters.

And last but not least, I want to thank my family, especially my wife Monika and my daughter Alicia, for the incredible moral support through the hardest of moments encountered in these last years.

BUPT

Strübbe, Carsten

INFLUENCE OF MICROSTRUCTURE ON THE METAL DUSTING BEHAVIOUR OF SELF-FLUXING NiCrBSi ALLOYS

Teze de doctorat ale UPT, Seria 15, Nr. 15, Editura Politehnica, 2015, 104 pagini, 88 figuri, 7 tabele.

ISSN:2285-1720
ISSN-L:2285-1720
ISBN:978-606-554-915-9

Keywords: self-fluxing alloys, NiCrBSi, metal dusting, carburizing.

Summary,
The present thesis deals with the evaluation of the metal dusting corrosion behaviour of different melted self-fluxing samples. Due to their very dense structure (after the melting process), their oxide forming elements such as Si and Cr, as well as the high amount of Ni, it was presumed that this material class may have a high potential for providing protection of components under metal dusting conditions. Based on these assumptions, thermal sprayed coatings were made by three different self-fluxing feedstock powders and posterior remelted by flame. Furthermore, nuggets of the same powders were manufactured in a vacuum oven or with an inductor. Afterwards, the samples with the highest density were exposed in a $N_2/CO/H_2$ gas mixture in an equimolar ratio at 650°C. The exposed samples were observed, described, and evaluated by means of light microscopy (LM), scanning electron microscopy (SEM) combined with energy dispersive X-ray analysis (EDX), and by X-ray diffraction (XRD). The final purpose was the investigation of the influence of the melting process on the microstructure and finally their metal dusting behaviour.

Rezumat,
În lucrarea de față este prezentată evaluarea comportamentului la coroziune prin carburizare distructivă a unor aliaje autofluxante topite prin diferite metode, care nu au mai fost investigate până în prezent sub aceste condiții.
Datorită structurii foarte dense, obținute după procesul de topire, a elementelor formatoare de oxizi (Si și Cr), precum și a cantității ridicate de Ni, s-a presupus că această clasă de materiale poate avea un potențial ridicat de a oferi protecție componentelor supuse carburării distructive. Bazat pe aceste ipoteze, au fost depuse straturi de acoperire prin pulverizare termică, utilizând ca materie primă trei tipuri de pulbere autofluxantă, care ulterior au fost retopite cu flacără. Aceleași pulberi au fost topite în cuptorul cu vid, respectiv prin inducție obținând probe cu aspect de pepită. Etapa următoare a constat în selectarea probelor cu structura cea mai densă în vederea expunerii într-un amestec de gaz $N_2/CO/H_2$ la temperatura de 650°C. Probele astfel testate au fost analizate și evaluate prin intermediul Microscopiei Optice (LM), al Microscopiei Electronice cu Baleiaj (SEM) combinată cu Spectroscopia de Energie Dispersivă (EDX) și prin Difracție de Raze X (XRD). Scopul final a constat în investigarea influenței procesului de topire asupra microstructurii aliajelor autofluxante de tip NiCrBSi, precum și asupra comportamentului acestora la carburare distructivă. Toate aceste rezultate şi informaţii au fost documentate astfel încât să poată fi folosite ca o bază de cunoştinţe pentru cercetări și aplicații viitoare.

BUPT

Content

List of figures **7**

List of tables **11**

1. INTRODUCTION **12**

1.1. Background 12

1.2. Aim of the Work 13

2. STATE OF THE ART **14**

2.1. Definition of Metal Dusting (MD) 14

2.2. Metal Dusting Mechanism 15

2.3. The Role of Alloying Elements in Ni based Alloys 18

2.4. Ni based Alloys under Metal Dusting Conditions 20

2.5. Increase of the Lifetime of Ni based Alloys under MD Conditions 22

2.6. Coatings for the Improvement of the Metal Dusting Resistance 28

2.7. Thermal Sprayed Self-Fluxing Coatings 29

2.7.1. The Complex Phase Structure of Self-Fluxing Materials 32

2.7.2. Critical Consideration 34

2.8. Motivation 35

3. METHODOLOGY **36**

3.1. Light Microscopy (LM) 36

3.2. Scanning Electron Microscopy (SEM) 37

3.3. X-ray Diffraction (XRD) 38

3.4. Colour Etching 39

3.5. UV Emission Spectroscopy (UVS) 40

3.6. X-ray Fluorescence Spectrometry (XRF) 40

3.7. Differential Thermal Analysis (DTA) 40

3.8. Thermocouple Measurement 41
3.9. Microindentation 41
3.10. Exposure to Metal Dusting in the Corrosion Test Rig 41
4. EXPERIMENTS 45
4.1. Materials Selection 45
4.2. Sample Manufacturing and Process Parameters 46
4.2.1. Thermal Sprayed and Flame Fused Self-Fluxing Samples 46
4.2.2. Vacuum Oven Melted Self-Fluxing Samples 47
4.2.3. Inductively Melted Self-Fluxing Samples 52
4.3. Exposure in the HT Corrosion Test Rig 55
5. RESULTS AND DISCUSSION 56
5.1. Morphology, Chemical and Physical Properties of the Materials 56
5.1.1. Self-Fluxing Feedstock Powders 56
5.1.2. Thermal Sprayed and Flame Fused Coatings 60
5.1.3. Vacuum Melted Samples 62
5.1.4. Inductively Melted Samples 64
5.1.5. Influence of the Melting Process on the Obtained Structure 67
5.2. Morphology and Structure of the Exposed Samples 69
5.2.1. Samples after 500 h of Exposure to Metal Dusting Conditions 69
5.2.2. Samples after 1000 h of Exposure to Metal Dusting Conditions 72
6. CONCLUSIONS AND OUTLOOK 80
6.1. Conclusions 80
6.2. Outlook 82
References 83
List of Publications 88
Appendix 89

BUPT

List of figures

Figure 2.1: Schematic presentation of the metal dusting mechanism of iron and low-alloy steels by Grabke [45] 16
Figure 2.2: SEM (scanning electron microscopy) image of C whiskers with metallic particles, which are visible as white spots at the end of the C whiskers [27]..... 16
Figure 2.3: Mass gain kinetics for Fe–Ni alloys in flowing 50%H_2-50%CO at 650°C; left [26] and in a 25%CO–25%H_2–0.5%H_2O–49.5%Ar gas at 650°C 17
Figure 2.4: The phase structure of iron 18
Figure 2.5: Mass loss rate versus exposure time for alloy samples exposed to CO-20% H_2 at 621°C [34] 21
Figure 2.6: Maximum pit depth measurements for alloy samples exposed to CO-20% H_2 at 621°C [34] 22
Figure 2.7: Ellingham-Richardson diagram for some oxidation reactions [48] 23
Figure 2.8: Wagner´s model of the parabolic oxide scale growth for metal oxides. 24
Figure 2.9: Some parabolic oxidation constants k_p in dependence of the temperature [29] 26
Figure 2.10: Schematic representation of the metal dusting prevention technique [55] 27
Figure 2.11: Binary phase diagram of Ni-Si [72] 30
Figure 2.12: Binary phase diagram of Ni-B [72] 30
Figure 2.13: Schematic representation of thermal sprayed coatings 31
Figure 2.14: Ni-Cr-B liquidus projection [82] 32
Figure 2.15: XRD analysis of the powder NiCrBSi [72] 33
Figure 3.1 Schematic presentation of the function mode of a light microscope 36
Figure 3.2: Scheme of a Scanning Electron Microscope 37
Figure 3.3: Schematic representation of diffraction of X-rays in a crystalline material 38
Figure 3.4: Schematic structure of the UV spectrometer from the company Spectro Ametek 40
Figure 3.5: Open voltage circuit; e_{AB}= Seebeck voltage 41
Figure 3.6: Schematic representation (CAD) of the high temperature test rig 42
Figure 3.7: Function block diagram of the HT test rig 42

BUPT

8 List of figures

Figure 3.8: Graphical user interface 1 of the HT test rig 43
Figure 3.9: The second graphical user interface of the HT test rig 43
Figure 3.10: Schematic representation (CAD) of the oven with 44
the quartz glass reactor 44
Figure 3.11: The Kovar connection (left) and its placement on the 44
reactor at the outlet side of the high temperature oven (right) 44
Figure 4.1: Overview experimental plan 45
Figure 4.2: Schematic representation of thermal powder flame spraying process .. 46
Figure 4.3: LM micrographs of the 15E thermal sprayed coating before (left) and . 47
after the flame fusing process (right) 47
Figure 4.4: Ceramic crucible, refractory-lined with a glass fiber 48
mat (left) and sealed ceramic crucible with the powder (right) 48
Figure 4.5: DTA-curves of the feedstock powders tested 48
Figure 4.6: Screenshot of the graphic display of the written program (test run) 49
Figure 4.7: Control protocol for the exposure of the 15E sample in the vacuum oven 49
Figure 4.8: Section of the control protocol with the parabolic cooling curve 50
Figure 4.9: LM micrograph used for porosity measurement; the pores are colored blue 51
Figure 4.10: Induction heating system 52
Figure 4.11: Schematic representation of the fundamentals of induction heating [4] 53
Figure 5.1: SEM micrograph powder 15E 57
Figure 5.2: SEM micrograph powder 18C 57
Figure 5.3: SEM micrograph powder 19E 57
Figure 5.5: Cross section of the powder 18C 58
Figure 5.4: Cross section of the powder 15E 58
Figure 5.7: EDX analysis of the powder 19E 58
Figure 5.6: Cross section of the powder 19E 58
Figure 5.8: XRD pattern for the powder 15E 59
Figure 5.9: Quantification charts of the three powders 15E, 18C and 19E 59
Figure 5.11: Structure of the thermal sprayed and flame fused 18C coating (SEM) 60
Figure 5.10: Structure of the thermal sprayed and flame fused 15E coating (SEM) 60
Figure 5.12: Structure of the thermal sprayed 60

BUPT

and flame fused 19E coating (SEM) 60
Figure 5.13: EDX analysis of the light grey phases from the thermal sprayed and . 60
flame fused sample 19E..... 60
Figure 5.14: Quantification charts of the three thermal sprayed and flame fused coatings..... 61
Figure 5.15: Structure of the vacuum melted sample 15E 62
Figure 5.16: Structure of the vacuum melted sample 18C..... 62
Figure 5.17: Structure of the vacuum 62
melted sample 19E 62
Figure 5.18: Quantification charts of the vacuum melted nuggets 63
Figure 5.20: Structure of the inductively melted sample 18C..... 64
Figure 5.19: Structure of the inductively melted sample 15E..... 64
Figure 5.21: Structure of the inductively melted sample 19E..... 64
Figure 5.22: Star-shaped structure of the inductively melted sample 18C (mapping) 65
Figure 5.23: Binary phase diagram of the system Cr/Mo 66
Figure 5.24: Quantification charts of the inductively melted nuggets 66
Figure 5.25: Overview of the obtained structures..... 67
Figure 5.26: View in the glass reactor of the HT test rig after the..... 69
exposure of the samples to metal dusting conditions 69
Figure 5.27: Overview of the macroscopic examinations of the samples after 500 hours of exposure to metal dusting conditions 70
Figure 5.28: Cross section of the vacuum melted sample 15E after 500 hours exposure to metal dusting conditions 70
Figure 5.29: Cross section of the flame fused sample 18C after 500 hours exposure to metal dusting conditions 70
Figure 5.30: Iron nail after 500 hours of exposure to metal dusting conditions 71
Figure 5.32: EDX-analysis of the oxide scale formed on the flame fused 18C sample after 500 hours exposure to metal dusting conditions..... 71
Figure 5.31: Cross section of the flame fused 18C sample after 500 hours exposure to metal dusting conditions 71
Figure 5.33: Cross section SEM micrograph of the flame fused 15E sample after 500 hours exposure to metal dusting conditions..... 72

BUPT

Figure 5.34: EDX analyses 1 and 2 of the oxide scale grown on of the flame fused 15E sample after 500 hours exposure to metal dusting conditions..... 72
Figure 5.35: Overview of the macroscopic examinations of the samples after 1000 hours of exposure to metal dusting conditions 73
Figure 5.36: Cross section of the sample 18C, thermal sprayed and 73
remelted with flame after 1000 hours under MD conditions 73
Figure 5.38: Cross section SEM micrograph of the flame fused sample 19E after 1000 h of exposure to MD conditions..... 74
Figure 5.37: Cross section SEM micrograph..... 74
of the vacuum melted sample 15E after..... 74
1000 hours exposure to MD conditions 74
Figure 5.40: Cross section SEM micrograph of the inductively melted sample 18C after 1000 hours of exposure to metal dusting conditions 74
Figure 5.39: SEM micrograph of the star-shaped structure of the sample 18C, melted with an inductor 74
Figure 5.41: Cross section SEM micrograph of the flame fused sample 75
15E after 1000 hours of exposure to metal dusting conditions 75
Figure 5.42: Cross section SEM micrograph of the flame fused sample 15E after 1000 hours of exposure to metal dusting conditions, observed at a magnification of 500x (left) and 2500x (right) 75
Figure 5.43: Section of a Cr-Si phase diagram..... 76
Figure 5.44: LM micrograph of a color etched sample with the hardness indentation A and B on it 77
Figure 5.46: EDX-analysis 2 of the brown, color etched phases 77
Figure 5.45: EDX-analysis 1 of the brown, color etched phases 77
Figure 5.47: EDX-analysis 3 of the light grey matrix..... 77
Figure 5.48: EDX-analysis 4 of the dark grey round shaped particles..... 78
Figure 5.50: LM micrograph of the color etched vacuum oven melted sample 15E. 78
Figure 5.49: LM micrograph of the color etched flame fused sample 15E..... 78
Figure 5.51: LM micrograph of the inductively melted color etched sample 18C 79

BUPT

List of tables

Table 2.1: Chemical composition of Ni based alloys, tested under metal dusting conditions 20
Table 2.2: Oxide-metal volume ratios of some common metals [40,59] 26
Table 4.1: Chemical composition (mass%) of the self-fluxing alloys tested 45
Table 4.2: Parameters and results of the vacuum melting tests 51
Table 4.3: Parameters of the inductive melting process and the degree of internal porosity of the obtained samples 54
Table 4.4: Parameters for the exposure of the samples in the HT test rig 55
Table 5.1: Chemical composition of the self-fluxing feedstock powders used, determined by means of XRF 56

BUPT

1. INTRODUCTION

1.1. Background

Metal dusting (MD) is a corrosion phenomenon of Fe, Ni- and Co based alloys in carbon supersaturated atmospheres at medium temperatures. The corrosion attack, which is very often encountered in chemical and petrochemical industries, results in localized pitting and/or general overall surface wastage with metal particles, or carbide particles, and coke as the byproducts of the corrosion reaction.
Metal dusting causes $1.3 billion in costs per year worldwide for the replacement of damaged components. Most of these replacements are made using of cheaper steels, and are conducted at regular intervals in different industrial areas [1]. Alvarez [2] refers to a statement from the US Department of Energy, which states "…savings up to $290 million per year could be obtained if metal dusting is eliminated in the production of hydrogen". Due to this reason, researchers from all over the world are searching for methods to prevent the metal dusting attack, or at least to extend the lifetime of components in such environments. One of the most promising discovery was the use of special Ni based alloys. Due to the lower diffusivity as well as the low solubility of carbon in nickel, Ni based alloys have a higher resistance against metal dusting and therefore a longer lifetime, in comparison with Fe based alloys. Furthermore, the special Ni based alloys are able to form a dense, adherent, free from defects, and stable oxide scale on the surface of the component, using the remaining oxygen from the atmosphere. The scientists reported promising results up until the moment the protective oxide scale failed. In such a situation, also the Ni based material was carburized, especially along grain boundaries and defects in the austenite or more intensively along pores and cracks in Ni based coatings from where the metal dusting attack typically starts [3]. This has been proven by many studies. This approach was also included in the scope of this work.
The main idea deals with the selection of dense Ni based self-fluxing coatings for the protection of components under MD conditions. Out of the most common Ni based self-fluxing alloys, namely NiCrBSi, which are focused on in this work, Ni is the most corrosion resistant component at higher temperatures and provides high mechanical strength, and excellent stability [4]. The addition of Si and B gives them the "self-fluxing" characteristic, and together they reduce the melting interval [4,5]. In some cases, depending on the field of application, Ni has to be substituted with Co or Fe [6]. Co based self-fluxing alloys provide the highest temperature resistance. According to Cheng [7], the Fe based alloys are the most cost-efficient option, especially for protection against oxidation at lower temperatures and for aqueous corrosion resistance.
The most common technique to deposit the self-fluxing feedstock powders onto components is the flame spraying (FS). This thermal spray process leads to a very poor coating quality. As such, after the application process, it is necessary to subject the coating to a post-treatment fusing, which can be done either with an oxyacetylene flame, in a vacuum oven, or with an inductor. These are typical processes in the industry and therefore were used in this work. Such thermal sprayed and fused coatings exhibit an almost completely dense structure.

1.2. Aim of the Work

The NiCrBSi alloys have already been extensively studied with respect to their wear resistance [4–6,8], and also their aqueous corrosion resistance [7,9–11] in mineral acid solutions, including oxidizing acids [6]. However, self-fluxing alloys have never been investigated under metal dusting conditions. Due to their very dense structure (after the fusing process), their oxide forming elements such as Si and Cr, as well as the high amount of Ni, it was presumed that this material class may have a high potential for special applications such as providing protection of components under metal dusting conditions. Based on these assumptions, thermal sprayed and subsequently fused, as well as vacuum- and inductively melted self-fluxing alloys were manufactured of three different self-fluxing feedstock powders. The samples were exposed in a $N_2/CO/H_2$ gas mixture in a ratio of 80:10:10 (vol%) at 650°C. According to the literature, it is indeed the most aggressive atmosphere and generally generates metal dusting after a short exposure time. The aim of the work was the evaluation of the microstructure after the different post-treatment fusing processes and its influence on the metal dusting behaviour.

BUPT

2. STATE OF THE ART

2.1. Definition of Metal Dusting (MD)

After reviewing the damage analysis of a blast furnace in 1869, Mr. Lowthian Bell [12] noted that iron catalyzes the deposition of carbon from carbon monoxide gas. Seven years later, Mr. Pattinson [13] confirmed this theory. He claimed that small amounts of iron in furnace bricks led to a carbon deposition and finally to the disintegration of the bricks. Furthermore, he described his observation regarding the reaction of carbon with pig iron in the blast furnace as follows: "It is marvelous to consider how this action has succeeded in disintegrating, probably large pieces of metal (Cleveland pig iron), gradually lifting the particles of iron farther and farther away from their original position, and distributing them amongst the large masses of accumulated carbon" [13]. This was one of the first public documentations which addressed the metal dusting phenomenon, today much better understood. In the literature, several contradictory statements exist regarding when the term "metal dusting" was used for the first time. Al-Meshari [14] asserted in his dissertation that the term "metal dusting" was first used in the late 1950s or early 1960s. Taking other statements into account, this statement can be disputed. Mr. Szakalos referred in a patent from 2003 [15] and in his doctoral thesis [16] that the term "metal dusting" was actually mentioned by E. Camp and co-workers as early as 1945 [17]. The phenomenon "metal dusting" was first detected in a superheater for reforming naphtha. In this period, the term "metal dusting" was used to describe the phenomenon associated with hydrocarbon processing. Butane dehydrogenation plant personnel noted how iron oxide and coke radiated outward through catalyst particles from a metal contaminant, which acted as a nucleating point. The metal had deteriorated and appeared to have turned into dust. The phenomenon has been referred to as "catastrophic carburization" and "metal deterioration in high temperature carbonaceous environment", but the term most commonly used today is **metal dusting** [18].

Currently, there is not a uniform definition of metal dusting. That is precisely the reason why scientists are using different methods to define the metal dusting phenomenon. The definitions of all authors can be classified into two groups. One part of the scientists describe the metal dusting mechanism as a catastrophic corrosion of Fe-, Ni- and Co based alloys in carbon supersaturated or strongly carburizing atmospheres at 400 °C to 800°C [19–23].

The other part of the scientists [24–28] use the expression "catastrophic carburization" without mentioning the temperature range. Both definitions comprise metal or carbide particles and coke as the products of the reaction under metal dusting conditions.

BUPT

2.2. Metal Dusting Mechanism

The metal dusting mechanism can be classified into two types. The first one concerns pure iron and Fe based alloys. The second one relates to the reaction of Ni, Co and their alloys. Source states [14,29] that, the process of metal dusting for iron was first researched by Hochman [30,31] in 1969. Later, Grabke and co-workers [27,29] exhaustively studied the process for Ni, Co and their alloys. In general, metal dusting can lead to a disintegration of metals and alloys into a dust of fine metallic particles, graphite, or carbon [14,26–28,32–39] and/or oxide particles [14]. The condition for metal dusting to occur is a supersaturated atmosphere, containing CO and/or hydrocarbons [37]. That means the thermodynamic activity of carbon in the atmosphere, which can be calculated by the use of thermodynamic calculation programs, is greater than 1 (a_c>1). At carbon activities <1, a structural change will occur without a disintegration of the material [40].
Metal dusting of steels and Ni based alloys is often encountered in CO containing syngas environments with a low oxygen potential (pO_2). The metal dusting process in this atmosphere starts with the formation of carbon. According to Grabke et al. [26,27,37,41], the main carbon formation reactions from carbon monoxide, the most potent metal dusting molecule [42], are a) the reduction of CO by hydrogen (reduction reaction) and b) the decomposition of CO (Boudouard reaction).

a) Reduction reaction: $\mathrm{CO + H_2 \leftrightarrow H_2O + C}$ (Eq. 2.1)

b) Boudouard reaction: $\mathrm{2CO \leftrightarrow CO_2 + C}$ (Eq. 2.2)

Both reactions begin with the breakdown of carbon monoxide molecule. For the separation of carbon from carbon monoxide, the chemical bond between carbon and oxygen must be broken. Usually, CO is a relatively stable molecule at 650°C [43]. However, in the presence of catalysts, such as the transition metals Fe, Co or Ni, the electrons can be shifted from filled d-metal orbitals to the CO antibonding orbital (∏ molecular orbital). Thereby, the chemical bond in the CO molecule is weakened by electron delocalization and the energy needed for dissociation and activation will be decreased [44].
The electron distribution of Fe, Co and Ni is outlined below:

Fe: $1s^2\ 2s^2p^6\ 3s^2p^6\ 4s^2\ 3d^6$

Co: $1s^2\ 2s^2p^6\ 3s^2p^6\ 4s^2\ 3d^7$

Ni: $1s^2\ 2s^2p^6\ 3s^2p^6\ 4s^2\ 3d^8$

BUPT

With regards to the reduction reaction Grabke et al. proposed a metal dusting mechanism of iron and low alloy steels, which is schematically presented in the following figure.

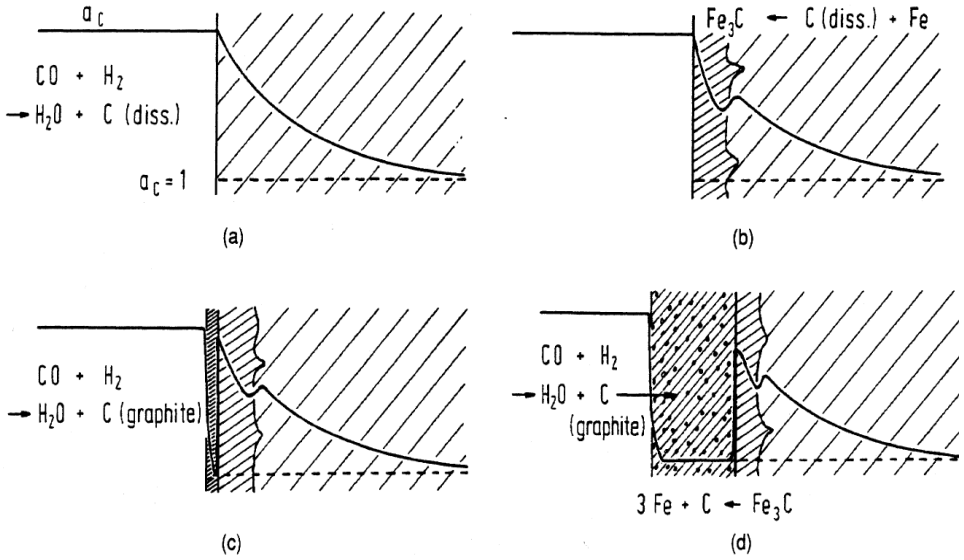

Figure 2.1: Schematic presentation of the metal dusting mechanism of iron and low-alloy steels by Grabke [45]

The metal dusting process starts with (a) the supersaturation of the metal matrix by carburization. In the next step (b), the formation of Fe_3C at the surface takes place with growth from inside out. The result is (c) a deposition of graphite onto the Fe_3C surface. This oversaturation of C in Fe_3C leads to (d) the cementite decomposition (according to the reaction $Fe_3C \rightarrow 3Fe + C$) into pure metal particles and graphite. The diffusion velocity of carbon in cementite is slow. For this reason, the carbon causes an outgrowth of coke, during which the metallic iron particles diffuse through the graphite lattice structure. This leads to the formation of nanometric carbon fibrils [14,32] with metallic particles [27] (see Fig. 2.2) on the surface which "then strongly catalyze further carbon deposition" [34]. The process then repeats itself from the first step, but with much higher rates [27].

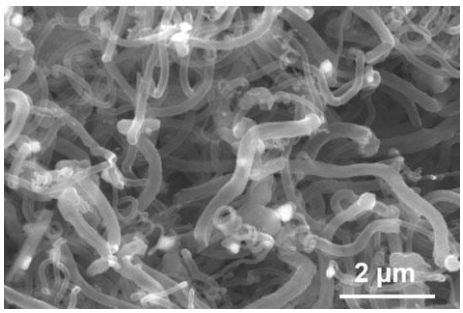

Figure 2.2: SEM (scanning electron microscopy) image of C whiskers with metallic particles, which are visible as white spots at the end of the C whiskers [27]

BUPT

It is a well-known fact that the metal dusting mechanism for Ni based alloys is similar to that of Co based alloys [46]. Ni and Co do not form carbides, because they are unstable by nature [27]. It is supposed that there is a direct inward growth of graphite in the bulk material. It is also known that the filaments of graphite for Ni and Ni based alloys are bigger than those of iron [26]. Furthermore, the disintegration of Ni and Ni based alloys leads to larger metallic particles, whereas the carbon deposition and the metal wastage are lower [46]. Grabke et al. [26] also indicate that the larger the metal particles are, the less catalytically active they are for carbon deposition. In this work Grabke et al. investigated the mass gain in mg/cm² as an indicator for the metal dusting mechanism of several Fe-Ni alloys. He confirmed the theory that the metal dusting resistance depends on the Fe/Ni ratio. The higher the Ni content in the alloys, the lower the initial rate of carbon uptake (mass gain) in a H_2/CO atmosphere at 650°C (see Fig. 2.3, left).
In addition to Grabke et al., Zhang and Young [47] studied eight Fe-Ni alloys in CO–H_2–H_2O–Ar gas, corresponding to a_C = 19.6, in a tube furnace at 650°C. For this purpose, they prepared Fe–5Ni, Fe–10Ni, Fe–20Ni, Fe–40Ni, Fe–60Ni, Fe–70Ni, Fe–80Ni, and Fe–90Ni (compositions in mass%). Before the reaction started, the rectangular samples (14 x 7 x 1.5 mm) were annealed for 24 hours at 1000°C in 5% H_2 in Ar. Afterwards, the samples were ground with 1200-grit SiC-sandpaper, polished to 3 µm, and ultrasonically cleaned in acetone before exposing. These results showed that the carbon uptake decreased with relation to increased nickel content (see Fig. 2.3, right [47]).

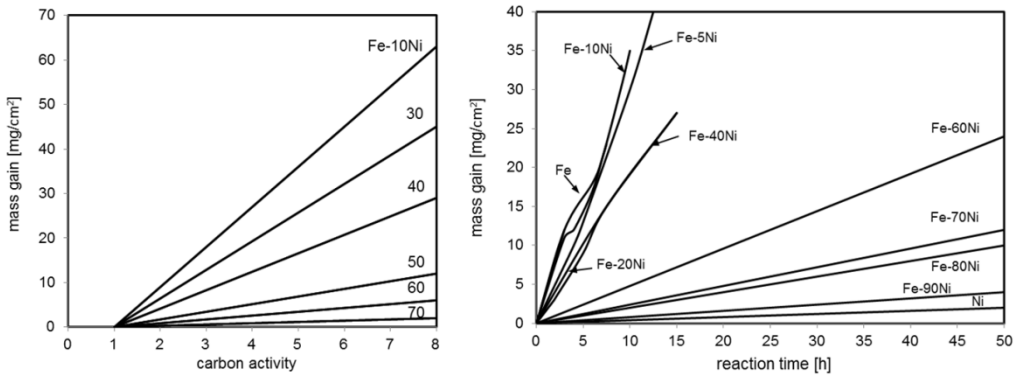

Figure 2.3: Mass gain kinetics for Fe–Ni alloys in flowing 50%H_2-50%CO at 650°C; left [26] and in a 25%CO–25%H_2–0.5%H_2O–49.5%Ar gas at 650°C

A uniform Fe_3C scale was detected on pure iron. The layer of Fe–5Ni consisted of Fe_3C, γ and α-Fe, whereas the layer of Fe–10Ni had only "small amounts of Fe_3C developed at the surface of an austenite layer grown on two-phase (α + γ)". For alloys with more than 10 mass% of nickel, no carbides were detected.

The higher metal dusting resistance can be attributed to the lower solubility and diffusivity of carbon in nickel, in comparison to iron [48]. This resulted in a higher packing density of Ni, which keeps a face-centered cubic (fcc) lattice structure up to its melting point of 1455°C [40]. Fe, in contrast, has a body-centered structure (bcc) from room temperature up to 911°C or over 1392°C [49] (see Fig. 2.4). However, under certain operational conditions, dependent on the temperature, time,

BUPT

and surroundings, Ni is also susceptible. For that purpose, the potential of Ni can be optimized through alloying. The general effects of the alloying elements in Ni based materials are the content of the following chapter.

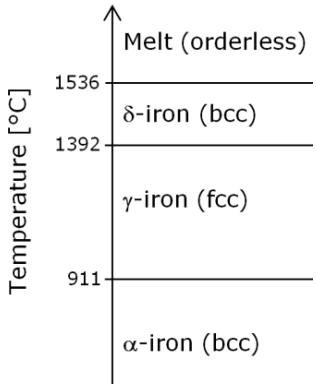

Figure 2.4: The phase structure of iron

2.3. The Role of Alloying Elements in Ni based Alloys

Through the addition of different elements, Ni based alloys provide the most favorable combination of mechanical properties, corrosion resistance, and machinability of all the high temperature (>500°C [40]) metal alloys (e.g. Co- and Fe- based alloys [40,50]). Therefore, the research concerning the material's resistance to metal dusting focused mainly on Ni based alloys. Ni based alloys are defined as those with more than 50 mass% Ni [49]. There are many Ni based alloys existing in the world today. The Special Metals Corporation of West Virginia (USA), established in 1906, is the only company currently producing more than a hundred Ni based alloys, including the well-known Ni based alloy products: INCONEL®, INCOLOY®, MONEL®, NILO®, NILOMAG® NIMONIC®, BRIGHTRAY®, DURANICKEL®, UDIMET® and UDIMAR® [51]. This class of Ni based materials has remarkable high temperature strength, toughness, and resistance to corrosive or oxidizing environments. According to feasibility (costs, handling, machining, etc.), and as per the maxim "no more than necessary", in order to optimize efficiency, different Ni based superalloys of varying alloy compositions are used in the industry (e.g. to raise the efficiency of gas turbine components in aircrafts and in power plants). These Ni based superalloys contain up to ten other elements [52].
Bürgel [40] summarized the influences of many elements and their general positive (+) and negative (-) effects on Ni based materials. It should be noted that these values for the maximum alloying contents are in reference to the Ni based alloy production standards of 2006. Hence, there are some differences between the values reported by Bürgel and those of currently used Ni based alloys. This work also comprises newly developed high temperature Ni based alloys (e.g. INCONEL® alloy 671, 690, 693 and Sumitomo® 696).

BUPT

Fe (up to 39 mass%)
\+ Fe is very cheap; Ni in Ni-Fe-basis wrought alloys will be partly substituted through Fe for applications at medium temperatures.
\- Higher Fe contents lower the oxidation resistance.

Cr (up to 46 mass%)
\+ Able to form a dense Cr_2O_3 for the protection against corrosion
\+ Carbide former, mainly $M_{23}C_6$
\+ Solid hardening solution

Co (up to 20 mass%)
\+ Improves the creep strength at median temperatures
\+ Solid hardening solution
\- Can reduce the phase stability

Mo (up to 14 mass%)
\+ Increases the E-module (positive for the creep strength)
\+ Solid solution hardening (strong covalent bond to Ni)
\+ Reduces the diffusion
\+ Carbide former, mainly M_6C
\- Can reduce the oxidation- and hot-gas corrosion stability

W (up to 14 mass%)
\- The same effect as Mo
\- Strongly dendritical segregation; cannot be completely compensated
\- Increases the density

Ta (up to 12 mass%)
\+ Solid hardening solution (strong covalent bond with Ni)
\+ Reduces the growth rate of the Al_2O_3-oxide layer
\+ Improves the cyclic oxidation resistance
\- Increases the density

Al (up to 6 mass%)
\+ γ´-formation (Ni_3Al) and β-formation (NiAl)
\+ Formation of Al_2O_3 for the protection against further oxidation, also >950°C
\+ Strong solid hardening solution (strong covalent bond with Ni in Ni_3Al and NiAl)
\- Higher Al-contents cause the phase stability to become poorer, because more Ni is used in γ´ and therefore the Ni-content in the matrix decreases

Nb (up to 5 mass%)
\+ Solid hardening solution
\- Higher contents can lead to embrittlement (Ni_3Nb-plates)
\- Can reduce the oxidation resistance

Ti (up to 5 mass%)
\+ Al in γ´ will be substituted through Ti
\- Formation of the brittle η-phase Ni_3Ti

Si (up to 1 mass%)
\+ Improves the oxidation- and hot-gas corrosion stability, mostly used in coatings
\- Reduces the solidus temperature

BUPT

C (up to 0.18 mass%)
\+ Carbide former
\- Reduces the solidus temperature

B (up to 0.03 mass%)
\+ Increases the ductility and the creep rupture strength
\+ Boride-forming (instead of carbides)
\- Reduces the solidus temperature

2.4. Ni based Alloys under Metal Dusting Conditions

Numerous of the actual Ni based alloys were already tested under metal dusting conditions by many scientists including Grabke, Ramanarayanan, and Nishiyama, to name a few. The tests were carried out in the laboratory and as field tests over days, weeks, months and years with/without pre- and post-treatments in different environments with varied oxygen partial pressure and gas flow rates at different temperatures. Some of these Ni based alloys (see Tab. 2.1) are described in this chapter, in order to illustrate the above outlined elements under metal dusting conditions.

Table 2.1: Chemical composition of Ni based alloys, tested under metal dusting conditions

Alloy	Ni	Cr	Fe	Mn	Si	Al	Cu	Ti	C	Y	Nb	Mo	Co
INCONEL ® 600	73,8	15,5	8	1,5	/	0,3	0,5	0,3	0,1	/	/	/	/
INCONEL ® 601	58,7	25	13	0,2	0,5	1,7	0,5	0,3	0,1	/	/	/	/
Nicrofer ® 602	60,5	25	10,5	0,5	0,5	2,4	0,1	0,2	0,2	0,1	/	/	/
INCONEL ® 617	50,7	21,5	2	1	0,7	1	0,5	0,5	0,1	/	/	9	13
INCONEL ® 671	53,4	46	/	/	/	0,3	/	0,3	0,03	/	/	/	/
INCONEL ® 690	60,5	29	9	0,5	0,5	/	0,5	/	0,05	/	/	/	/
INCONEL ® 693	62,1	29	4	/	0,3	3,1	/	/	0,02	/	1,5	/	/
Sumitomo ® 696	58	30	4	1	2	/	2	1	0,08	/	/	2	/

The two Ni based alloys 601 (UNS N6601) and 602 (UNS N6025) are often used for waste heat boiler shells, tubes in ammonia plants, and for reformer components in order to decrease the time of nonuse and repair costs. Many scientists studied these alloys under metal dusting conditions.
Brandl et al. [32] studied these uncoated samples in metal dusting experiments at 700°C. For that, the samples were periodically removed out of the hot zone of the test device and were sprayed every 30 minutes with a special fuel oil, in order to simulate flame heaters. After 850 hours, both Ni based samples showed local attacks. The alloy 601 showed more pitting than the 602, which is the main indicator for metal dusting.

BUPT

The same corrosion behavior was detected by Grabke et al. [28] for the alloy 601 with 49 mass% CO, 49 mass% H_2, and 2 mass% H_2O at 650°C after 1993 hours. He suggested that the pits were probably initiated by small defects in the oxide scale.
Walmsley et al. [50] found out that the exposure of alloy 601 in a commercial methanol plant at 540°C led to the formation of a coherent nanometer scale $M_{23}C_6$ and a coarser M_7C_3 under the surface. Hence, the alloy 601 was also destroyed in this case. The carbides were Cr rich and may contain Fe. Due to increasing carbon content for thermodynamically stable carbides, the accepted sequence of formation is as follows:

$$M_{23}C_6 < M_7C_3 < M_3C_2 < \text{graphite [50]}.$$

Grabke et al. [26] stated that the carbides $M_{23}C_6$, M_7C_3, and MC are oxidized through the formation of spinels. This often results in defects and other oxides, when the metal matrix of high alloy steels and Ni based alloys are disintegrated by metal dusting.
For a better protection against metal dusting under the harshest conditions, alloys such as INCONEL® alloy 617, 671, 690, or the new developed INCONEL® alloy 693 (UNS N06693), from the world leading Special Metals Corporation mentioned above, offer a higher potential as an upgrade from the commonly used alloy 601 [34]. The INCONEL® alloy 671, for example, is especially used in petroleum industry [53]. In the nuclear industry, the INCONEL® alloy 690, commonly used as heat exchanger tubing, has proven to be successful [41]. These alloys provide a combination of high temperature strength, as well as resistance to a wider range of corrosive environments, in contrast to alloy 601 and 602, respectively [54].
Baker et al. [34,41] confirmed this as well. They studied a large number of high alloyed steels and Ni based materials for up to 14,000 hours in CO-20% H_2 at 621°C. Baker discovered that INCONEL® alloy 671 and alloy 693, which contain the highest total amount of Cr and Al, showed the best performance with regards to resistance against mass loss rate (Fig. 2.5) and pitting (Fig. 2.6).

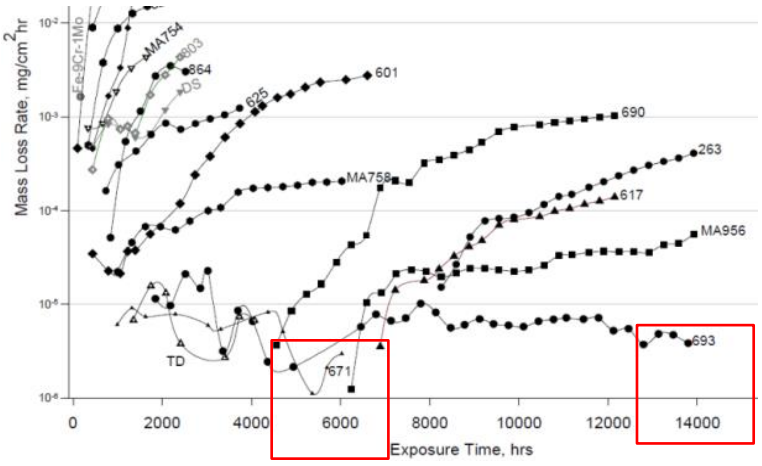

Figure 2.5: Mass loss rate versus exposure time for alloy samples exposed to CO-20% H_2 at 621°C [34]

BUPT

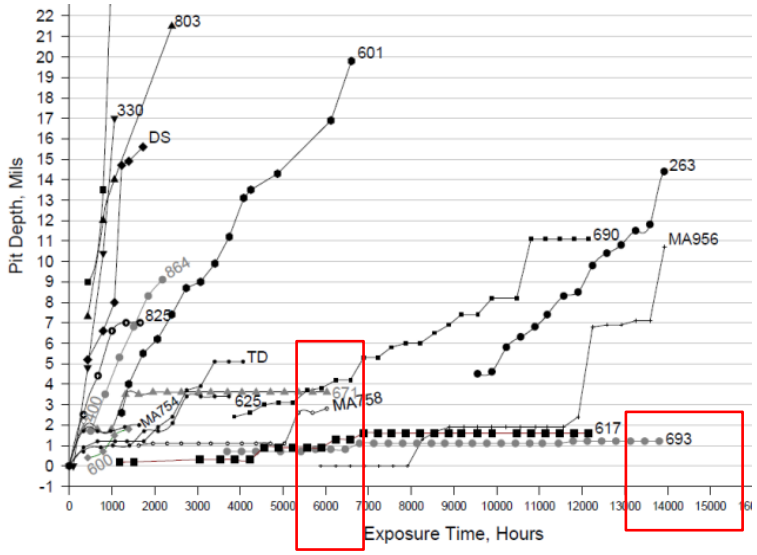

Figure 2.6: Maximum pit depth measurements for alloy samples exposed to CO-20% H_2 at 621°C [34]

Similar results were achieved by Nishiyama et al. [55]. In this work, thermocyclic long term tests were conducted for several Fe- and Ni based materials. The alloys were heated up to 650°C for 50 hours and cooled down to 100°C in the span of 5 hours. A stage followed, in which the temperature was held at 100°C for 30 minutes in 60 vol% CO, 26% H_2, 11.5% CO_2 and 2.5% H_2O. The calculated carbon activity was 10 and the oxygen partial pressure was 4.6×10^{-26} MPa. The alloys 601 and 602 already showed pits after 200 hours (4 heating and cooling cycles) and 500 hours (10 heating and cooling cycles), respectively. Pits formed in alloy 693 at 2,000 hours and at 13,000 hours for the alloy 690. However, the final mass loss rate of the alloy 690 was higher than that of the alloy 693. In the same work, Nishiyama et al. compared these alloys with the new Ni based superalloy Sumitomo 696 (N06696), developed by Sumitomo Metal Industries, Ltd. (Osaka, Japan). Even after 22,000 hours exposure in the environment outlined above, the alloy 696 had no pits on its surface. The results of this study show that this new Ni based superalloy, Sumitomo 696, is currently the Ni based superalloy with the highest metal dusting resistance. This will be discussed later in detail.
As aforementioned, the reason for the different behaviour of the Ni based alloys with a similar Ni content is related to the influence of the alloying elements. The function of the alloying elements for the protection of Ni based alloys under metal dusting conditions is presented in the following chapter.

2.5. Increase of the Lifetime of Ni based Alloys under MD Conditions

Referring to the American Society for Metals and known as DIN EN ISO 8044:1999 in Germany, corrosion is generally defined as a chemical or electrochemical reaction between a material, usually a metal, and its environment, which produces a

BUPT

deterioration of the material and its properties. In the world of material sciences, it is known that the corrosion of metals and alloys can never be stopped completely. Due to this reason, there is a replacement of the corroded components resulting from regular periodical inspections and preventive checks.
Metal dusting is attributed to high temperature corrosion in the literature and cannot be completely prevented. However, the lifetime of components can be significantly increased through the proper use of Ni based alloys. As mentioned before, Ni based alloys have, on one hand, a good resistance to metal dusting due to their low carbon diffusivity and solubility in nickel. On the other hand, they have certain susceptibilities. As such, some elements are able to increase the lifetime of Ni based materials under metal dusting conditions. The protection of the concerned elements is based on the blocking of carbon diffusion in the material. One of the most common techniques to suppress the carbon ingress, and through this, the metal dusting attack requires elements which can continuously form a dense, adherent, defect-free, and stable oxide scale on the surface of the component with the remaining oxygen in the atmosphere [2,27,56]. Such an oxide scale will be formed if the oxygen partial pressure is higher than its dissociation pressure [57].
In order to evaluate the metal oxidation and the stability of the formed oxides under a given temperature, one should take into account the theoretical basics of the Ellingham-Richardson-diagram (see Fig. 2.7).

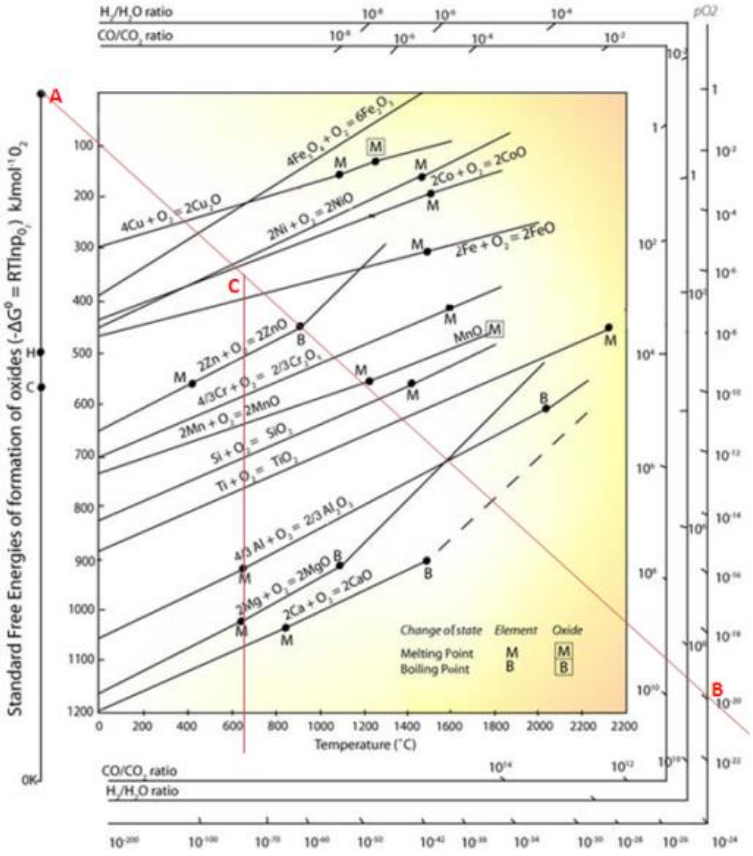

Figure 2.7: Ellingham-Richardson diagram for some oxidation reactions [48]

BUPT

The scale on the right side of the diagram labelled "pO_2" is used to determine which value for the partial pressure of oxygen is needed for equilibrium with the metal and metal oxide at a given temperature. For the determination of the stable oxides at a given temperature and known pO_2, it is necessary to connect a straight line from point A (standard free energies of formation of oxides) to point B of the known pO_2 (here $pO_2=10^{-20}$; standard value in syngas industries). Subsequently, a new vertical line will be drawn from the given temperature on the x-axis (here 650°C) to point C. Generally speaking, all oxides on this line are stable under these conditions, but not all of them are suitable for the protection of materials against metal dusting. This requires a short description of the kinetics for the growth of an oxide scale.

Growth Kinetic Mechanism of Oxide Scales

Along with the linear growth of oxide scales with a proportional change in mass over time, there is a parabolic growth time law of oxide scales at temperatures above 500°C. A linear mass gain during oxidation suggests that the formed oxide scale is not dense, because of its disintegration after a short time. For metals, which follow the parabolic oxidation law, the rate of the oxidation process can slow down and can almost gradually come to a stop after forming an oxide layer on the surface. The theory for the formation of a parabolic oxide scale was developed in 1933 by Wagner. With regards to Wagner´s model, Bürgel [40] states that it is assumed that a thin, crack-free, and perfect oxide scale is already available at the beginning of the oxidation process. There are two fundamental processes of the parabolic oxide scale growth for metal oxides (see Fig. 2.8).

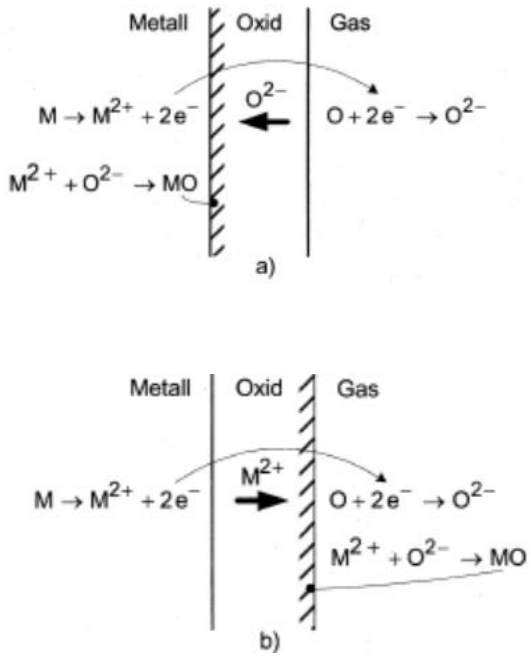

Figure 2.8: Wagner´s model of the parabolic oxide scale growth for metal oxides

BUPT

If the diffusion rate of the oxygen ions is faster than that of the metal ions through the existing oxide scale, the growth of the oxide scale takes place at the interface metal/oxide (see Fig. 2.9 a). Otherwise, the metal atoms move first in the direction of the surface through the defects of this oxide scale [58]. This occurs because of their attempt to achieve the noble gas configuration (see Fig. 2.9 b). That means, the metal loses its electrons:

$$Me \rightarrow Me^{2+} + 2^{e-} \qquad (Eq.\ 2.3)$$

The remaining molecular oxygen, which surrounds the metal atoms, dissociates into two oxygen atoms. The oxygen atoms will take up the electrons, previously delivered by the metal:

$$O_2 \rightarrow 2O \qquad (Eq.\ 2.4)$$

$$O + 2^{e-} \rightarrow O^{2-} \qquad (Eq.\ 2.5)$$

Then, a metal cation and an oxygen anion react to an oxide molecule:

$$Me^{2+} + O^{2-} \rightarrow MeO \qquad (Eq.\ 2.6)$$

The parabolic law describes the mass gain (Δm) in dependence of the time:

$$\Delta m = A * \sqrt{k_p * t} \quad [g] \qquad (Eq.\ 2.7)$$

A	sample surface [m²]
k_p	parabolic oxidation constant [$kg^2m^{-4}s^{-1}$]
t	time [s]

The parabolic oxidation constant (k_p) results from the Arrhenius-function:

$$k_p = k_{po} * e^{-\frac{Q}{R*T}} \quad [m^2/s] \qquad (Eq.\ 2.8)$$

k_{po}	prefactor
Q	activation energy [$kJ \cdot mol^{-1}$]
R	gas constant
T	temperature [K]

With consideration of the formula for the parabolic law, it is quite clear that oxides for long-term applications should have a low oxidation constant, since the mass increases quadratically to the time.

BUPT

As shown in the following Fig. 2.9, Al_2O_3 has the lowest oxidation constant. The oxides SiO_2 and Cr_2O_3 follow closely.

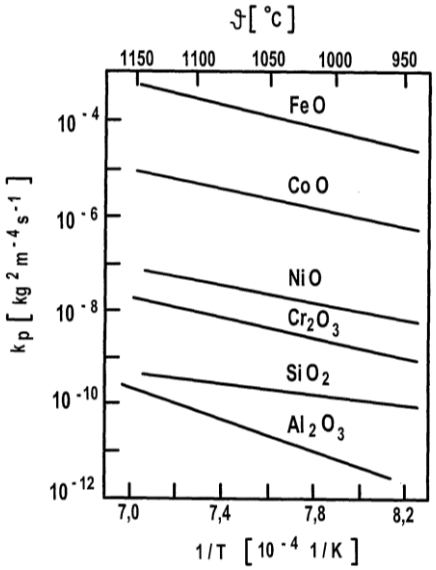

Figure 2.9: Some parabolic oxidation constants k_p in dependence of the temperature [29]

In the year 1923, Pilling and Bedworth formulated a rule in order to recognize the protective effect of oxide scales. The criterion is named the Pilling-Bedworth-Value (PBV). The PBV gives the ratio between the unit cell-volume of the oxide and the metal [40] (see Eq. 2.9). The variable "M" [g/mol] stands for the molar mass, "V" [m³/mol] is the molar volume, "ρ" [kg/m³] is the density, and "n" represents the number of metal atoms.

$$\frac{V_{oxide}}{n*V_{metal}} = \frac{M_{oxide}*\rho_{metal}}{M_{metal}*n*\rho_{oxide}} \qquad \text{(Eq. 2.9)}$$

The development of growth stresses may lead to damage to the oxide layer if the PBV value is smaller than 1. If the PBV is much higher than 1 (e.g. 8), compressive and growth stresses can occur parallel to the surface [58]. These stresses lead to the spalling of the oxide layer. If the PBV is higher than 1, the grown oxide scale is roughly stable and performs a protective function [40].
The PBW values for some oxides are listed in the following table:

Table 2.2: Oxide-metal volume ratios of some common metals [40,59]

Oxide	CaO	MgO	Al_2O_3	FeO	Cr_2O3	SiO_2
PBW	0,64	0,81	1,28	1,7	2,05	2,15

The positive effect of stable oxide scales, which fulfill both criteria (k_p and PBV), has been studied by many scientists including Grabke [26,35,36,45], Ramanarayanan

BUPT

[23,60,61], and Nishiyama [25,55,56], to name a few. These oxide scales, with reasonable stability under low oxygen partial pressure, have been proven to be an effective method to prevent metal dusting. Alkaline earth metals like CaO and MgO do not provide a sufficient protection under these conditions [62]. Oxides formed with elements from the first and second main group in the periodic system, form cracks. Therefore, they are not dense [40]. The same observation is applicable to FeO [14].

Although oxides may be stable, the oxide scales may still be susceptible to disruption, due to the carbon capture (coking) on their surface. As long as an ideal Cr rich protective oxide scale can no longer be formed on the material surface, its microstructure becomes carburized. This phenomenon leads to a steady state corrosion rate, as described by Walmsley et al. [50] and observed for Alloy 600 and 601 after long exposure time under laboratory metal dusting conditions. For this reason, a high amount of the oxide scale forming element served as a reservoir able to ensure the scale healing process. It made it more rapid and complete [34,41] over a long period of time.

Even the Cr_2O_3 forming process can be supported through the addition of carbide forming elements. Strauß and Grabke [63] predicated that the addition of carbide forming elements, like Mo, W, or Nb, with a higher affinity to C than Cr, prolongs the incubation time for metal dusting. In consequence, more Cr for the formation of a protective Cr_2O_3 scale is available.

This mechanism could be further improved. Nishiyama et al. [56] confirmed that the newly developed Sumitomo® 696 alloy with Ni-30%Cr-2%Si-2%Cu specified above shows an excellent metal dusting resistance up to 22,000 h in a CO-H_2-reducing atmosphere at 650°C. He described that Cr and Si are able to form a protective oxide scale on the surface of the material. Moreover, a solid solution of Cu suppresses the reaction of the CO molecules with the metal at the positions where the oxide scale was destroyed. In this case, the healing of the oxide scale could take place, because Cu does not act catalytically. The principle of this mechanism is shown schematically in Fig. 2.10.

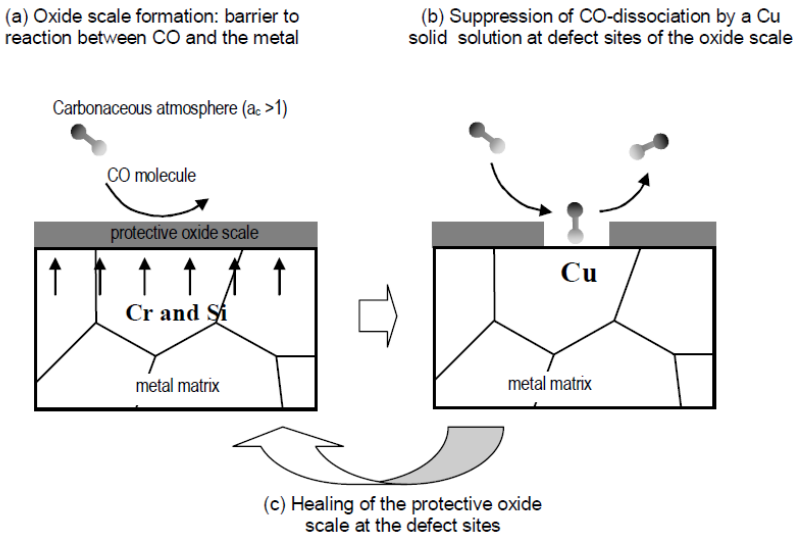

Figure 2.10: Schematic representation of the metal dusting prevention technique [55]

BUPT

As mentioned before, the adverse effect of alloying must also be taken into account. For example, the presence of high amounts of W and Si in an alloy may degrade desirable properties such as ductility and strength. The addition of elements like Al or Ti, outlined above, can lead to the formation of internal oxides and to an increased brittleness which weaken the alloy. Therefore, such alloys can be used only as coating which are applied by different technologies on ductile substrates. Coatings provide more significant advantages. In many cases, they can be repaired [27] and are a cheaper alternative to changing the overall alloy composition [48].

2.6. Coatings for the Improvement of the Metal Dusting Resistance

The task of a coating is to prevent the contact between the metallic material and the environment. Coatings are intermetallics or alloys, and can be deposited by a number of techniques including physical vapor deposition (PVD), chemical vapor deposition (CVD), electro-deposition, or thermal spraying [27]. As mentioned above, the protection of components under metal dusting conditions is based on the ability of elements to form a dense, adherent, defect-free, and stable oxide scale with the remaining oxygen in the atmosphere. Due to the outlined characteristics, only Cr_2O_3, Al_2O_3 and SiO_2 are potential oxides for such applications.
Melo-Máximo et al. [64] investigated Cr/Cr_2O_3 thin films deposited on 304L stainless steel substrates by reactive magnetron sputtering (RMS) under metal dusting conditions. The samples were exposed to an atmosphere consisting of $CH_4 + H_2$ and residual oxygen at 800°C for up to 20 hours via thermogravimetric analysis (TGA). The results showed that the Cr/Cr_2O_3 thin film clearly improved the resistance of the 304L steel. Melo-Máximo et al. confirmed the well-known theory that the catalytic deposition of carbon on the Cr_2O_3 surface was less present. Moreover, the Cr_2O_3 thin film hindered the carbon diffusion into steel due to the low diffusion coefficient of carbon in oxides.
Brandl et al. [32] reported that flame tubes, coated with a NiCrAlY alloy, which belongs to the group of MCrAlY alloys (M= Ni, Co or Fe), exhibit a good stability under metal dusting conditions. In this work, uncoated and MCrAlY-coated samples made of alloy 601 and alloy 602 were tested at 700°C by the use of computer controlled special equipment. After 300 hours, the uncoated samples revealed specific characteristics of metal dusting degradation, whereas, the MCrAlY-coated samples formed an even Al_2O_3-scale as a protection against carbon ingress. Based on this result, the samples were not attacked even after 850 hours. They demonstrated that the β-phase (NiAl) in the MCrAlY-coating with 8 mass% Al delivers sufficient Al for the forming of a stable Al_2O_3 scale.
In addition, Voisey et al. [48] confirmed the positive effect of a 150 µm thick plasma sprayed Ni31Cr11Al0.6Y coating on the metal dusting resistance of Alloy 800H. It takes 30 times longer to initiate metal dusting of the MCrAlY-coated sample, compared to the uncoated Alloy 800H in 80 vol% CO, 20 vol% H_2 at 650°C.
Chun et al. [61] investigated the metal dusting corrosion resistance of powder plasma welded (PPW) NiCrAl base alumina forming coatings with 25 mass% Cr and 6 mass% Al on alloy 601, which were exposed in carbon supersaturated environments in $CO–H_2$ for 1000 hours at 650 °C. The continuous Al_2O_3 film provided protection against metal dusting.

BUPT

Alvarez et al. [65] deposited Al/Al_2O_3 layers by reactive magnetron sputtering on HK40 substrates under various conditions in order to develop the most adequate structure for protection against metal dusting. The samples were exposed to a gas mixture of CH_4–Ar at 600 °C for 50 hours. Alvarez et al. confirmed the well-known theory that the density and adherence of the oxide coating to the substrate, is needed to protect the substrate. The deposition method was less advantageous, because of the resulting tensions during the reactive magnetron sputtering. These tensions (internal stress) led to the formation of cracks during the exposure in the carburizing atmosphere.
As mentioned before, besides aluminum and chromium, silicon is one of the most favorable protective scale forming elements. The positive effect of silicon for the oxidation resistance of heat resistant steels and Ni-Cr heater alloys were already well established by 1930. Silicides formed by diffusion in nickel base superalloys have been in use since the 1960s, especially for gas turbine applications. Recently, silicon is gaining interest as an alloying element and as a coating element for the purpose of improving carburization resistance in coal conversion plants, and high temperature gas cooled reactor (HTGR) helium environments [66].
Lang et al. [67] investigated the carburizing resistance of SiO_2- plasma-assisted vapor deposited (PVD) coatings with a thickness of 4 to 9 µm on Incoloy 800H. The specimens were exposed at 825°C and 1000°C for up to 1000 hours in H_2-CH_4 gas mixtures at a pressure of 1.6 bar, with an oxygen partial pressure of 10^{-28} bar, and a carbon activity of about 9.8. The $Si0_2$ coating completely prevented the carburization of Incoloy 800H at 825 °C. During the exposure of the samples at 1000°C a reduction of the SiO_2 occurred and the formation of SiC took place. In this work, it was asserted, that the role of SiO_2 in the metal dusting phenomenon has not been fully understood.
While some scientists claimed that SiO_2 provides a good protection under metal dusting conditions, others assumed that SiO_2 might act as a nucleation site for the metal dusting phenomenon [27,66]. For example Rahmel and his co-workers [27,68] pointed out that the principal mechanism of degradation by carburization is based on the conversion from oxides into carbides. They argued that silica is stable under metal dusting conditions and its conversion to the corresponding carbides occurs at significantly higher temperatures than that of chromium. Nonetheless, a better understanding of the Si effect is needed [27]. Therefore, the role of silicon containing self-fluxing alloys, which have proven to be very successful for other applications, will be focused on in this work. This group of coatings will be described in particular in the following chapter.

2.7. Thermal Sprayed Self-Fluxing Coatings

Flame spraying and fusing of self-fluxing alloys is standardized in EN ISO 14920:1999-03 "Spraying and fusing of self-fluxing alloys" and is known in Germany as DIN EN ISO 14920 "Thermisches Spritzen –Spritzen und Einschmelzen von selbstfließenden Legierungen" [69].
Generally speaking, thermal sprayed and remelted Ni based self-fluxing coatings are used for components in applications requiring wear resistance combined with corrosion resistance [4,5,70].
Considering all the most common Ni based self-fluxing alloys, namely NiCrBSi, which are focused on in this work, Ni is the most corrosion resistant component at higher temperatures and provides high mechanical strength and stability [4]. The

BUPT

addition of Si and B gives them the "self-fluxing" characteristic, and together they reduce the melting interval [4,5]. In the same way, boron effectively increases the hardness. The melting interval of commercial NiCrBSi alloys ranges between 960°C and 1220°C (pure nickel = 1455 °C) [71].

The effect of B and Si on the melting temperature of NiCrBSi alloys are shown in the binary phase diagrams (see Fig. 2.11 and Fig. 2.12). The Si and B contents are mostly in the region between 2 and 4.5 wt.

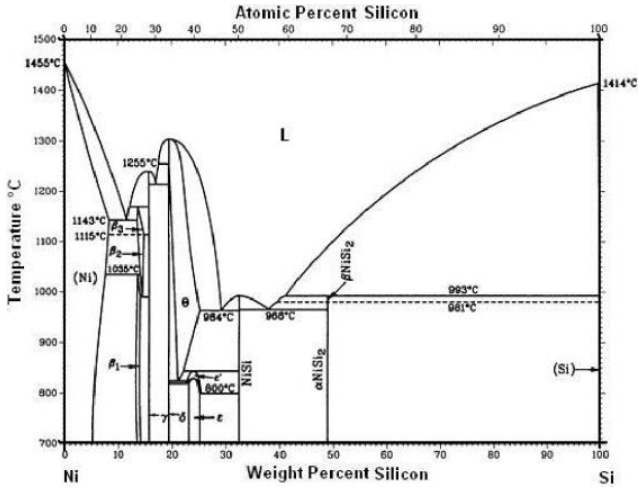

Figure 2.11: Binary phase diagram of Ni-Si [72]

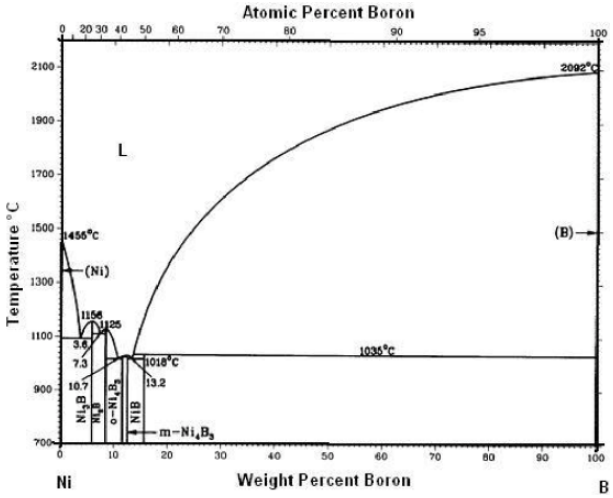

Figure 2.12: Binary phase diagram of Ni-B [72]

Normally 5 mass% up to 18 mass% Cr enables the resistance against oxidation at high temperatures. Cr also increases the hardness of the coating, because of its tendency to form very hard precipitates [8]. Carbon, usually up to 1 mass% in standard self-fluxing alloys, produces carbides with high hardness levels that

BUPT

improve the wear resistance of coatings [72,73]. If the hardness is not sufficient, the addition of W- and Cr-Carbides takes place.

It has been proven that the phenomenon of a pitting attack occurs mainly at the edges and corners. The damaging of the protective oxide film tends to be higher at these regions [20]. Therefore, Cu and Mo are added in order to improve the edge stability [74]. Moreover, it is common knowledge that Mo (min. 2 mass%) increases the corrosion resistance in aqueous media. The addition of Fe is mostly due to reasons of cost, because Cr, B, and Si are generally added in the form of ferro-compounds during the fusion-metallurgical production of the alloys [71].

Self-fluxing alloys are typically deposited on the substrate with different kinds of thermal spray methods. These include the oxygen-fuel-flame spraying, high-velocity-oxygen-fuel spraying (HVOF) [4,5,72,75], and also laser cladding [76]. The sprayed Ni based self-fluxing alloys have a typical microstructure as a result of the spraying technology [77]. A schematic representation of thermally sprayed coatings is shown in Fig. 2.13.

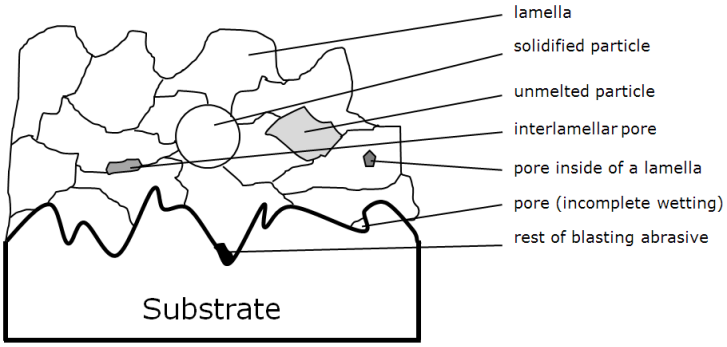

Figure 2.13: Schematic representation of thermal sprayed coatings

Over all, the layer structure of the sprayed coatings depends on the technology used. The HVOF process enables coatings with low porosity and minor unmelted particles, whereas the classical flame spraying results in poor coating quality [77]. Polema [78] stated that the porosity of non-sintered plasma sprayed self-fluxing coatings can reach 10-12% and that of gas-sprayed coatings can even reach 20%. Researchers like Buytoz [72] also confirmed that the HVOF thermal spraying process is one of the best methods for the deposition of conventional Ni based and NiCr feedstock powders. This is due to the hypersonic velocity of the flame, which shortens the time of interaction between the powder and the atmosphere and reduces the oxidation of the molten metallic particles. However, it should be noted, that the HVOF-coating technique is more expensive in comparison to conventional flame spraying [5].

It is well known that an improved quality of self-fluxing alloys is reached through a subsequent remelting process. This process step consists in fusing. In order to remelt the sprayed coatings, post treatments are carried out in a flame, with a laser, in a vacuum furnace [4] or inductively [79]. According to González et al. [80] the flame remelting technology is the most commonly used method, because of its

BUPT

versatility and economical aspects [80]. It can be applied to achieve a higher density [4,81], thereby less pores, homogenization of the microstructure and higher cohesion and adhesion [4]. The adhesion on the substrate can be considerably increased from 15-25 MPa (adhesion force after flame spraying process) to 110-450 MPa [81]. Overall, an improvement of the performance with respect to the properties described above can be reached through the use of the post treatment [4].

2.7.1. The Complex Phase Structure of Self-Fluxing Materials

The ternary Ni-Cr-B alloy system has a multiphase structure (see the liquidus projection of the Ni-Cr-B ternary phase diagram in Fig. 2.14).

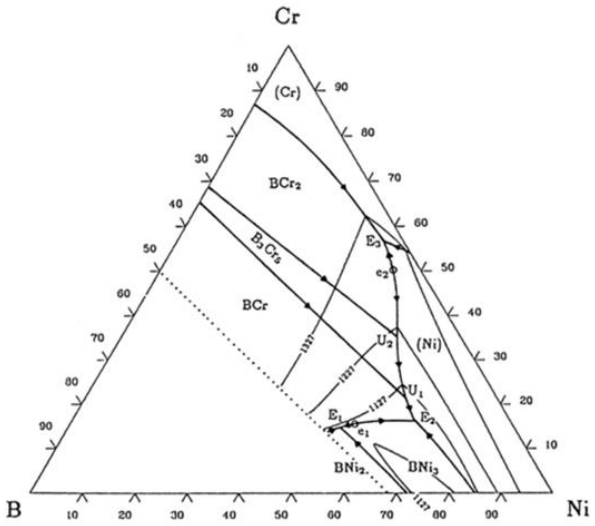

Figure 2.14: Ni-Cr-B liquidus projection [82]

The structure consists of a solid solution of chromium in nickel γ – Ni(Cr), nickel borides Ni_3B and borides of chromium (CrB, Cr_2B, Cr_5B_3) [83]. Nickel can dissolve small amounts of boron (0.1 mass%). This solubility is unfortunately not increased by the addition of chromium, as might be expected.
It is a commonplace that up to 5 mass% Si and up to 1 mass% C in standard NiCrBSi alloys makes the phase constitution more complex. These NiCrBSi alloys are able to form various types of carbides, borides, and silicides [83–86]. Nickel, for example, can dissolve a relatively large quantity of silicon into a substitution mixed crystal. The limit of solubility for Si in Ni is situated at approximately 8.5 mass% at 1143°C.
The microstructure of NiCrBSi powder for the thermal spray process was investigated with X-ray diffraction by Dudek [87] and also by Buytoz et al. [72]. Dudek analyzed a powder with 14 mass% Cr, 4 mass% Si, 3,5 mass% Fe, 3 mass% B and more than 70 mass% Ni. Beside the main signals of Ni and Cr, he detected CrB, Ni_3B, Cr_3Si and NiSi. Buytoz [72] examined the phase composition of

BUPT

a NiCrBSi feedstock powder with only 1 mass% more Si and 0,5 mass% less Fe. His evaluation differs only slightly from the results of Dudek (see Fig. 2.15).

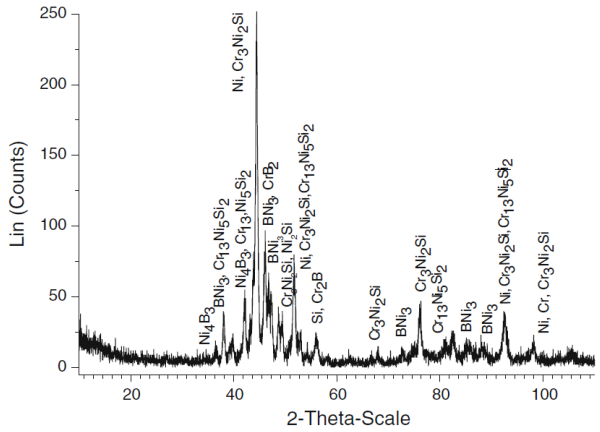

Figure 2.15: XRD analysis of the powder NiCrBSi [72]

It is often claimed that the modification of small amounts of the elements can influence the phase constitution of self-fluxing alloys. That was demonstrated by Hemmati et al. [84]. This work proved that the Cr content and the Si/B ratio affect the microstructure of NiCrBSi alloys. Depending on the alloy compositions, some phases like chromium boride and carbide precipitates (different types and amounts), Ni solid solution, and Ni-B-Si binary and ternary eutectics can be formed [84]. Moreover, he reported that the alloys with a higher Cr and B content with a lower level of Si/B, display a more complex microstructure, whereas, the low alloyed NiCrBSi exhibit a rather simple dendrite-structure (Ni solid solution with limited amounts of interdendritic eutectic phases) [84]. Otsubo et al. [70] confirmed this theory. Mrdak et al. [83] described the influence of the phase formation according to the amounts of the elements. He wrote about an increasing content of chromium carbide precipitates (Cr_7C_3) in remelted coatings with a carbon content over 0.8 mass% C. Kima [88] reported about CrB in coatings, if the content of boron was higher than 2 mass%. Cr_5Si_3 were detected in coatings with more than 3.2% Si. These phase transformations occur apparently after the spraying or remelting process. This fact has been addressed by many other scientists, however, this theory is still very controversial. Borisov [81] described that conventional melted Ni based self-fluxing alloys consist mainly of a nickel base γ -solid solution, an eutectic of nickel borides (NiB and Ni_2B) and the γ -solid solution, borides of chromium (mainly CrB) and nickel (Ni_3B), respectively chromium and nickel carboborides, together with a nickel silicide (Ni_3Si) and slag inclusions (boron, silicon, and chromium oxides). Šárka Houdkovà et al. [77] e.g. showed that laser remelted NiCrBSi coatings consist of FeNi (γ-Ni), CrB, Ni_3B, Al_5FeSi, Ni_xSi_y and FeSi. Carbides were not observed.
González et al. [80] studied the influence of flame spraying combined with flame remelting, flame spraying combined with laser remelting, and laser cladding on the microstructure of a NiCrBSi alloy. During laser cladding, the powder of a desired composition and a thin surface layer of the substrate material are melted

BUPT

simultaneously under laser irradiation, and then rapidly solidified to form a dense coating. The main characteristic of such a coating is the good metallurgical bond to the base material with a minimum dilution of the clad layer [80]. González asserted that the microstructure of a NiCrBSi alloy with 15 mass% Cr, 4 mass% Si, 4 mass% Fe, 3 mass% B, and more than 70 mass% Ni showed a similar phase structure, but differed in morphology, size, percentage, and distribution of the different constituents as a function of the coating technique. Through the SEM analysis, Cr precipitates were detected, which revealed a high concentration of Cr carbides and Cr borides after the flame spray process. The Ni matrix contains small amounts of Cr, a low percentage of Fe, and an average concentration of Si, with respect to the chemical composition of the original powders. Rodionov et al. [86] reported similar phase composition of atmospheric plasma sprayed coatings compared to that of the powders. On the contrary Mrdak et al. [83] described in their paper that the atmospheric plasma spraying (APS) of a NiCrBSi alloy with 14 mass% Cr, 4,5 mass% Si, 4,5 mass% Fe, 3,3 mass% B, 0,75 mass% C and 72,95 mass% Ni resulted in a change of the phase structure. Before the APS-process, the powder consisted of the γ-Ni(Cr) and the solid phases Ni_3B, NiSi, CrB and Cr_3Si. After the APS-process, the structure was mainly composed of γ-Ni(Cr), CrB, Ni_3B, Cr_7C_3 and Ni_5Si_2.

2.7.2. Critical Consideration

Some statements regarding the phases detected in self-fluxing materials have to be critically reviewed. Very often conventional X-ray diffraction (XRD) was used in order to identify the phases. The evaluation of the XRD-patterns for complex microstructures of NiCrBSi coatings is very difficult, because the peaks of different phases can overlap. In this case, it is a challenge to determine which peak belongs to which phase. This can lead to false quantitative and qualitative evaluations. On this account, the evaluation of XRD-patterns requires years of experience and the ability, often based on intuition, to make a correct evaluation. For example, Houdkovà´s statement has to be critically questioned, because he did not observe carbides in laser remelted NiCrBSi coatings, although other scientists found carbides after laser remelting [85,89,89]. It is possible that mistakes have been made within the evaluation of the XRD-patterns, based on the position of the elements in the periodic table. The signals for C and Si are superposed directly above one another.

A further possible reason for the recognizable deviations in the scientist´s results, with reference to the detected phases, is the location of microstructural characterization. It was confirmed by Hemmati et al. [84] that laser remelted NiCrBSi alloys are able to form multiple microstructures from the same chemical composition. Previous works of the authors [84] showed that different microstructures and phases may form one NiCrBSi clad layer with gradual or abrupt changes across the clad length or depth. Therefore, depending on the location of microstructural characterization of the coating, different types of phases are possible to be reported for similar compositions.

BUPT

2.8. Motivation

Based on the development of innovative catalysts and constant efforts to improve the efficiency of processes involving the production of syngas, the metal dusting corrosion phenomenon is focused on by many scientists. Due to the premature failure of Fe-, Co-, and Ni based alloys, scientists from all over the world are searching for new materials or coatings with an improved resistance under metal dusting conditions.
Standard self-fluxing alloys have not been investigated up to now under metal dusting conditions due to their operating temperature limit of 540°C. The restriction is predetermined by well-known manufacturers like Oerlikon Metco and Castolin. A study of the source material concerning the reason for the limited operating temperature revealed that the thermal sprayed self-fluxing coatings showed no changes of the mechanical properties after long-time tests up to this temperature. At higher temperatures, over 700°C, an outward diffusion of chromium borides occurs. This leads to a reduction of the hardness which is a very important property of self-fluxing protective layers in wear applications. However, in this work a high hardness, usually up to 800 HV (Vickers hardness), is not relevant for the protection of materials against metal dusting conditions.
One of the most common techniques to prevent metal dusting is the formation of an oxide scale on the surface, which may improve the steady state time [55]. Chromium oxides have been proven to provide very good protection against metal dusting, and even exceed optimistic expectations. However, it is known that a stable Cr_2O_3 oxide layer can only be formed above an oxygen partial pressure of 10^{-20} atm (standard value in syngas industries) at 650°C (see Ellingham-Richardson diagram). Numerous laboratory and field tests have confirmed that a certain percentage of Al as an Al_2O_3 forming element in combination with a Ni based matrix is able to reduce the metal dusting corrosion mechanism substantially even at an oxygen partial pressure of 10^{-55} atm. Generally speaking, Cr_2O_3 and Al_2O_3 forming materials have been extensively investigated and are well understood. In contrast, the Si oxide forming Ni based alloys with higher Cr contents has not yet been sufficiently studied. Silicon oxides can already be formed at an oxygen partial pressure of only 10^{-42} atm. In the year 1972 Schueler [90] proposed that that the effectiveness of the metal dusting resistance can be calculated by the equivalent equation:

$$\mathrm{Cr}_{\mathrm{equivalent}} = \mathrm{Cr}\% + 2 * \mathrm{Si}\% \geq 22 \qquad (\mathrm{Eq.}\ 2.10)$$

However, this statement is an empirical one and has not yet been conclusively proved until up to now. Furthermore, the metal dusting resistance of alloys under consideration of the elements Si and Cr in relation to each other has not been investigated. Therefore, the effect of the Si- and Cr- containing phases on the metal dusting resistance of standard self-fluxing alloys with up to 18 mass% Cr and 4 mass% Si after different fusing processes will be focused on.

BUPT

3. METHODOLOGY

The morphology, structure, and chemical composition of the thermal sprayed coatings, and of the nuggets obtained from the feedstock powders, were observed by means of light microscopy (LM), scanning electron microscopy (SEM) combined with energy dispersive spectrometry (EDS or EDX), X-ray diffraction (XRD), UV-emission spectroscopy (UV), or X-ray fluorescence spectrometry (XRF). For the visualization of the Si containing phases, a special colour etching process was used. The differential thermal analysis (DTA) enabled the determination of the melting interval of the self-fluxing feedstock powders. For the determination of the temperature during the melting process with the inductor, a voltmeter with thermocouples was used. The hardness measurements of the melted samples were done by means of a microhardness tester. The samples were tested under metal dusting conditions inside of a custom made high temperature corrosion test rig.

3.1. Light Microscopy (LM)

Within the scope of this work the light microscope Leica DM-RME was used. With the aid of two lenses (objective and ocular), incoming light beams were refracted through the objective lens, creating an intermediate image, which was enlarged with the aid of an ocular. A schematic presentation for the function mode of a light-microscope is shown in Fig. 3.1.
In addition, a Keyence VHX-600 digital light microscope was also used. With this type of digital microscope, the ocular is replaced by an electronic display, in contrast to the above described light microscope. The main advantages of the digital light microscope are the higher depth of focus, and the possibility to generate 3D-images (made from up to 9 single images) for the representation of the topography. This is achieved through a digital processor in combination with high performance software.

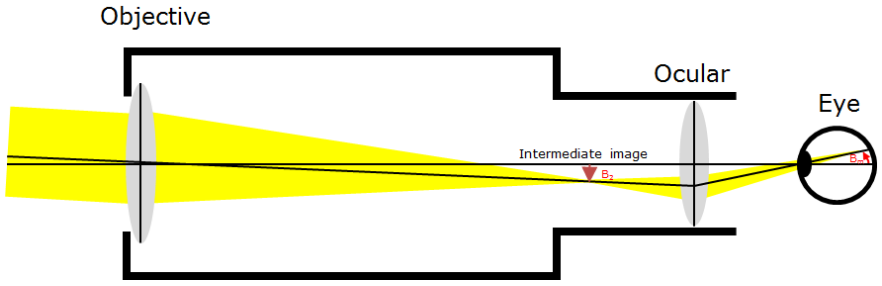

Figure 3.1 Schematic presentation of the function mode of a light microscope

3.2. Scanning Electron Microscopy (SEM)

The SEM studies were performed with Philips XL 30 ESEM microscope (Environmental Scanning Electron Microscope). Fig. 3.2 [91] represents the schematic overview of such an SEM. This microscope has a tungsten cathode, which generates a very thin (0.01 µm) electron beam by applying an electric current. With the aid of a deflecting coil, the electron beam is scattered over the surface of the samples. Through the impact of the primary electrons of the electron beam, secondary electrons (SE) are generated from a microvolume at the sample surface. These electrons are then captured by an SE-detector. The local distribution of the secondary electrons can be shown in three dimensions on a monitor.
For the generation of a material contrast image, an additional detector picks up the primary electrons, backscattered from the screened object. Due to that reason, the detector is called a BSE-detector (backscattered electrons). On the monitor, lighter elements (e.g. Si) appear dark, and heavier elements (e.g. W) are depicted in light grey, because of their higher backscattering intensity [92].
For the EDX-analysis, a method for the quantitative determination of elements (the minimum detection limit is 1wt-%), an additional detector was used. Such a solid-state X-ray-detector is able to collect the specific energy (X-ray quantum) that is produced when a shell electron is located from the primary electrons of the electronic beam and is replaced with an electron from an outer shell, in order to reach a lower state of excitement. With the measured energy, the EDX-detector can classify elements with an atomic number >10 [91]. For elements with a low atomic number (e.g. boron, carbon and nitrogen), the detection limit is considerably poor and more inexact.

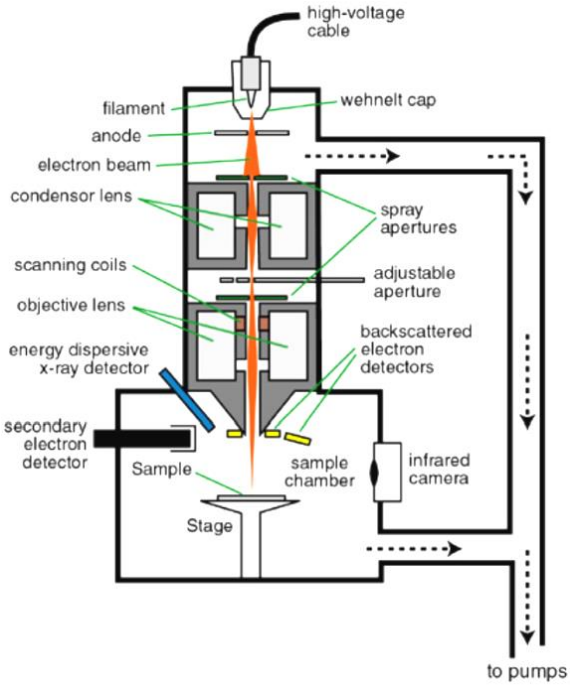

Figure 3.2: Scheme of a Scanning Electron Microscope

BUPT

For the graphical representation of the distribution of elements in the sample, an EDX mapping can also be generated with the SEM. In addition to conventional energy dispersive spectrometry, EDX (Energy-dispersive X-ray) mapping provides a meaningful method for observing the element distribution in a sample. In contrast to the aforementioned method for determination of the chemical composition with the aid of the quantitative energy dispersive spectrometry, the EDX-mapping is a qualitative method.

3.3. X-ray Diffraction (XRD)

For the examination concerning the phase composition of the investigated samples, X-ray diffraction (XRD) technique was used. This method is a rapid analytical non-destructive technique, primarily used for phase identification of a crystalline material. In this process, a characteristic roentgen radiation (X-ray) will be generated and directed onto the surface of the sample. The electrons in the sample are responsible for scattering these X-rays. In crystalline materials, the atoms are arranged in a regular structure. Due to this reason, the scattering results in a minima and maxima in the diffracted intensity, whereby the weakest signal follows the Bragg´s law $n*\lambda = 2d\sin\theta$, with n as an integer, λ as the X-ray wavelength, d as the distance between the crystal lattice planes (interlayer spacing), and θ as the diffraction angle, shown in Fig. 3.3 [93].

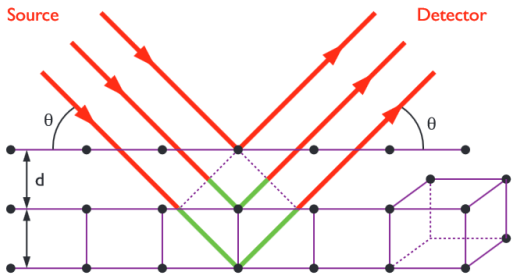

Figure 3.3: Schematic representation of diffraction of X-rays in a crystalline material

The intensity and spacing of these diffracted beams are unique for each type of crystalline material, and can be identified through reference to a published atlas. The X-ray diffraction examinations were performed using an X`Pert MPD apparatus from Phillips. This diffractometer is equipped with a high-resolution vertical goniometer with a long fine focus ceramic tube PW3373/00, Cu anode, wavelength 0.154 nm, max. 2.2 kW, 60 kV.

3.4. Colour Etching

For the visualization of the Si containing phases, which have the same contrast as the matrix, a special colour etching process was used. As noted by F. Richter [94], the use of a sodium-picrate solution as an etching agent for Fe-Si alloys leads to the formation of a thin oxide scale on the surface of the metal-silicon-mixed crystals, whose strength depends on the Si amount and etch time. After 30 seconds at 95°C in a sodium-picrate solution, phases in Fe-Si alloys with 5 mass% Si appear blue or blue-green, those with 9 mass% Si appear red or orange, and those with more than 14 mass% Si appear violet or brown. This solution with the chemical formula $C_6H_2N_3NaO_7$ consisted of 75 cm³ distilled water, 25 g sodium hydroxide (NaOH) and 2 g picric acid ($C_6H_3N_3O_7$).

In order to observe the Cr- and Ni-silicides in the Ni based self-fluxing alloys under the light microscope, it was necessary to modify this colour etching process. For that reason, a high number of tests with different parameters for the Ni based self-fluxing alloys were performed within the scope of a bachelor thesis "Detection of Silicon Rich Phases in NiCrBSi coatings by Metallographic Investigation" by the student Christian Schwabe at the Department of Materials Science of the Westphalian University in Gelsenkirchen, Germany. A solution with the same concentration, as indicated above, was produced under observation of the safety regulations, and heated up to 95°C.

First, all samples were ground with 500, 800, and 1200 grit paper with a grinding pressure of 20 N for 60 seconds. They were then polished with a 3 µm diamond suspension using a contact pressure of 25 N for 5 minutes on a polishing disc (MD Plus), cleaned with ethanol, and then dried with hot air. After that, the samples were immersed in the hot solution for 90 seconds. That was the ideal time for a clear colour change. Finally, the samples were dipped in distilled water and immediately cleaned with ethanol. For the chemical analysis of the colored phases by EDX, they were marked with microhardness indentations. The marked phases were then analyzed with the help of the SEM combined with EDX-analysis.

BUPT

3.5. UV Emission Spectroscopy (UVS)

Another method that was applied in order to determine the exact chemical composition, especially of the base alloy, was the UV-emission spectrometry, using a SPECTROMAXx from the company Spectro Ametek. The schematic structure of the UV-spectrometer from the company Spectro Ametek is shown in Fig. 3.4 [95].

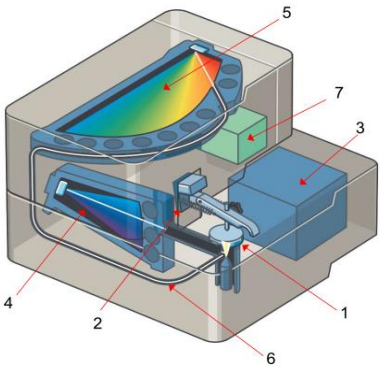

1. Spark Stand
2. Sample Holder
3. Stimulator
4. UV-Optic
5. Air-Optic

Figure 3.4: Schematic structure of the UV spectrometer from the company Spectro Ametek

Reference values for the elements, applied as verification for the measured values, were taken from the "Key to Steel" software, a German version from 2007. With the application of the UV emission spectroscopy, it is possible to get the value of the elements in the thousandth-of-a-percentage range. The samples are irradiated with electromagnetic waves of ultraviolet (UV) and visible light. The resulting reflections deliver the information about the elemental contents of the sample.

3.6. X-ray Fluorescence Spectrometry (XRF)

Due to the limitation that the UV emission spectrometer can be only used for metallic components with a minimum size of 0.25 cm² or a diameter of 0.5 cm (contact surface), the chemical composition of the self-fluxing powders was controlled with the X-ray fluorescence spectrometer SPECTRO MIDEX. Applying this method, atoms are excited and subsequently transmit the obtained energy via fluorescence (spontaneous emission of light) to a semiconductor detector. Through different radiation intensities, each element with an atomic number >11 (from Mg) can be detected.

3.7. Differential Thermal Analysis (DTA)

For determining the melting interval of the three powders, DTA was performed by using the thermogravimetric analyzer (TGA) Netzsch STA 449 F1 Jupiter. This method of measurement enables the determination of endothermic and exothermic reactions of the samples [96]. With reference to the statement of Mr. Strunk from the company Netzsch, during the measurements, the spontaneous temperature

BUPT

change (1/K) was being recorded with a thermocouple, located directly under the sample holder (ceramic crucible). The temperature change was then presented as a peak in a DTA-diagram. A peak went upward if a melting process was initiated, downward meant that crystallization was taking place, illustrated in chapter 4.

3.8. Thermocouple Measurement

The temperature during the melting process of the powders with the inductor was measured by using the data logger Almeno 2290-8, from the company Ahlborn, in combination with a Ni-Cr/Ni thermocouple for a temperature range between -270 and 1372°C. A thermocouple consists of two dissimilar connected metals [97]. If two metals are coupled at both ends, and one end is heated up, a continuous current flows in the thermoelectric circuit. Thomas Seebeck discovered this effect in 1821. An interruption of the circuit (Seebeck voltage), illustrated in Fig. 3.5 [98], leads to a voltage difference between the open ends and delivers the information about the temperature gradient. The Seebeck voltage is linearly proportional to the temperature: $\Delta e_{AB} = \alpha \Delta T$ [98].

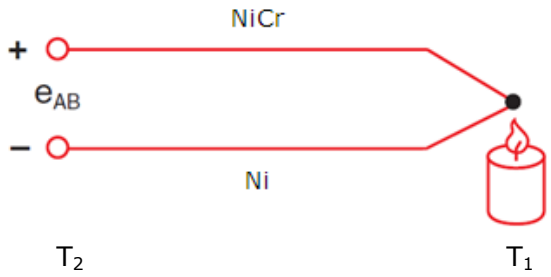

Figure 3.5: Open voltage circuit; e_{AB}= Seebeck voltage

3.9. Microindentation

The microhardness tester Zwick/Roell ZHVμ-S, with a test load range between HV0.01 and HV2, was used in order to mark micro areas with a diamond pyramid for further investigations. The Vickers indenter makes a pyramid-shaped impact with a depth of one-seventh of the length of the mean diagonals.

3.10. Exposure to Metal Dusting in the Corrosion Test Rig

The samples were tested under metal dusting conditions inside of a custom-made high temperature corrosion test rig. The high temperature test rig was developed during a previous research project, performed in 2002/2003, which dealt with the development of corrosion protective solutions for metallic materials in practical applications. For that purpose, it was necessary to develop up an appropriate test rig that was able to reproduce precise real world testing conditions, especially

BUPT

concerning the gas composition and the temperature, respectively. A schematic representation of the test rig is given in the following figure.

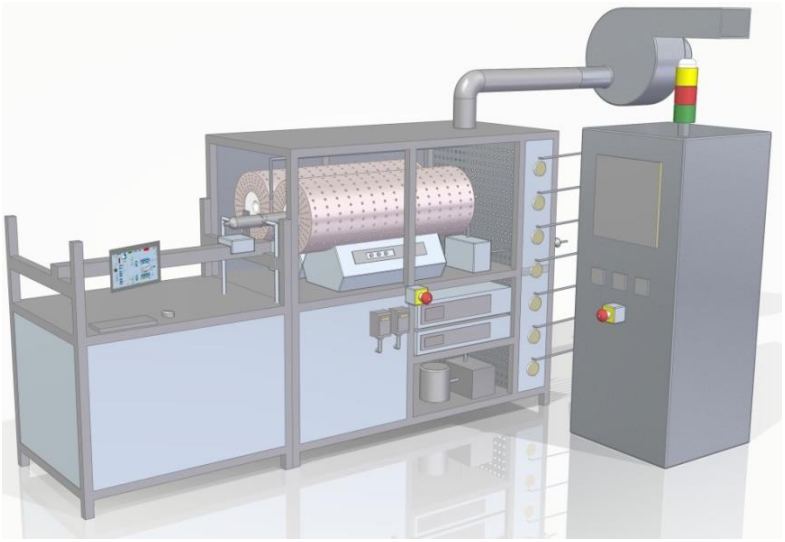

Figure 3.6: Schematic representation (CAD) of the high temperature test rig

In the schematic workflow (shown in Fig. 3.7) it can be observed that this test rig enables an exposure of samples in gases, such as air, nitrogen (N_2), carbon dioxide (CO_2), propane (C_3H_8), carbon monoxide (CO), nitric oxide (NO), sulfur dioxide (SO_2), hydrogen (H) or a mixture of them, up to 1000°C.

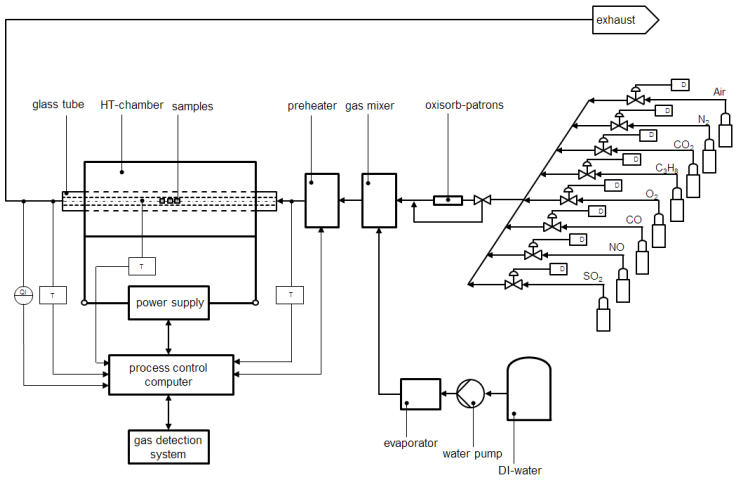

Figure 3.7: Function block diagram of the HT test rig

The supply and the dosage accuracy in ml/min. of the gases was assessed and adjusted with a mass flow controller (MFC) from the Company Bronkhorst Mättig, and was computer controlled and monitored via a graphical user interface,

developed with the Freelance ABB software from the Westphalian University Gelsenkirchen (see Fig. 3.8).

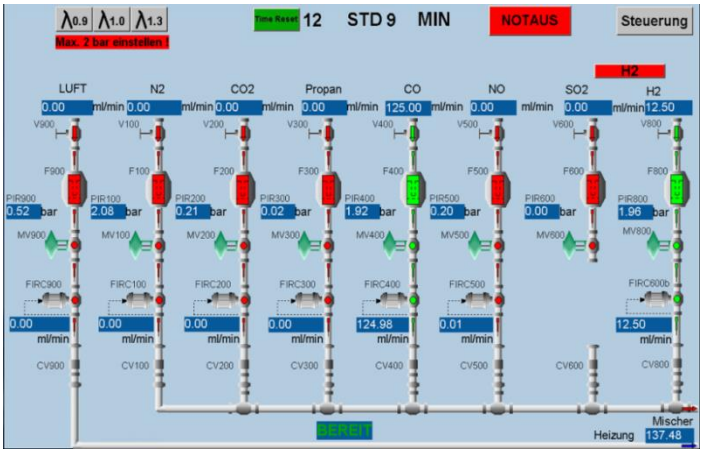

Figure 3.8: Graphical user interface 1 of the HT test rig

The downstream Oxisorb®-cartridge contains active elements able to remove the residual oxygen as a trace contaminant in pure gases down to 5 ppb (5.0×10^{-7} %). Its functional principle is based on the chemisorption of oxygen on a reactive chromium compound. When the active element is saturated with oxygen, the color changes from blue to brown, indicating that the cartridge needs to be replaced [99]. For the optional humidification of the gas stream with a newly installed high performance liquid chromatograph pump, a gas mixer was implemented. This hermetically sealed chamber was necessary because of the sensitivity of the Oxisorb-cartridge to moisture. The preheater mounted after the gas mixer is able to heat the gas mixture up to 500°C. This is especially necessary if the gas stream contains moisture. A preheating of the gas prevents the subsequent condensation of water. These functions are controlled and monitored with the aid of a second graphical user interface (see Fig. 3.9).

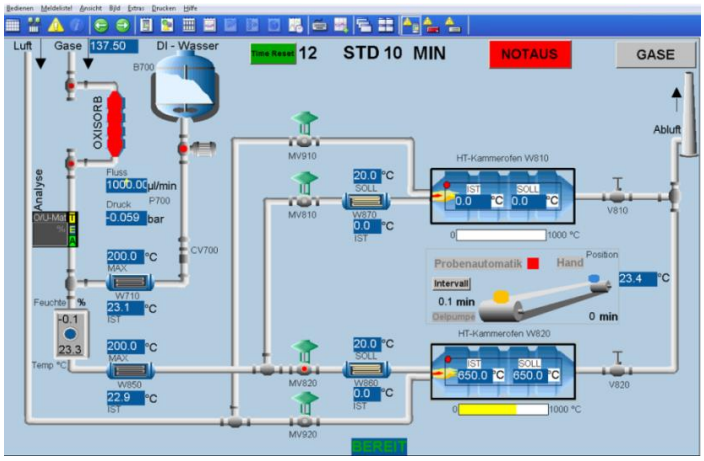

Figure 3.9: The second graphical user interface of the HT test rig

BUPT

The core of the test rig is the oven, with a quartz glass reactor inside, where the samples are exposed to the test environment (see Fig. 3.10).

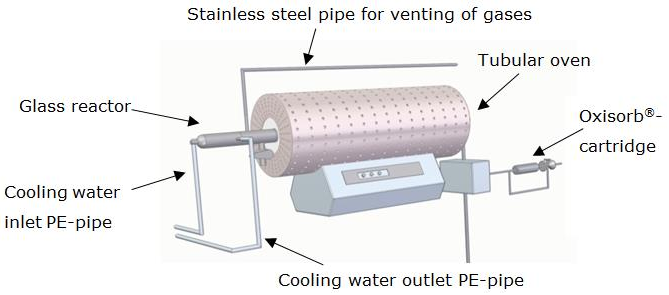

Figure 3.10: Schematic representation (CAD) of the oven with the quartz glass reactor

The whole reactor consists of three different components. The first one is a long quartz glass tube horizontally installed in the oven with conical ends. The second one is a fitting with just one inlet for the gases and is installed on the right side of the long glass tube via mechanical interlock (standard ground). The last component on the left side of the long glass tube is a custom made part. It was produced following specifications from the Westphalian University Gelsenkirchen and handmade at the Technical University in Dortmund. This double hulled glass tube enables the cooling of the exhaust gases with water. Furthermore, this custom made component has a special glass-metal (Kovar) connection. Kovar, a trademark of CRS Holdings, is a Ni-Co-Si-Mn-Fe alloy, designed to be compatible with the thermal expansion characteristics of borosilicate glass ($\sim 5\times10^{-6}$/K between 30 and 200 °C, to $\sim 10\times10^{-6}$ /K at 800 °C) [100]. This glass-metal assembly (pipe section, see Fig. 3.11) was necessary in order to allow direct mechanical connection of the stainless steel pipe that was used to carry exhaust gases to the glass reactor.

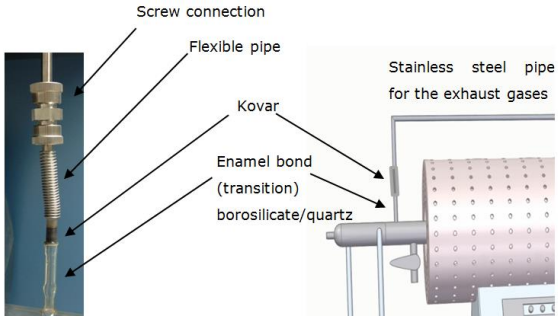

Figure 3.11: The Kovar connection (left) and its placement on the reactor at the outlet side of the high temperature oven (right)

The primary flexible unit of this tube is made of stainless steel and prevents glass breakage during the periodical assembling or disassembling, which is necessary when changing the specimen. In addition, a removable screw connection was selected. It served mainly as a secure opening for the reactor after the exposure of the samples to the metal dusting atmosphere.

BUPT

4. EXPERIMENTS

4.1. Materials Selection

The selection of potential materials for coatings was based on the premise that the self-fluxing powders used, those with a $Cr_{equivalent} \geq 22$, should exhibit a better metal dusting resistance in comparison with materials having a lower $Cr_{equivalent}$. For that reason the self-fluxing powder 15E with a $Cr_{equivalent}$ of 25 from Oerlikon Metco was selected (see Tab. 4.1). A further feedstock powder was selected with a similar $Cr_{equivalent}$, but different matrix (Co base), specifically, the self-fluxing alloy 18C. The third powder, 19E, has a lightly lower $Cr_{equivalent}$ (24), but also contains other elements like W, Mo, and Cu, which possibly could have a positive effect on the metal dusting resistance of Ni based alloys. The chemical composition in mass% and the particle size of the gas atomized powders in µm, defined by the manufacturer of the self-fluxing alloys (15E, 18C, 19E), are listed below.

Table 4.1: Chemical composition (mass%) of the self-fluxing alloys tested

Name	Particle size (µm)	Ni (bal.)	Cr	B	Si	C	W	Co	Mo	Fe	Cu
15E	-106/+45	70,5	17	3,5	4	1	/	/	/	4	/
18C	-125/+53	26,8	18	3	3,5	0,2	/	40	6	2,5	/
19E	-106/+45	64,3	16	4	4	0,5	2,4	/	2,4	4	2,4

The selected self-fluxing alloys (SF) were evaluated with observance of their resistance to metal dusting. Therefore, an experimental plan was established (see Fig. 4.1), further detailed in the following paragraphs.

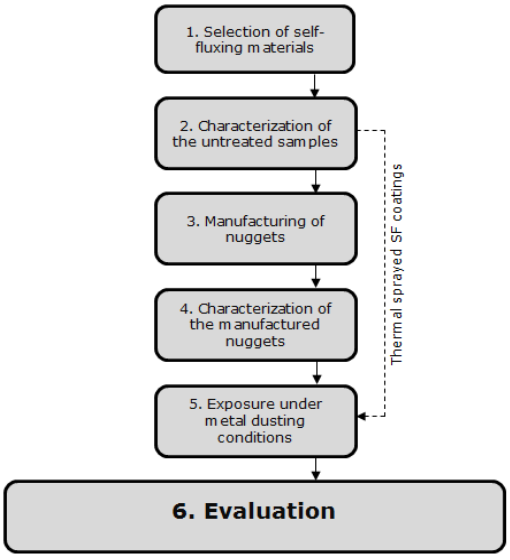

Figure 4.1: Overview experimental plan

After material selection, the priority of the research work was focused on the characterization of the samples in untreated conditions regarding their morphology, structure, and chemical composition. In order to evaluate the influence of the melting process on the metal dusting resistance, the thermal sprayed and fused coatings were compared with "nuggets" made of self-fluxing alloys by melting the feedstock powder with the help of either an inductor or a vacuum oven.

4.2. Sample Manufacturing and Process Parameters

For the exposure of the self-fluxing alloys under metal dusting conditions, it was necessary to manufacture melted samples. Therefore, available or accessible methods - also applied in the industry - were used. These included the thermal spray process with a subsequent flame fusing, and the direct melting of powders into nuggets in a vacuum furnace or with the aid of an inductor. The processes and the general approaches are described in the following pages.

4.2.1. Thermal Sprayed and Flame Fused Self-Fluxing Samples

For the production of self-fluxing coatings, the company Karl Schumacher GmbH & Co. KG coated cylindrical steel substrates (Ø12 mm) with the three previously described self-fluxing powders, using thermal flame powder spraying (DIN EN 657). The thermal powder flame spraying is illustrated below in the schematic in Fig. 4.2 [101].

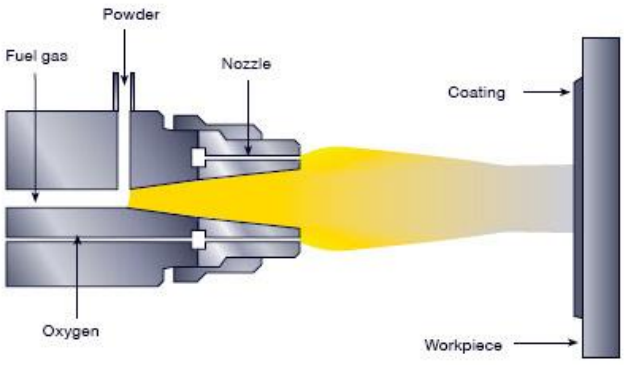

Figure 4.2: Schematic representation of thermal powder flame spraying process

There are many alloys that cannot be produced in a wire or rod-shape form. For that reason, the thermal flame powder spray process was developed. A heat source, generated by a chemical reaction between oxygen (O_2) and acetylene (C_2H_2), produces a gas stream with a temperature of more than 3000°C. The powder has to be fed into the flame. This leads to the acceleration of the powder particles and deposition on the substrate surface [101].

BUPT

Before the flame spraying, the surfaces of the steel substrates were blasted with steel shot (particle size max. 1.5 mm) for a better bonding of the self-fluxing alloys. The company, for reasons of confidentiality, did not disclose the parameters used for the thermal spray process. Typical parameters for the coating with self-fluxing alloys are 12-14 l/min. C_2H_2, 25-29 l/min. O_2 with a spraying distance of 150-250 mm between the nozzle and the surface of the substrate. The average thickness of each coating was 1.2 mm. After the posterior fusing process by an oxyacetylene flame (the medium time for the remelting process was 15 minutes.), the layer thickness was reduced to 1.1 mm, because the coating became more compact. An example for the thermal sprayed self-fluxing material 15E is shown in Fig. 4.3. The LM micrographs reveal a high degree of porosity (see Fig. 4.3, left), which is typical for these coatings in the as sprayed status. Moreover, one can observe that the particles have a round flat shape and were only partially, not fully, melted during the spraying process. After fusing with an oxyacetylene flame, the coating was almost dense and completely homogenous (see Fig. 4.3, right).

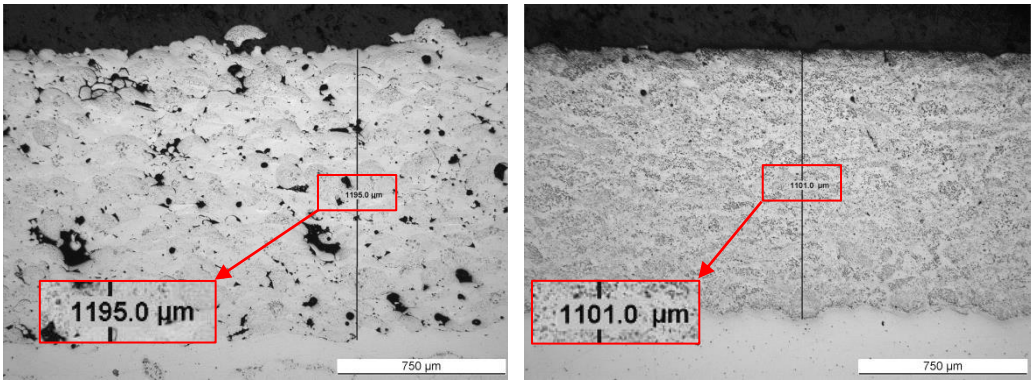

Figure 4.3: LM micrographs of the 15E thermal sprayed coating before (left) and after the flame fusing process (right)

In order to investigate the thermal sprayed and remelted coatings as self-standing bodies like the nuggets produced by fusing only the powders, the carbon steel was spark-eroded in oil. SEM investigations revealed that the electrical discharge machining had no impact on the microstructure of the samples.

4.2.2. Vacuum Oven Melted Self-Fluxing Samples

The most important benefits of the vacuum oven are the degassing during the process and the possibility to program exact parameters, such as the heating-up, holding and cooling-down times, as well as the exposure temperature. For this treatment, 5 g of the powder were weighed and filled in a ceramic crucible with a size of Ø3.5 x 5 cm (see Fig. 4.4 left). This crucible was refractory lined with a glass fiber mat to prevent the powder from caking on the ground of the crucible. In order to avoid the exhausting of the powder out of the ceramic crucible through the vacuum pump, a further smaller conical ceramic crucible, with the function of a cap,

BUPT

was covered with a glass fiber mat and then inserted in the crucible with the powder, as illustrated in Fig. 4.4 right.

Figure 4.4: Ceramic crucible, refractory-lined with a glass fiber mat (left) and sealed ceramic crucible with the powder (right)

Unfortunately, the producer did not offer any data about the melting interval of the self-fluxing powders. For that reason, the respective melting interval of the powders has to be identified by using Differential Thermal Analysis (DTA). The laboratory equipment used was the thermogravimetric analyzer model STA 449 F1 Jupiter from the company Netzsch. As explained before, the temperature oscillation will appear as a peak in a DTA-diagram. The lowest value for the melting interval of the three samples was recorded for the powder 19E at around 980°C (see the first peak from left in Fig. 4.5), closely followed by that of the powder 15E at 992°C.

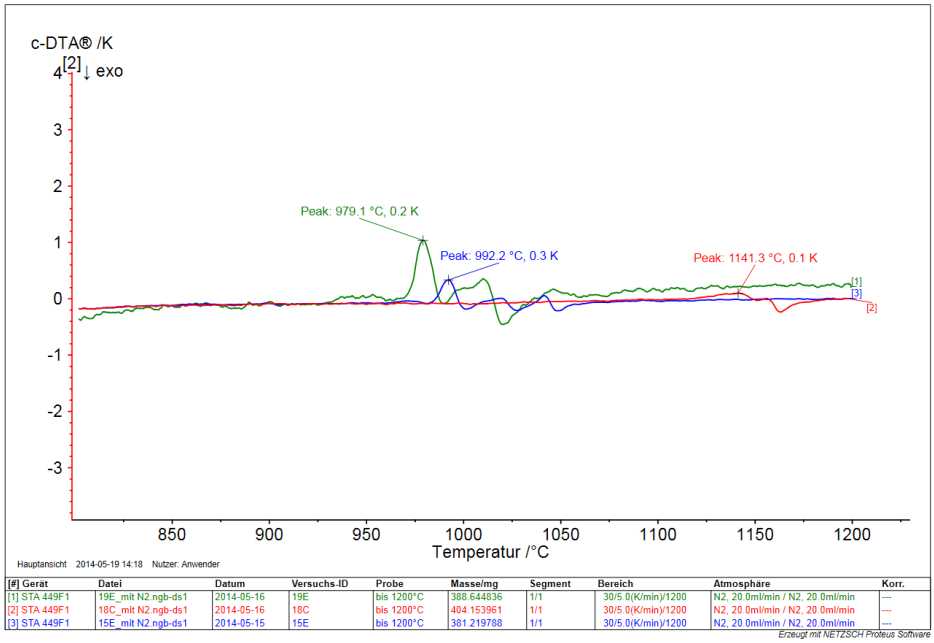

Figure 4.5: DTA-curves of the feedstock powders tested

BUPT

The highest value for the liquidus point was noted for the powder 18C at 1140°C. This result confirmed expectations, because this powder had a high content of cobalt (40 mass%) in the chemical composition. The element cobalt has a melting temperature of 1495°C. In contrast, Ni has a melting point of 1455°C. However, the main reason was the 6 mass% Mo in the powder 18C. This element has a melting point of 2623°C.
Based on the results of the DTA, the chosen temperature for the melting process of the three powders in the vacuum oven was approximately 20-30 °C higher in comparison with the measured one. That was a recommendation of the powder manufacturer. Fig. 4.6 shows an exemplary screenshot of the written program (test run) for the exposure of the powder Oerlikon Metco 15E in the vacuum oven.

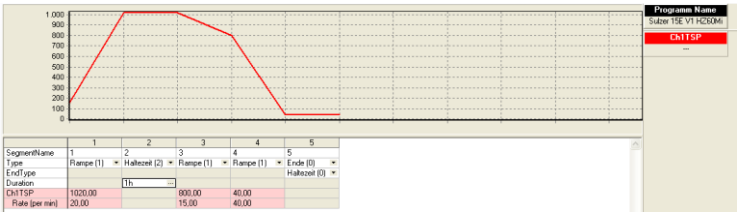

Figure 4.6: Screenshot of the graphic display of the written program (test run)

After reaching a stable high vacuum (10^{-5} mbar), the powder was heated-up at a rate of 20°C/min. This meant, a heating-up time of about 51 minutes was needed in order to reach the temperature, determined with the DTA. In order to achieve a uniform phase distribution, the sample was slowly cooled at a rate of 15°C/min. down to 800°C. Afterwards, with the aim of alloy solidification with a uniform phase distribution, the cooling rate for the test run was more than doubled, until the room temperature was reached. During the exposure in the vacuum oven, the programmed parameters of the test run were constantly monitored (see Fig. 4.7).

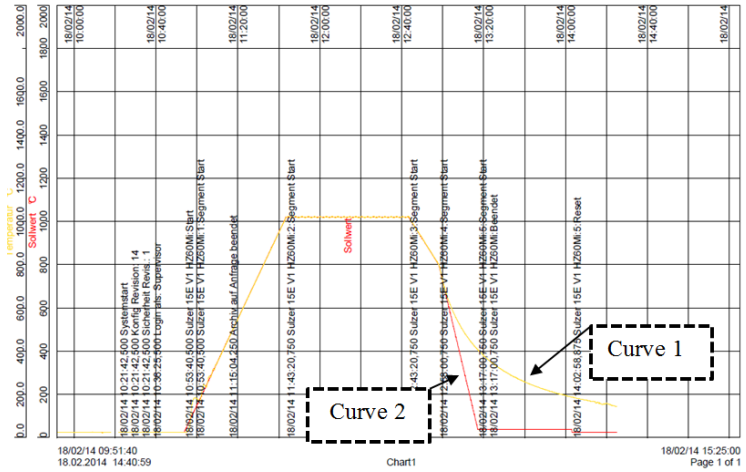

Figure 4.7: Control protocol for the exposure of the 15E sample in the vacuum oven

BUPT

It can be seen that the actual value for the temperature (Curve 1) deviates from the set point (Curve 2) only in the range of the second cooling ramp, starting at 700°C with a parabolic course. This is solely due to the fact that the programmed cooling rate could not be achieved with the hardware that was used. However, as Mr. Gottmann from the company Oerlikon Metco (formerly: Sulzer Metco) states, the cooling rate for NiCrBSi powders independent of the chemical composition should be between 5 - 15°C, in order to avoid stresses followed by cracks in the coating (here: "nuggets").
In order to determine the average cooling rate, a secant was drawn between the start and the end point of the parabolic curve in the control protocol for the exposure of the 15E sample in the vacuum oven (see Fig. 4.8).

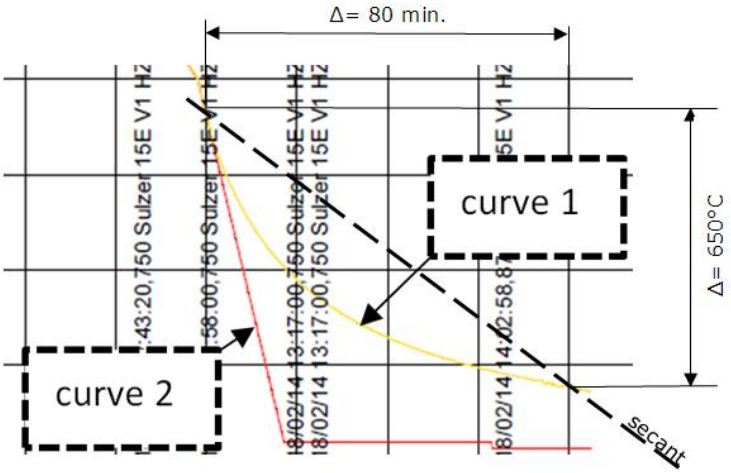

Figure 4.8: Section of the control protocol with the parabolic cooling curve

The delta values (differences) for the temperature as a function of the time, offered a cooling rate of 8°C (minimum), thereby in compliance with the statement of the company Oerlikon Metco.

The main task of the melting process was to produce nuggets with a low porosity value of most 0.5%, which corresponds to the average porosity of the thermal sprayed and flame fused coatings.
For the determination of the porosity of the samples, they were embedded in bakelite, ground with 4000 grain SiC, and polished with a 3µm diamond suspension, before being cleaned with ethanol and dried with hot air.
For the quantification of the porosity, the Leica light microscope in combination with the image processing program "Leica Qwin" was used. This program makes it possible to determine the pores through differences in contrast. The pores were identified as a dark grey color whereas the color for the rest of the sample was much lighter. Through adjustment of the sensitivity, the program was able to detect only the areas with the greyscale corresponding to the pores.

BUPT

For the determination of the average porosity for all samples, three individual measurements were done in different regions of each sample. An example of such a measurement is given in the Fig. 4.9.

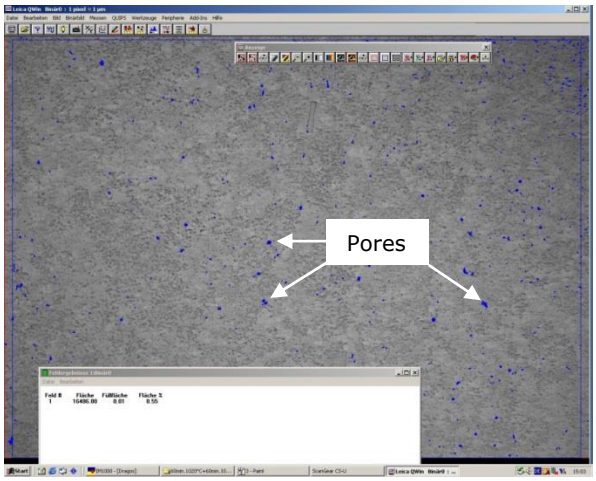

Figure 4.9: LM micrograph used for porosity measurement; the pores are colored blue

The parameters used for the melting tests and the porosity for all samples made of the three feedstock powders are given in the following table. The holding time for the powder treatment was between 60 and 180 minutes (see Tab. 4.2). The heating rate (20 °C/min.), the cooling rate (8 °C/min.), as well as the pressure (10^{-5} mbar) in the vacuum chamber were constant for all tests.

Table 4.2: Parameters and results of the vacuum melting tests

No.	Powder	Dwell time [min.]	Temperature [°C]	Porosity [%]
1	15E	60	1020	1,42
2	15E	60	1050	0,47
3	15E	60	1070	0,66
4	15E	120	1020	1,07
5	15E	120	1050	**0,21**
6	15E	180	1020	1,25
7	15E	180	1050	0,28
8	18C	120	1120	not molten
9	18C	120	1160	1,16
10	18C	120	1200	**0,5**
11	19E	120	1000	1,68
12	19E	120	1020	0,75
13	19E	120	1040	**0,34**

BUPT

For the first melting test of the powder 15E, the chosen temperature (1020°C) was about 20°C higher than the temperature (992°C) determined by means of DTA-analysis. The measured porosity (1.42%) of the nugget obtained from the powder 15E was still not satisfactory. For this reason, the main parameter that had to be modified was the exposure temperature. For the powder 15E it was increased up to 1070°C. For further tests, the melting period was doubled and tripled. After a series of experimental tests concerning the optimal vacuum melting of the powder 15E, the best results were achieved at 1050°C at a time of 120 minutes. This sample was selected for subsequent exposure under metal dusting conditions.
With respect to the higher liquidus point (1141°C) of the powder 18C, an adjustment of the parameters was applied. It was confirmed that the temperature used (1120°C), around 20°C below the liquidus point determined by means of DTA, was not sufficient in order to remelt this powder. Even temperatures of 1160°C only led to a minimal fusing of the powder particles without any compaction. A lower porosity of 0.5% (sample no. 10) was achieved at 1200°C. Since the temperature of 40-60°C above the liquidus temperature determined by the DTA analysis and the holding time of 120 minutes were confirmed as the most suitable parameters for the melting of the powder 15E and 18C, these were also chosen for the last powder 19E. The sample obtained with these treatment parameters exhibited a porosity of 0.34% (sample no. 13).

4.2.3. Inductively Melted Self-Fluxing Samples

Another wide spread method that is used to remelt self-fluxing alloys is induction heating. The functionality of the inductive heating process is based on the principle that an alternating current generator produces a magnetic field in a primary coil, which is part of an inductor (see Fig. 4.10).

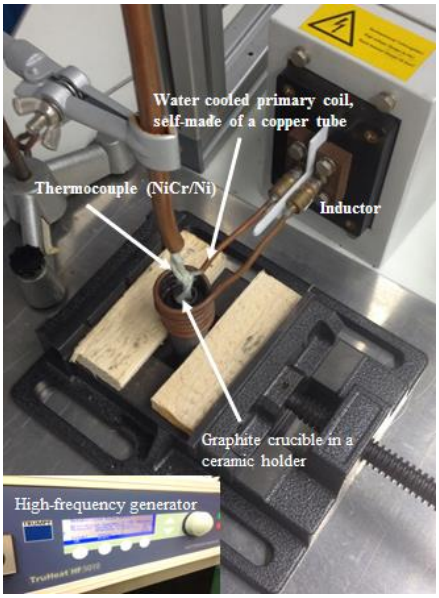

Figure 4.10: Induction heating system

BUPT

This magnetic field induces the voltage in the workpiece. This process generates a direct heating of the sample (see Fig. 4.11).

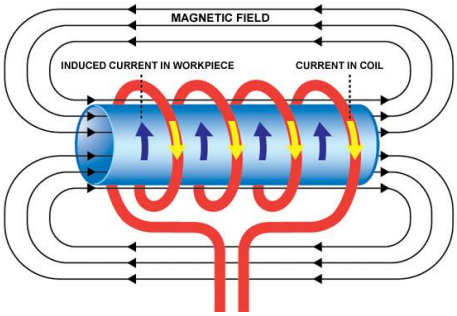

Figure 4.11: Schematic representation of the fundamentals of induction heating [4]

The big advantage of induction heating is the possibility to generate the heat only in the sample without using any external heat source. This method not only spares the environment, but also saves supplementary costs, which could be generated due to current high energy prices. Another major advantage of using such a high-frequency inductive heating system is the exact adjustment of the heat penetration depth. Such a high frequency inductive heating system from the company Trumpf (Germany), model TruHeat HF 5010 (max. 35A, 50 – 450 kHz), together with the above-described peripheral equipment, was used in this work.
There were no accessible parameters (time and current) in the literature for the melting process of self-fluxing powders in a graphite crucible. Referring to the statement of Mr. Krauss from the company Trumpf, there are many factors that may have an influence on the results of the sample quality. These include the geometries of the graphite crucible, the chemical composition of the powders used, or the installed condensers in the inductor. Normally, the condensers have to be adapted to the individual application with consideration for the treatment time and temperature. However, for the tests in this work, the time and current were adapted to the present condensers. For this purpose, preliminary tests were conducted with 1 g of the powder. The powder was placed in a small graphite crucible. This kind of crucible is typical for operational temperatures between 400 and 1400°C. Before each test, the crucible was placed in the same position with the aid of a ceramic holder inside the copper coil.

A rough approximation of the process parameters was done as a first step, with respect only to a visual examination of the surface texture. A high level of porosity was evidence of an incomplete melting process. In a further step, the value for the electric current was increased. In some situations, the crucible jumped out of the copper coil, because of the rapidly growing magnetic field (Lorenz force in magnetic field). Therefore, it was necessary to decrease the value of the applied current for the following tests. Under the newly established conditions, it was necessary thereafter to modify another parameter, namely the treatment time, which was increased. Only one parameter in each test was changed. Based on these results, a selection of parameters for all powders was defined. The way the applied parameters were selected for each of the three powders is summarized in table 4.3.

BUPT

The decisive result concerning the characteristics of the obtained nuggets was, as mentioned before, the internal porosity, analyzed by means of light microscopy in combination with the software "Leica Qwin" (compare chapter 4.1.2).

Table 4.3: Parameters of the inductive melting process and the degree of internal porosity of the obtained samples

15E No.	C* [A]	PD* [sec.]	P* [%]	**18C No.**	C* [A]	PD* [sec.]	P* [%]	**19E No.**	C* [A]	PD* [sec.]	P* [%]
1	25	1	0,31	10	30	2	**1,99**	19	25	1	12,22
2	25	2	1,06	11	30	2,5	3,63	20	25	2	2,12
3	25	3	6,09	12	30	3	12,1	21	25	3	4,69
4	27,5	1	**0,29**	13	32,5	2	3,43	22	27,5	1	5,84
5	27,5	2	1,15	14	32,5	2,5	7,56	23	27,5	2	0,65
6	27,5	3	9,24	15	32,5	3	6,59	24	27,5	3	7,37
7	30	1	0,86	16	35	2	2,88	25	30	1	6,07
8	30	2	2,45	17	35	2,5	4,78	26	30	2	**0,37**
9	30	3	5,66	18	35	3	8,19	27	30	3	7,46

*) C= current, PD= pulse duration, P= porosity

The lowest sample porosity was obtained for the melted 15E powder with applied pulse duration of one second and 27.5 Ampere. A similar result for the porosity was achieved for the self-fluxing material 19E. Unfortunately, the best parameters for the melting tests of the powder 18C resulted in a porosity of about 2%. Based on these findings, one can assume that either this kind of melting process or the existing hardware is not suitable for melting of Co based self-fluxing materials.
The process temperature during the melting process of the powders with the inductor was measured by using the data logger (multimeter) Almeno 2290-8 from the company Ahlborn in combination with a Ni-Cr/Ni thermocouple for a temperature range between -270 and 1380°C. The measured temperatures were between 1240°C and 1370°C. However, it should be mentioned that the multimeter used is not very suitable for such applications. The first limitation was the maximum temperature. It could not be clearly established if the measured temperature was in agreement with the real temperature due to the upper measuring limitation of the multimeter. Moreover, with the data logger used, it was only possible to record one value per second. Due to this, it is clear that the probability of registering the precise temperature was rather low, especially because of the fast cooling rate. A temperature measurement over a longer time revealed that the sample cooled down very quickly. The powder sample 18C needed just 21 seconds to cool down from 1244°C to 650°C. In total, it took less than 3 minutes to reach 100°C. However, the cooling time down to room temperature was longer than expected and was still not reached even after six minutes, probably due to the heat storage in the graphite crucible.

BUPT

4.3. Exposure in the HT Corrosion Test Rig

Authors Chun et al. [23] and Nishiyama et al. [25] found out that the maximum rate of carbon transfer from CO–H_2 mixtures occurs at the 50CO:50H_2 composition. Because of this reason, all samples were exposed in a N_2/CO/H_2 (80:10:10) gas mixture. Due to the high costs of pure CO, an N_2/CO-test gas with 90 vol% N_2 and 10 vol% CO was used. For the right ratio of vol% for CO and H_2 (50:50), 250 ml of the test gas N_2+CO and 25 ml H_2 were combined.

Samples like the eroded self-fluxing coatings, as well as all selected nuggets with the lowest porosity, which were melted in the vacuum oven or with the inductor, were ground with abrasive SiC-paper (grain size 4000), polished with a 3µm diamond suspension, cleaned with ethanol (C_2H_6O), and then blow dried. After that they were positioned in a ceramic boat with the ground surface on top. At the beginning of each test, the quartz-glass reactor of the HT test rig with the stored samples was purged with N_2 for 24 hours, in order to eliminate the residual oxygen. After this process, the Oxisorb cartridge and the CO- and H_2-gas flow were activated, whereas the N_2-gas flow was stopped. After 11 hours in test 1 or 12 hours in test 2, the oven was heated up to 650°C within 15 minutes (automated). The parameters used are shown in Tab. 4.4. The results of the tests are discussed in the following chapter.

Table 4.4: Parameters for the exposure of the samples in the HT test rig

	Purging with N_2		**Forerun Flow rate**			**Pressure [bar]**		**Flow rate [ml/min]**		**T [°C]**	**Process time [h]**
Test	Time [h]	Flow rate [ml/min]	Time [h]	N_2+CO (10% CO) [ml/min]	H_2 [ml/min]	N_2+CO (10% CO) [ml/min]	H_2 [ml/min]	N_2+CO (10% CO)	H_2		
1	24	2000	11	250	25	1,00	1,00	250	25	650	**513**
2	24	2000	12	250	25	1,00	1,01	250	25	650	**1019**

The carbon activity, which was calculated by the using of the thermodynamic calculation software HSC Chemistry version 7, was 21.

BUPT

5. RESULTS AND DISCUSSION

This study was conducted in order to evaluate the resistance of different fused self-fluxing alloys against metal dusting attack. The samples chosen were selected based on the high Cr and Si contents in their chemical composition.
The focus of this work was mainly on the influence of the element Si in self-fluxing alloys with consideration for its positive effect on the metal dusting resistance, the distribution in the sample, and the interaction with the accompanying elements.

5.1. Morphology, Chemical and Physical Properties of the Materials

The selected gas-atomized (in N_2) standard self-fluxing feedstock powders, the melted nuggets, made of these same powders in a vacuum oven or with an inductor, as well as the thermal sprayed and flame fused coatings, were examined by means of scanning electron microscopy (SEM) combined with energy dispersed X-ray analysis (EDX). The magnification for the investigation of the powder particles, and the structure of the coatings and nuggets in cross section, varied in the range between 200x and 3000x. A lower magnification (30x-50x) was used only for a clear presentation (overview) of the samples that were exposed to metal dusting conditions. The chemical composition of the self-fluxing feedstock powders was verified by means of X-ray fluorescence spectrometry (XRF). Additionally, the phase composition of the feedstock powders, and that of the melted samples (coatings and nuggets), was determined by means of X-ray diffraction (XRD).

5.1.1. Self-Fluxing Feedstock Powders

At the beginning of the study, the chemical composition was verified by means of XRF-technique. As mentioned in chapter 3, only elements with an atomic number ≥ 11 (from Na) in the periodic table can be detected. That means that B and C could not be determined with this method. Due to this reason, the B and C mass% content was proportionally distributed to the other elements during the quantitative analysis using the software X-Lab Pro. The mean values derived from three single measurements, rounded to one decimal place, are displayed in the following table 5.1. The standard deviation according to the measurement report is less than 0.1%.

Table 5.1: Chemical composition of the self-fluxing feedstock powders used, determined by means of XRF

Powder	Ni	Cr	B	Si	W	Co	Mo	Fe	Cu
15 E	74,4	17	3,5	4,2	/	/	/	4,4	/
18 C	29,4	19	3	3,8	/	39	6,6	2,2	/
19 E	69,3	15,7	4	3,9	2,2	/	2,4	4	2,5

When compared with the information given by the manufacturer, the measured chemical compositions showed only a slight deviation from the original values. Total conformity was not expected because the elements are randomly distributed in the powder particles.
The SEM investigations, depicted in Fig. 5.1 – 5.3, confirmed the information of the manufacturer that the feedstock powder particles have a spheroidal shape, which reduces their tendency to agglomerate. This means they are less likely to obstruct the feed unit of the flame-spraying system, and also exhibit low friction movement. Furthermore, it could be established that the particle size is also in accordance with the data of the manufacturer (see the particle size for each powder in Tab 4.1). The measurements done at the Oerlikon Metco Company for larger particle sizes conformed to sieve analysis norm ASTM B214. Particle size smaller than 45 µm was determined by means of laser diffraction [102].

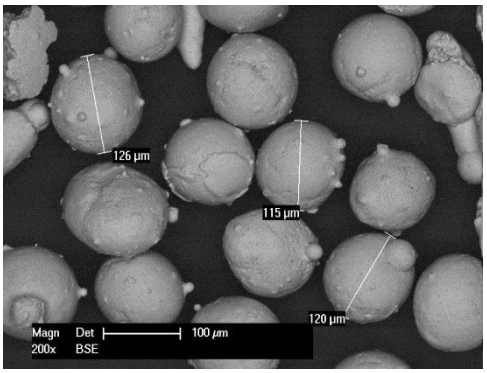

Figure 5.1: SEM micrograph powder 15E

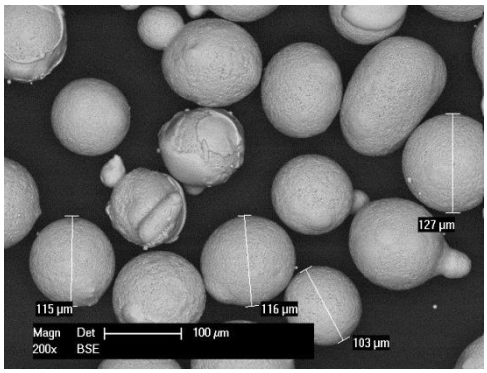

Figure 5.2: SEM micrograph powder 18C

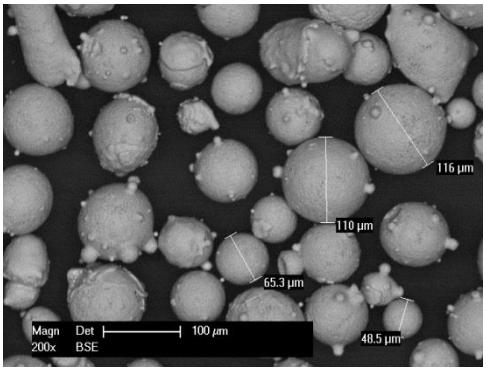

Figure 5.3: SEM micrograph powder 19E

For cross section observations, the powders were individually embedded in Bakelite, ground with 4000 grain SiC, and polished with a 3µm diamond suspension. Finally, the prepared cross section samples were cleaned with ethanol and dried with hot air. The SEM-micrographs presented in Fig. 5.4 – 5.6 reveal different intensities of grey areas. Based on the method of data presentation for the backscatter detector, one may assume that the local chemical composition differs from one shade of grey to another. Some chemical analyses were done with the EDX detector, which revealed that the dark grey areas in the powder particles 15E and 19E were borides,

BUPT

whereas the light dark greyscale signified the carbides. The constitution of the carbides and borides is illustrated in Fig. 5.7. Due to the higher atomic mass of C (12.01 u) in comparison with B (10.811 u), the carbides appear brighter than the borides in the BSE detector. The silicides have the same contrast as the matrix.

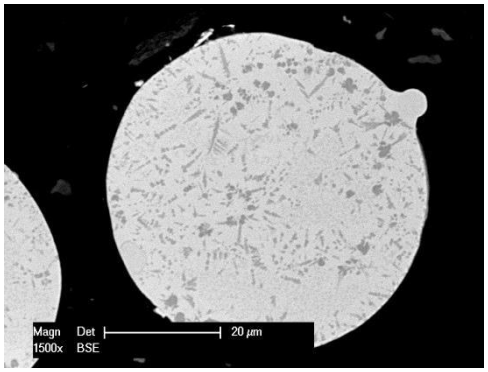

Figure 5.4: Cross section of the powder 15E

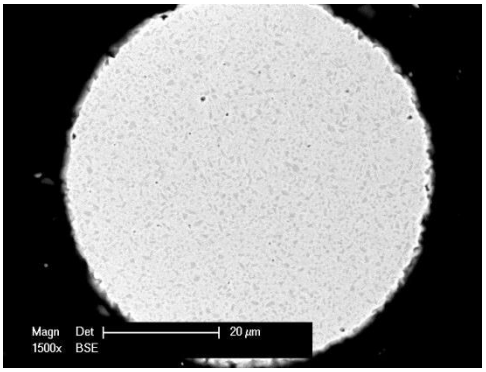

Figure 5.5: Cross section of the powder 18C

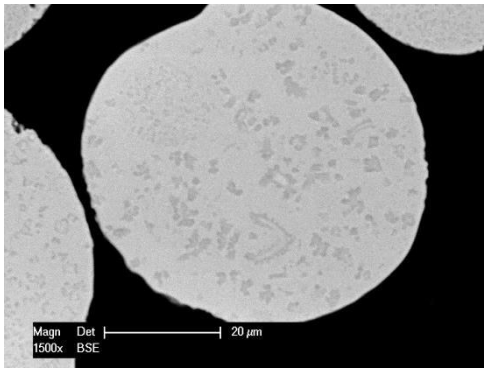

Figure 5.6: Cross section of the powder 19E

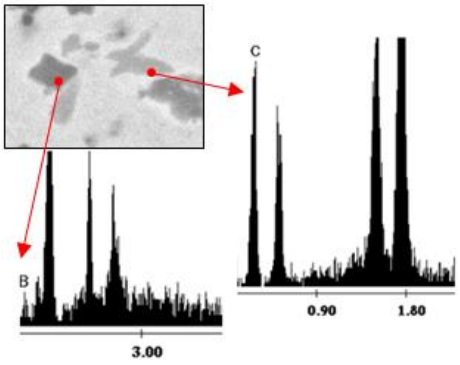

Figure 5.7: EDX analysis of the powder 19E

The determination of the phase composition of the three feedstock powders was accomplished by means of XRD. Due to the requirement that the base for the quantitative and qualitative analyses should be the same, only the elements Ni, Cr, B, Si, C, Fe (and Co for the powder 18C) were taken into account. This consideration was perfectly sufficient, because the focus of this work was mainly on the Si containing phases.

As stated in the literature, the ternary Ni-Cr-B alloy system has a multi-phase structure consisting of a solid solution of chromium in nickel γ – Ni(Cr), nickel borides Ni_3B, and borides of chromium, such as CrB, Cr_2B, or Cr_5B_3. However, up to 4 mass% Si and up to 1 mass% C in standard NiCrBSi alloys makes the phase constitution more complex (see chapter 2.7.1). Beside the signals for Ni and borides, the analysis of the XRD pattern (see the example in Fig. 5.8) for the

BUPT

powder 15E reveals two Si containing phases: 14 mass% Ni_3Si and 7 mass% Fe_5Si_3, as well as 12 mass% Cr_3C_2. (Fig. 5.9).

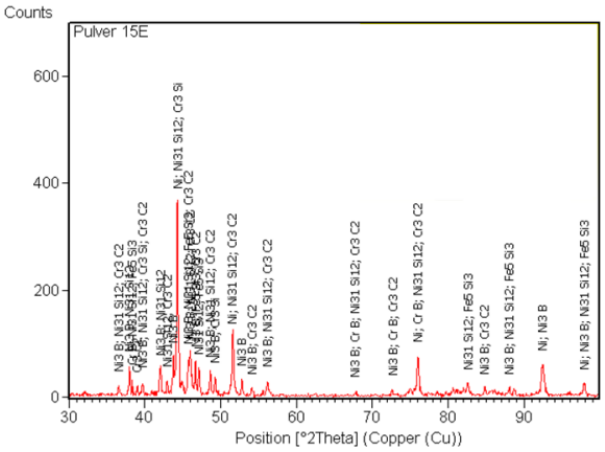

Figure 5.8: XRD pattern for the powder 15E

The carbides were detected only for the self-fluxing feedstock material 15E, which can probably be attributed to the high content of C (1 mass%). The increasing content of chromium carbide precipitates for self-fluxing materials with more than 0.8 mass% C was already described by Mrdak [83], as mentioned in chapter 2.7.1. The evaluation of the XRD patterns for the three feedstock powders 15E, 18C and 19E is illustrated in the following figure.

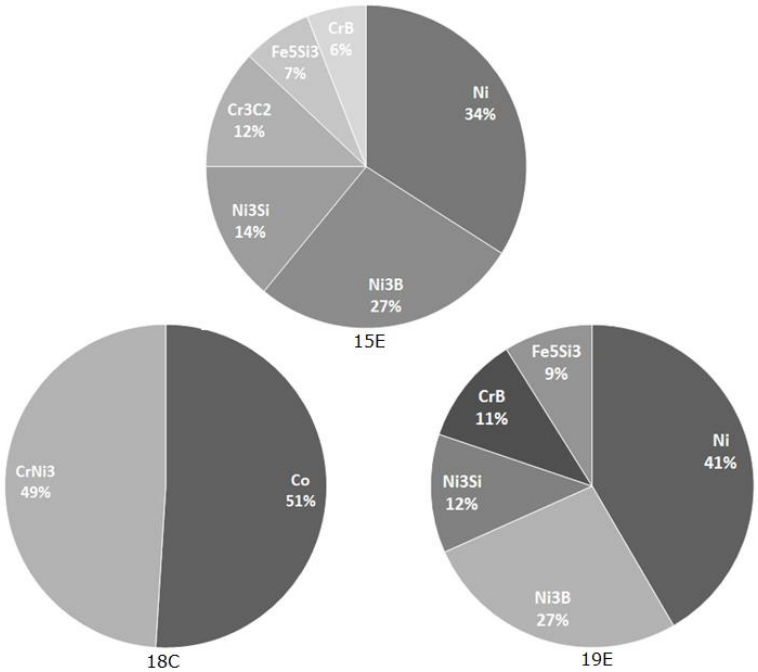

Figure 5.9: Quantification charts of the three powders 15E, 18C and 19E

BUPT

These results are the reference base for further comparison with the thermal sprayed and flame remelted samples, as well as the vacuum and inductively melted samples.

5.1.2. Thermal Sprayed and Flame Fused Coatings

The structure of the thermal sprayed and flame remelted coatings is presented in the following SEM micrographs Fig. 5.10 – 5.12.

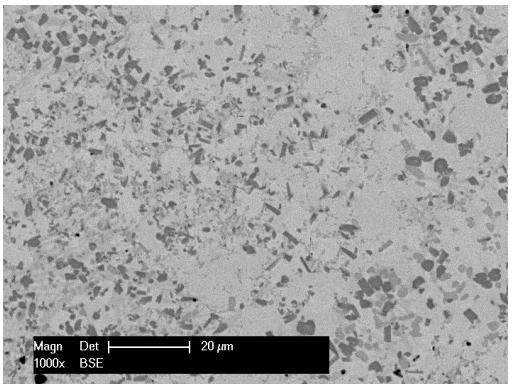

Figure 5.10: Structure of the thermal sprayed and flame fused 15E coating (SEM)

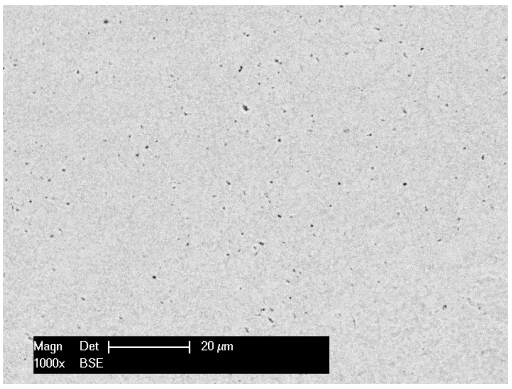

Figure 5.11: Structure of the thermal sprayed and flame fused 18C coating (SEM)

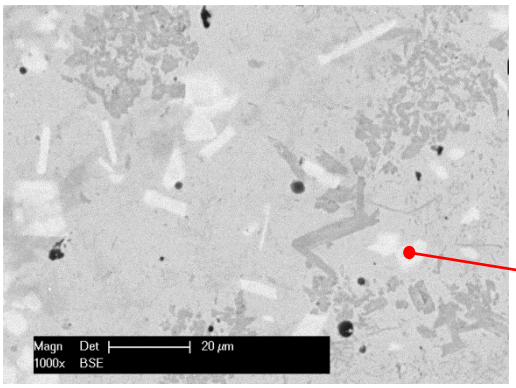

Figure 5.12: Structure of the thermal sprayed and flame fused 19E coating (SEM)

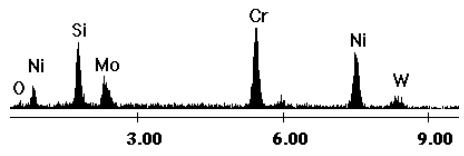

Figure 5.13: EDX analysis of the light grey phases from the thermal sprayed and flame fused sample 19E

The SEM investigations revealed that the thermal flame spraying and the posterior fusing process with an oxyacetylene flame had a definite influence on the phase structure of the self-fluxing materials. For further discussion, it is necessary to mention that the dark grey areas depicted on the SEM micrographs of the coatings 15E and 19E are borides, whereas the slightly lighter greyscale, in comparison with the greyscale of borides, reflects the carbides (see the EDX analysis for the

BUPT

powders). A further comparison of the coatings microstructure revealed that the amount of C- and B-containing phases was considerably reduced for the self-fluxing material 15E after the thermal spraying and posterior fusing process. This is very advantageous, because hardened phases such as C- and B- containing phases generate a notch-effect, due to the needle-like geometry, especially in the case of micro dislocations. This fact is well known and therefore one can expect that the strength of the material will be dramatically reduced. The fine structure of the self-fluxing material 18C (Co based) appeared unchanged after the coating and fusing process. The SEM-microscopy combined with the EDX analysis of the self-fluxing material 19E also confirmed the presence of W-and Mo- containing phases (light grey, see Fig. 5.12). These phases could not be observed in the SEM-microscopy of the powders, because the elements were dissolved in the matrix. The W- and Mo-rich phases were first formed during the coating process. The results obtained from the XRD-analyses of the coatings concur with the statements of Kima [88] and Borisov [81]. The Cr silicides in the sample 15E and the Co silicides in the remelted sample 18C, respectively, were first formed after the fusing process. In later chapters, there is a detailed description of why this fact has a considerable influence on the corrosion behaviour of the exposed samples under metal dusting conditions. The results of the quantitative XRD analysis for the three fused coatings are given in figure 5.14.

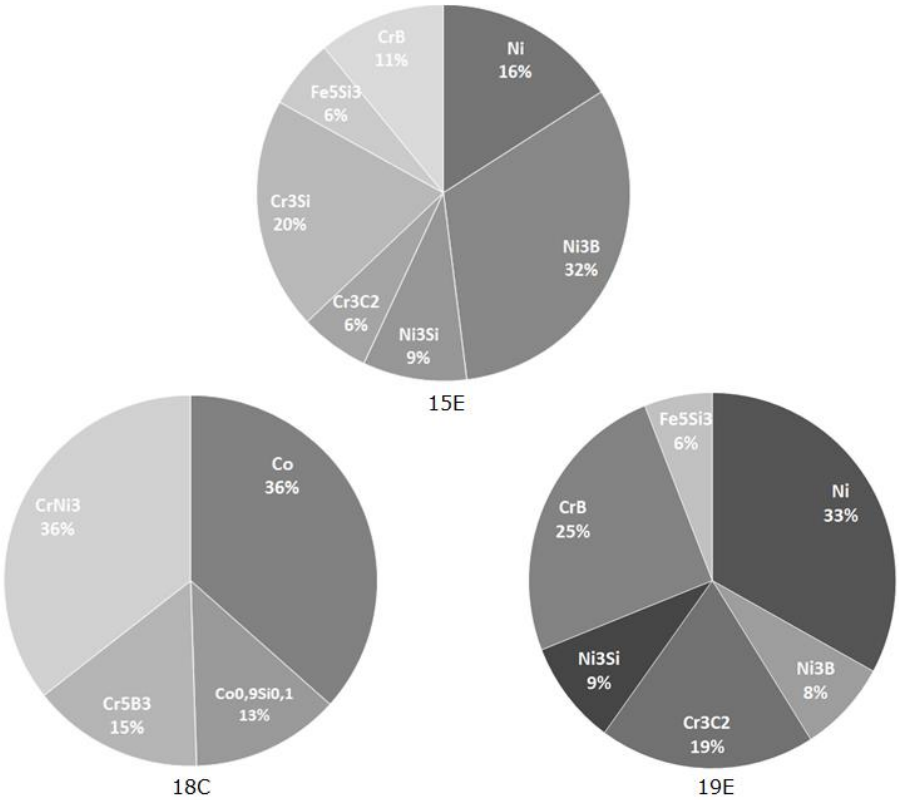

Figure 5.14: Quantification charts of the three thermal sprayed and flame fused coatings

BUPT

5.1.3. Vacuum Melted Samples

The structures of the three samples melted in the vacuum oven, observed at a magnification of 1000x (SEM-microscopy; BSE), are shown in the following Fig. 5.15 – 5.17.

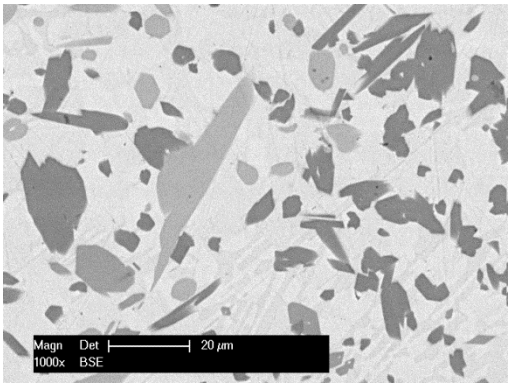

Figure 5.15: Structure of the vacuum melted sample 15E

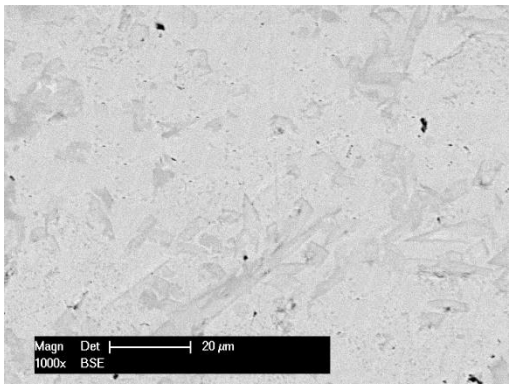

Figure 5.16: Structure of the vacuum melted sample 18C

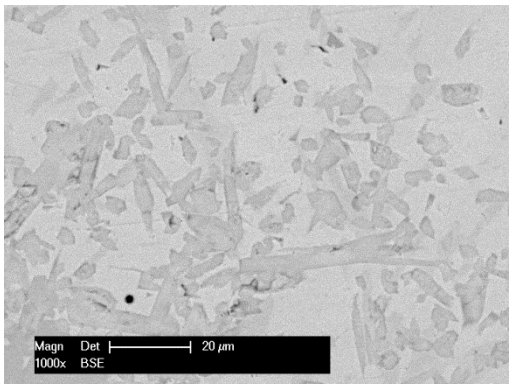

Figure 5.17: Structure of the vacuum melted sample 19E

The information already reported for the powder or flame fused coatings, regarding the correspondence between the greyscale and the phase composition, is still available and applicable for the present samples. The SEM micrograph of the sample 15E clearly reveals the distribution of the carbides (c) and borides (b) in the matrix.

BUPT

The quantification charts determined from the XRD measurements of all three vacuum melted self-fluxing feedstock powders are presented in the following figure.

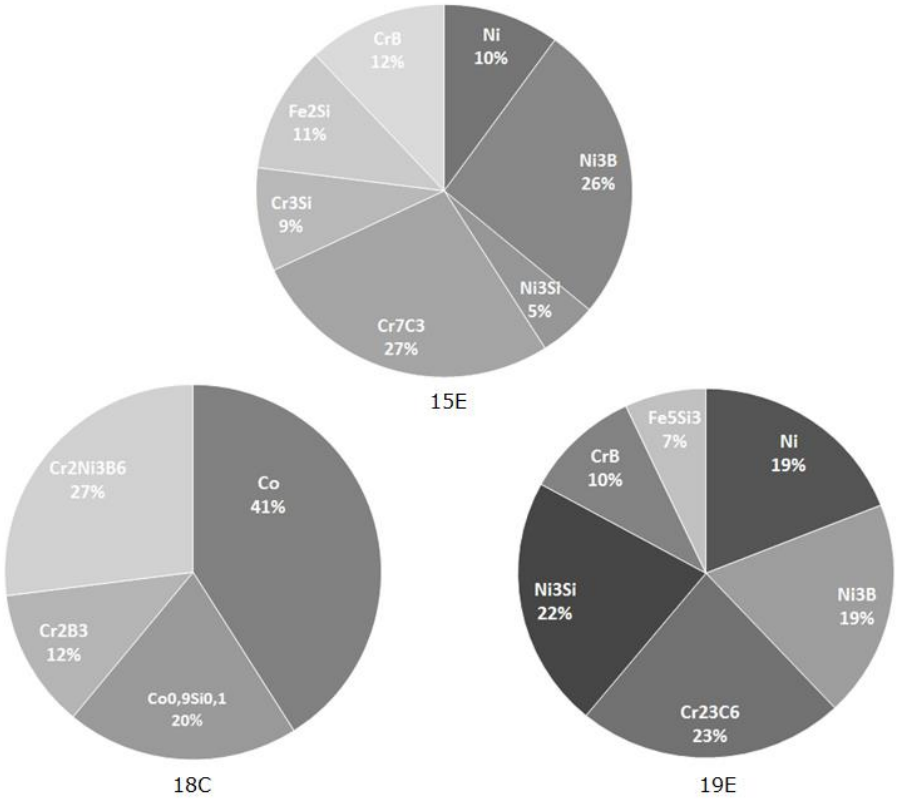

Figure 5.18: Quantification charts of the vacuum melted nuggets

The evaluation of the quantification chart for the sample 15E revealed that 9 mass% Cr_3Si was formed. Furthermore, there was a modification of Fe_5Si_3 to Fe_2Si, therefore an enrichment of the intermetallic phase with Si after the melting process occurred. The amount of borides did not change significantly. However, there was also a modification of Cr_3C_2 (carbide in the powder) into Cr_7C_3. According to Bürgel [40], this kind of carbide-modification with a complex hexagonal lattice structure is stable in the temperature range between 1100°C to 1150°C. At lower temperatures <1050°C it converts into $M_{23}C_6$ and then its structure becomes complex cubic. These phases appear round or lamellar. The manifestation of Cr_7C_3 is a blocky shape. The high amount of Cr_7C_3 (27 mass%) for the sample 15E explains the presence of many block-like phase fractions (see SEM micrograph in Fig. 5.15).
In contrast, one can observe in the SEM micrograph (Fig. 5.16) of the vacuum melted 18C sample that almost none of these block-like phases are present. This statement can be confirmed with the results of the XRD analysis. No carbides were identified for the XRD pattern of the vacuum melted feedstock powder 18C. This result was not surprising, because of the low carbon content of 0.2 mass%. As mentioned before, Mrdak [83] confirmed that such chromium carbide precipitates are formed in self-fluxing materials with more than 0.8 mass% after the remelting process. Instead of carbides, the XRD analysis identified many borides.

BUPT

Less remarkable are the formed silicides $Co_{0.9}Si_{0.1}$ (20 mass%). It appears that this phase will be formed only after the fusing process, like the Cr-silicides. For the melted 19E sample, no major changes were noted with respect to the amount of borides. However, comparing the structures of the powder and the vacuum melted sample, one can note that the fusing process led to a considerable growth of the borides. A particularly conspicuous aspect is the formation of the $Cr_{23}C_6$ phases, although the feedstock powder 19E has a relatively low C content (0.5 mass%). This contradicts the theory of Mrdak [83] that Cr carbides will only be formed if the C content is at least 0.8 mass%. A plausible hypothesis may be the long exposure time in the vacuum oven, which promoted the formation of 23 mass% $Cr_{23}C_6$. It should also be noted that the amount of Ni_3Si was double the amount determined before this treatment.

5.1.4. Inductively Melted Samples

The microstructure of the inductively melted samples is presented in the SEM micrographs from Fig. 5.19 – 5.21.

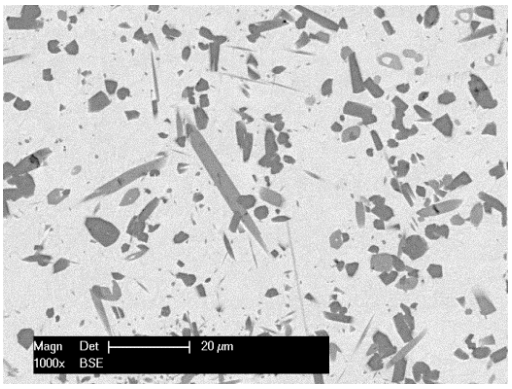

Figure 5.19: Structure of the inductively melted sample 15E

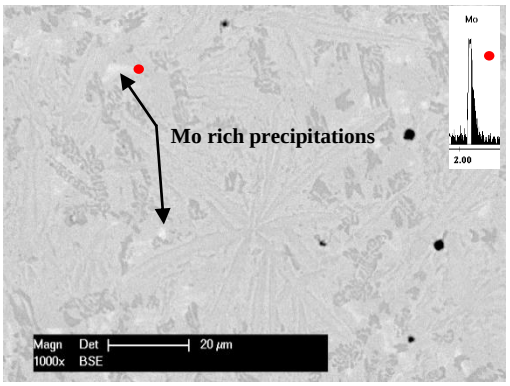

Figure 5.20: Structure of the inductively melted sample 18C

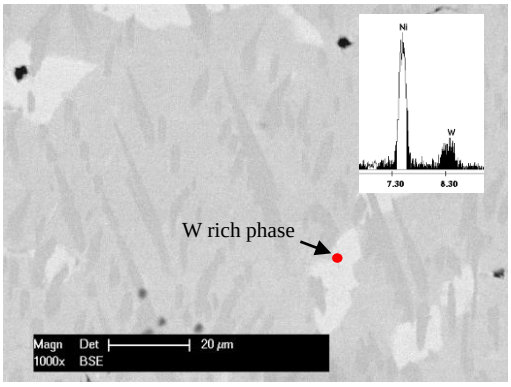

Figure 5.21: Structure of the inductively melted sample 19E

BUPT

Regarding the phase composition of the powders, the content of borides and carbides was almost unchanged after the inductive melting process of the feedstock powder 15E. However, a growth of the ceramic phases was observed. The amount of Ni_3Si was nearly twice the initial one, and additionally, 4 mass% Cr_3Si were formed.
Amazingly, all Si containing phases like $Co_{0.9}Si_{0.1}$, Ni_2Si, and $Cr_3Ni_5Si_2$ appeared after the inductive melting process of the feedstock powder 18C. Furthermore, the formation of a dendritic structure was identified and observed as well. The mapping investigations (see Fig. 5.22) revealed that the dendritic structure mainly consisted of Cr and Mo.

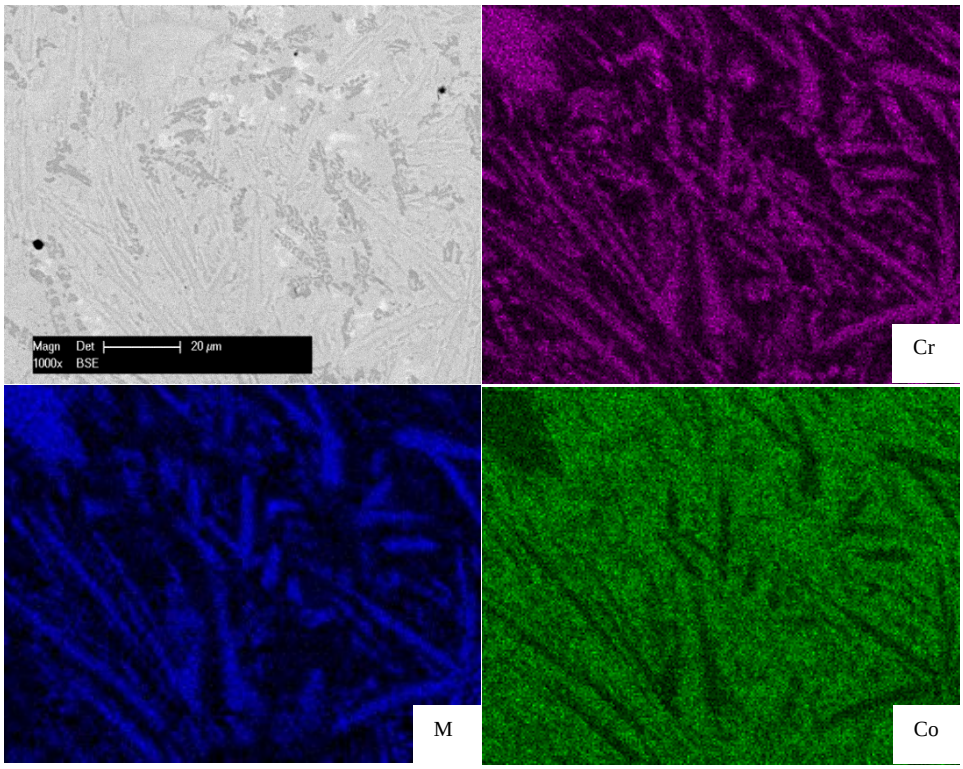

Figure 5.22: Star-shaped structure of the inductively melted sample 18C (mapping)

With respect to the binary phase diagram (see Fig. 5.23 [103]) of the system Cr/Mo, it is clear that up to 100 mass% Mo can be dissolved in Cr at a temperature of 1300°C, which was the measured temperature during the inductive melting process. However, it seems that the temperature was indeed much higher, probably over 1800°C (compare with Fig. 5.23). This statement can be made because of the formed dendritic structure. It is assumed that during cooling, from melting to solidification, there was a formation of a Cr/Mo dendritic structure. Due to the high liquidus point of this binary Cr/Mo phase in the alloy system, the dendritic structure could grow unhindered in the melt. Moreover, when cooled down, a partly precipitation of two single phases Cr- and Mo rich phases (marked in Fig 5.20) takes place at a temperature lower than 880°C. Due to this, no intermetallic Cr/Mo-phases were detected after the melting process. The adverse effect of such a dendritic

BUPT

structure on the formation of a dense oxide scale will be explained and clarified later in this work.

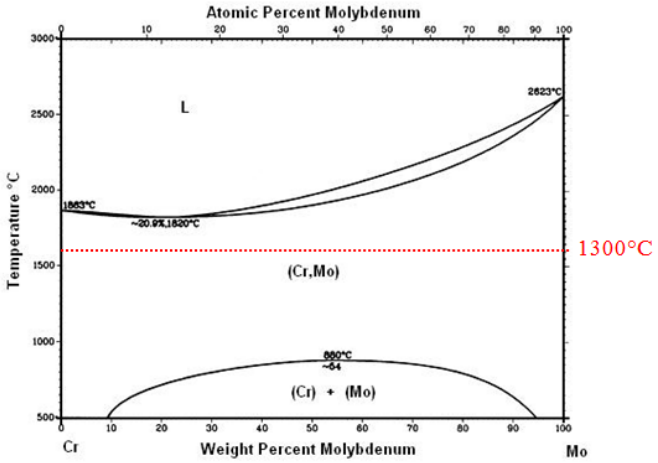

Figure 5.23: Binary phase diagram of the system Cr/Mo

Additionally, no carbides were detected for the inductively melted sample 18C, a fact confirmed by the EDX- and XRD- analyses.

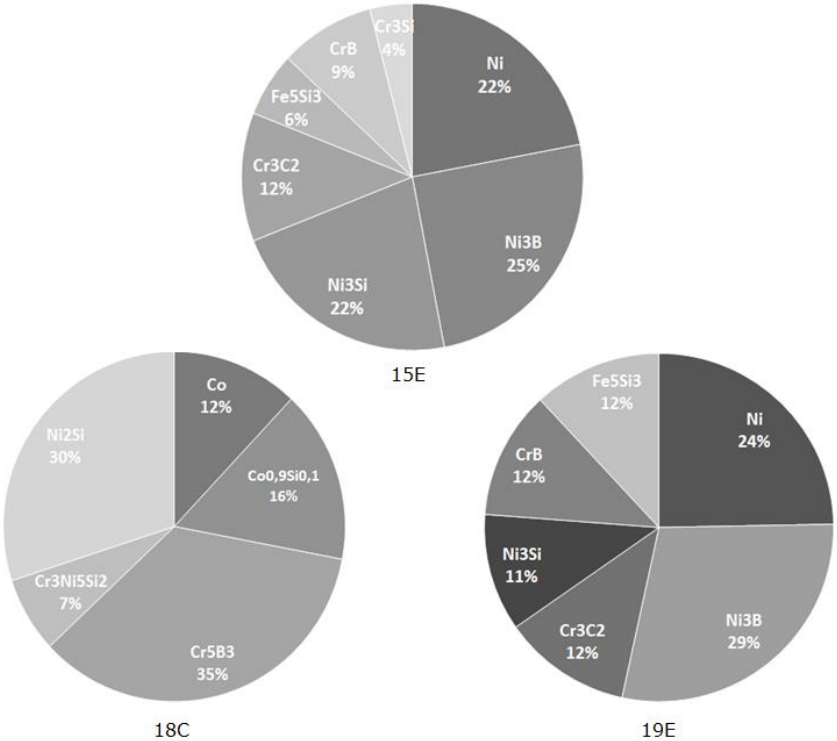

Figure 5.24: Quantification charts of the inductively melted nuggets

BUPT

However, this result is not surprising, because the material 18C used had only 0.2 mass% C. The amount of borides did not change after the inductive melting process of the feedstock powder 19E. However, there was a formation of W rich phases (marked in Fig. 5.21).
As stated before, there were some carbides in the self-fluxing feedstock powder 19E, which were detected with the aid of the EDX-analysis. These phases were finely agglomerated in the powder particles. This may have influenced the detection limit of the XRD-analysis and therefore it was not possible to detect the presence of such carbides in the powder particles. After the inductive melting process, 12 mass% Cr_3C_2 was detected (see Fig. 5.24).

5.1.5. Influence of the Melting Process on the Obtained Structure

A better evaluation of the obtained structures for each powder that was melted by means of the three different processes can be achieved through an overview presentation of the SEM micrographs, as shown in Fig. 5.25. In this way, it is possible both to compare the three powders melted by means of a certain process, and to compare the structure obtained for a certain chemical composition that was melted differently.

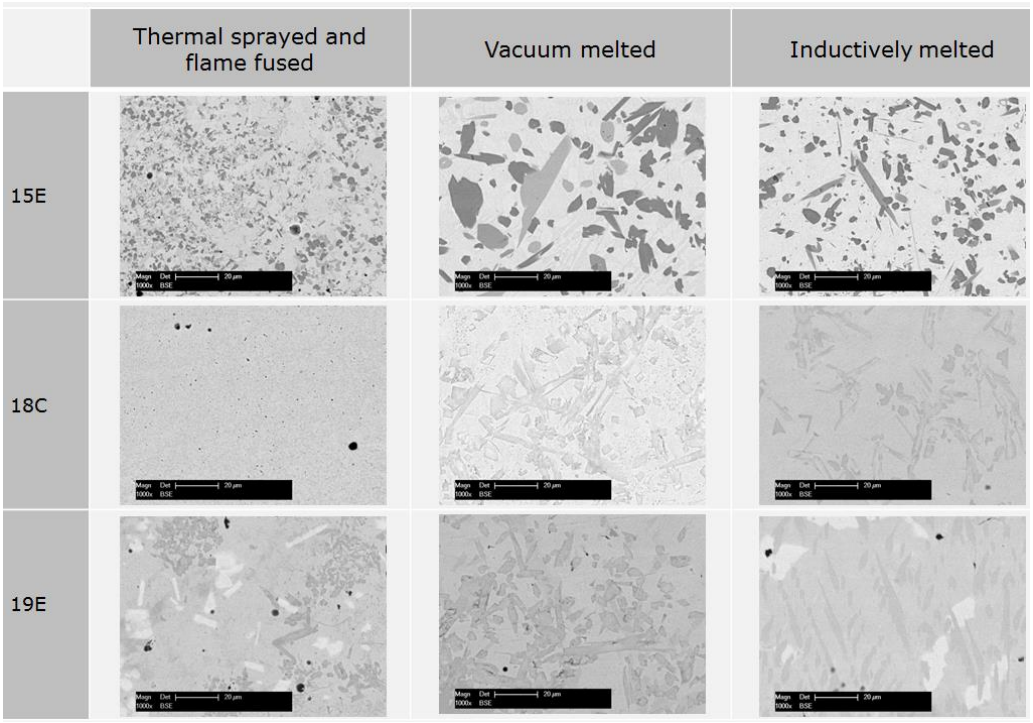

Figure 5.25: Overview of the obtained structures

It is obvious that the thermal sprayed and posterior remelted coating exhibited the finest microstructure from all the different melted samples made from the self-

BUPT

fluxing feedstock powder 15E. The melting process in the vacuum oven or with the inductor led to an enlargement of the phases. The reason for that was the operational load temperature during the inductive heating and the long exposure time in the vacuum oven, respectively. For the inductively melted samples, the high temperature and the focusing of energy on a small area, see chapter 4.1.3, were the important parameters which causes the growth of the phases. During the thermal spraying process, the powder particles remain a short time in the oxygen-acetylene flame at higher temperature and were not completely fused (compare Fig. 4.3 in chap. 4.1.1). The temperature generated by the oxyacetylene flame during the posterior remelting process was just above the inferior limit of the melting interval where the coating softens and becomes lucent. For that reason, there was only a barely visible change in the structure, with respect to the size of the phases, for the thermal sprayed and flame remelted sample 15E. A still smaller growth of the phases was identified for the thermal sprayed and flame remelted sample made from the Co based self-fluxing material 18C. It seems that the time and temperature was not sufficient to cause a growth of the phases. Only higher energy inputs during the melting process in the vacuum oven and with the inductor resulted in the formation of needle-like borides (vacuum) or a dendritic structure (inductive), which have a very negative effect on the strength of the samples. For the sample 19E, there was already a formation of boride clusters after the thermal spraying process. With respect to the softening point, this material had the lowest melting interval because of the high amount of degrading elements Si and B (see DTA-analysis in chapter 4.1.2). Due to this fact, the energy during the thermal spraying and posterior fusing process appears to have been high enough for the observable phase change. The carbides were rather finely dispersed in the sample, similar to the vacuum and inductively melted samples. In contrast, the borides had mainly a needle-like structure and were not agglomerated. The effect of the phase structure on the metal dusting resistance and the corrosion behaviour under such conditions is made clear in the following chapter.

BUPT

5.2. Morphology and Structure of the Exposed Samples

The samples were exposed in a gas mixture of nitrogen, carbon monoxide and hydrogen in a ratio of 80:10:10 at 650°C for 513 hours (test 1) or for 1019 hours (test 2), respectively, in the high temperature corrosion test rig. One side of the tested samples was ground with 4000 SiC-grit paper and cleaned with ethanol before the exposure to the metal dusting atmosphere. Following this, they were positioned in a ceramic boat with the ground surface on top. The exposed samples were evaluated by means of light microscopy (LM), scanning electron microscopy (SEM) combined with energy dispersive X-ray analysis (EDX), and by X-ray diffraction (XRD).

5.2.1. Samples after 500 Hours of Exposure to Metal Dusting Conditions

During the exposure of the samples to the carburizing atmosphere, many easily-adhering graphite particles or layers were formed on the surface. The extent of the graphite formation is given in the following figure. Due to this reason, the graphite had to be removed with a paintbrush for further investigation of the samples.

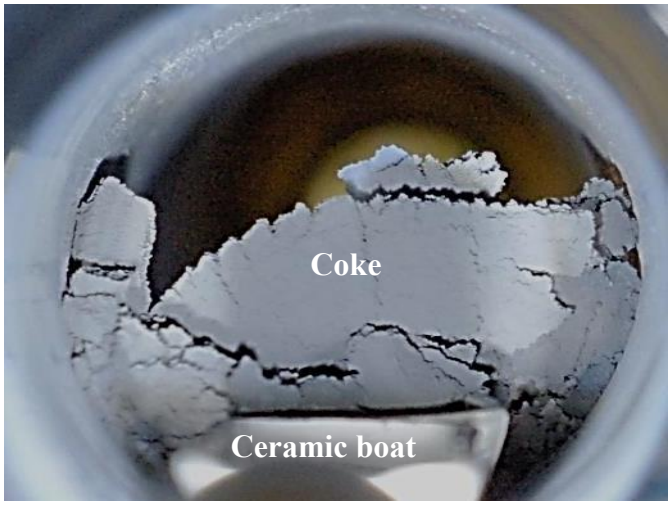

Figure 5.26: View in the glass reactor of the HT test rig after the exposure of the samples to metal dusting conditions

The examinations of the samples with the light microscope at a magnification of 30x revealed that especially the inductively melted 19E sample was visibly carburized and partially corroded with pitting along the edge areas (see point A in Fig. 5.27).

BUPT

The tendency for damage along the edges and the cause thereof was already described in chapter 2.7.

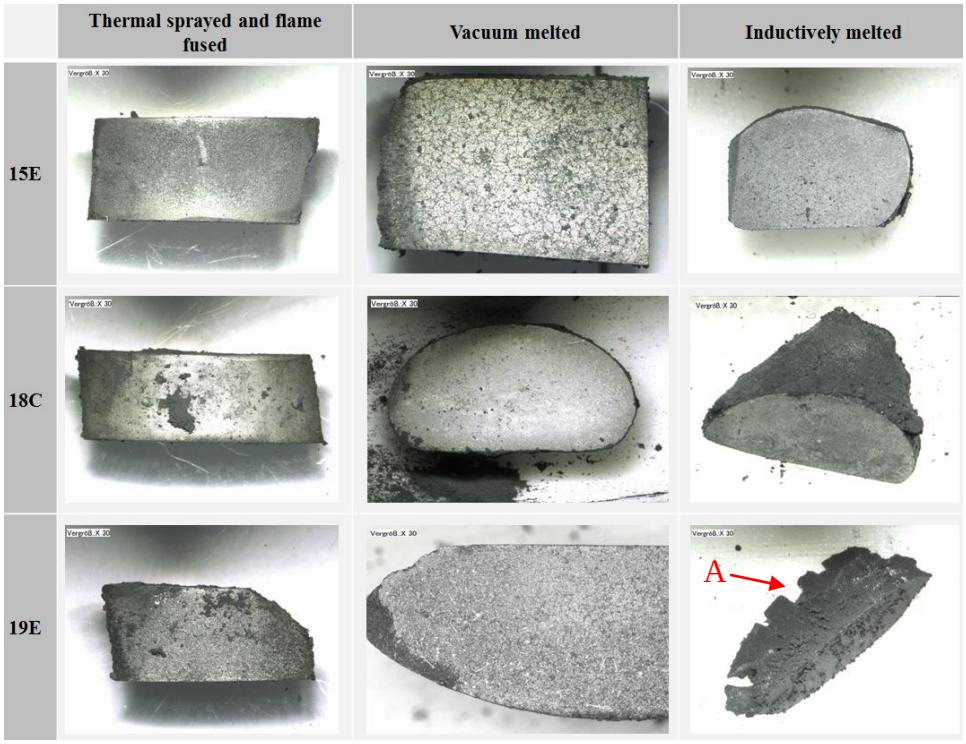

Figure 5.27: Overview of the macroscopic examinations of the samples after 500 hours of exposure to metal dusting conditions

Scanning electron microscope observations of all samples at a higher magnification in cross section revealed that most of them were affected to some extent.

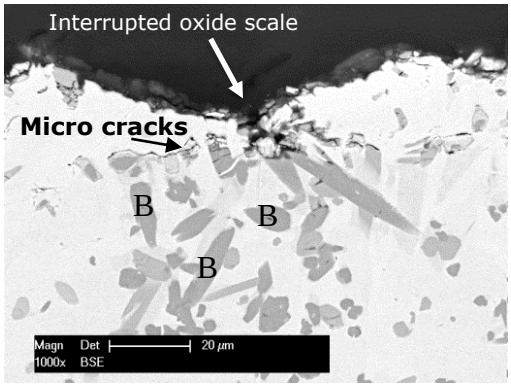

Figure 5.28: Cross section of the vacuum melted sample 15E after 500 hours exposure to metal dusting conditions

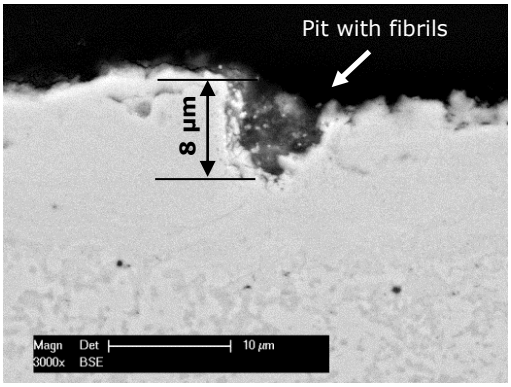

Figure 5.29: Cross section of the flame fused sample 18C after 500 hours exposure to metal dusting conditions

BUPT

The samples were either destroyed through internal oxidation, which led to the development of micro cracks (Fig. 5.28), or attacked through small pits with a diameter and a depth of 8 µm, which were filled with fibrils (see Fig. 5.29).

The kinetics of growth of such fibrils on the surface of non-protected metallic materials (without an oxide scale) can be demonstrated using a simple example. The following figure shows an iron nail after 500 hours of exposure to the same metal dusting conditions. The nail was positioned on the ground of the ceramic boat before the exposure, and was raised up only by the force of the fibrils grown on it.

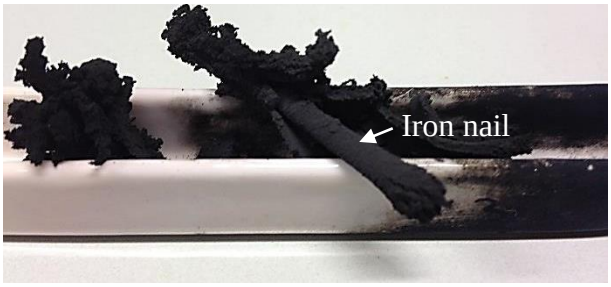

Figure 5.30: Iron nail after 500 hours of exposure to metal dusting conditions

There are at least two hypotheses regarding the fact that not all of the samples were able to form a dense protective oxide scale.
One of the reasons might be that the outward diffusion of the oxide scale forming elements would be reduced or even blocked in samples with coarser phase components, such as those which contain mostly borides and carbides.
Another reason for the growth of a non-protective oxide scale might be the formation of spinels. Such spinels were observed and identified with the EDX-analysis. Besides the instability of such spinels, due to their defects [26], their formation can lead to a significant volume expansion, which disrupts the material and results in surface damage, as described in [104]. An example of an spinel containing scale, analyzed by EDX, is given in the following figures.

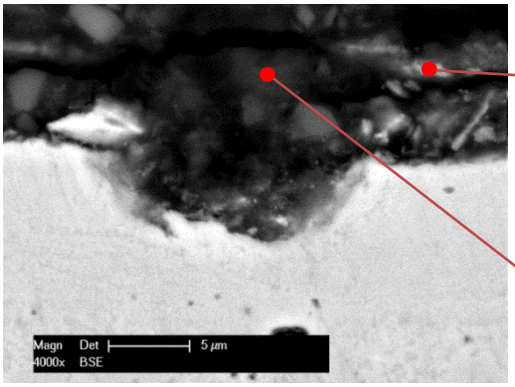

Figure 5.31: Cross section of the flame fused 18C sample after 500 hours exposure to metal dusting conditions

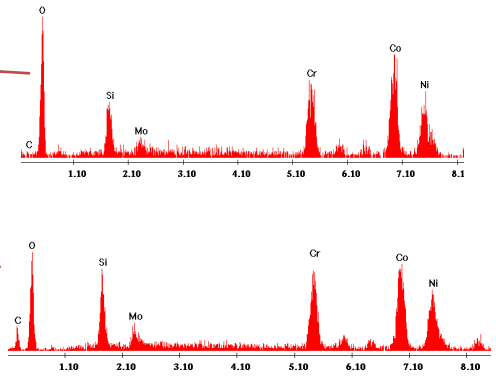

Figure 5.32: EDX-analysis of the oxide scale formed on the flame fused 18C sample after 500 hours exposure to metal dusting conditions

BUPT

The highest resistance was shown by the thermal sprayed and flame fused sample, made from the feedstock powder 15E, which formed an almost completely dense protective oxide scale on its surface (see Fig. 5.33). The fine phase distribution observed in the sample´s microstructure appears to provide a considerable contribution to the continous growth of the oxide scale. The oxide scale reached a maximum thickness of approximately 5 µm, the average thickness was 1.5 µm. The EDX analyses in the points 1 and 2 (Fig. 5.34) revealed that the protective oxide scale of the thermal sprayed and flame fused sample mainly consisted of Cr/Si-oxides.

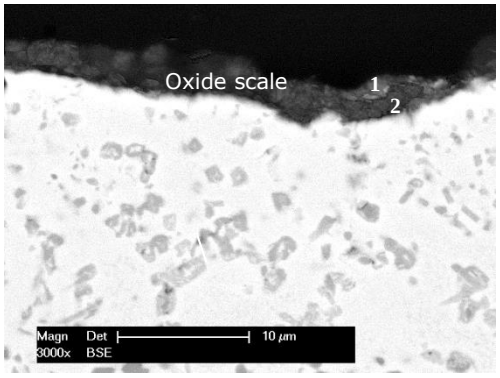

Figure 5.33: Cross section SEM micrograph of the flame fused 15E sample after 500 hours exposure to metal dusting conditions

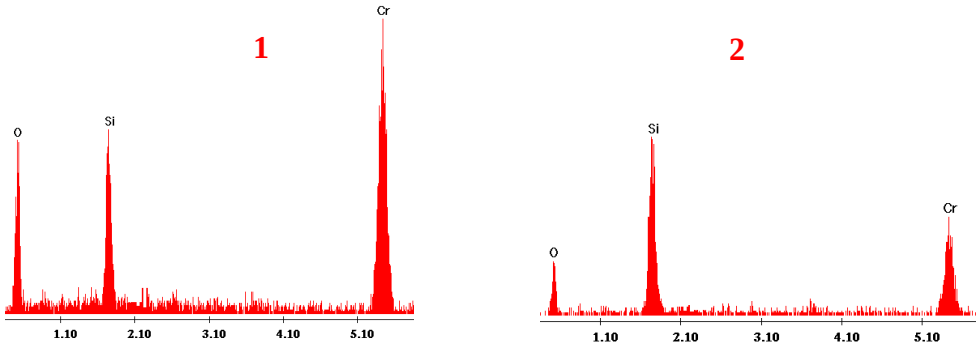

Figure 5.34: EDX analyses 1 and 2 of the oxide scale grown on of the flame fused 15E sample after 500 hours exposure to metal dusting conditions

5.2.2. Samples after 1000 Hours of Exposure to Metal Dusting Conditions

An overview of the macroscopic investigations of the samples after 1000 hours of exposure to metal dusting conditions is presented in Fig. 5.35 (after removing of the graphite with a paintbrush). Even at a magnification of 30x, it is obvious, that the

BUPT

samples 18C and 19E were especially attacked along the edges (red marked in Fig. 5.35) after the inductive melting process.

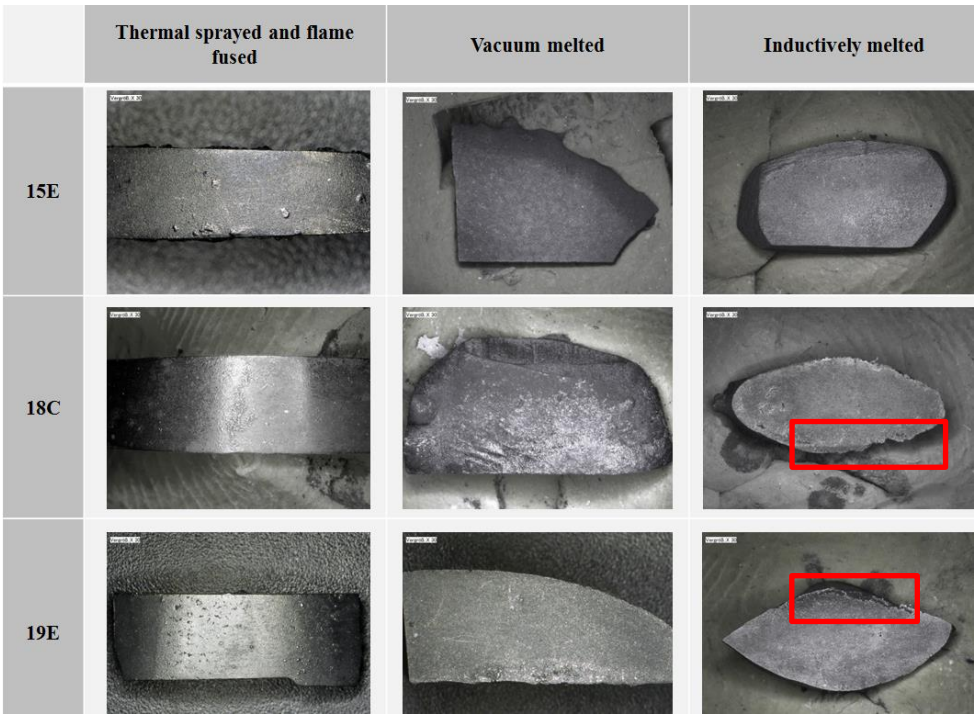

Figure 5.35: Overview of the macroscopic examinations of the samples after 1000 hours of exposure to metal dusting conditions

Comparing the results after 500 hours of exposure with the results obtained after 1000 hours of exposure to metal dusting atmosphere, one can clearly note that extending the duration of exposure led to a more intensive carburization. For example, the pits observed for the thermal sprayed and flame fused sample 18C, exposed for 1000 hours (see Fig. 5.36), exhibited a larger diameter (about three times larger) in comparison with those observed for the same alloy that was exposed only for 500 hours.

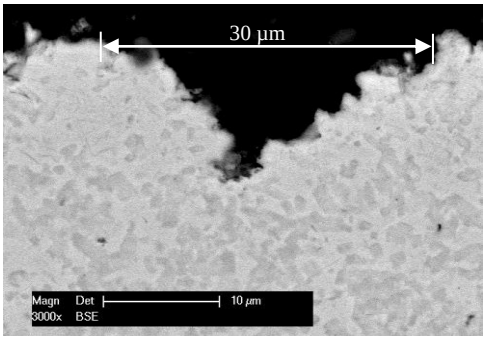

Figure 5.36: Cross section of the sample 18C, thermal sprayed and remelted with flame after 1000 hours under MD conditions

BUPT

Much more affected were the samples with a coarse microstructure (see Fig. 5.37 and 5.38). The material was much more destroyed through pits with different geometries and sizes, up to a depth of 50 µm.

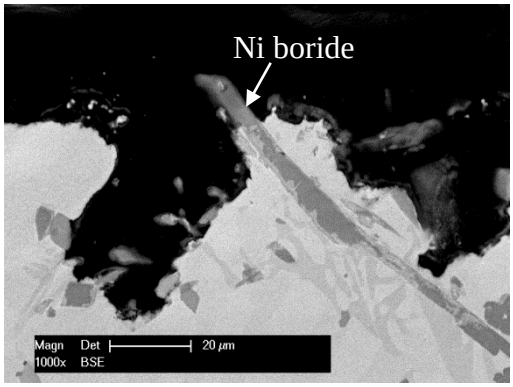

Figure 5.37: Cross section SEM micrograph of the vacuum melted sample 15E after 1000 hours exposure to MD conditions

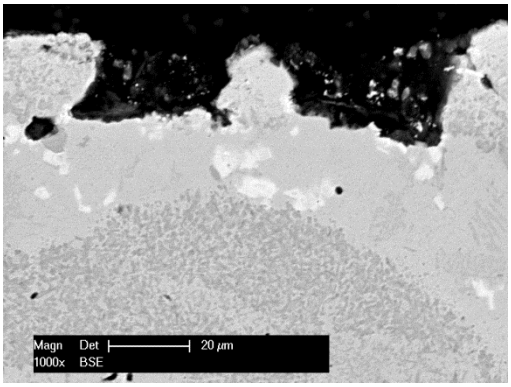

Figure 5.38: Cross section SEM micrograph of the flame fused sample 19E after 1000 h of exposure to MD conditions

It can be concluded that the surface morphology of the melted samples is probably another important factor that influences the severity of the metal dusting attack. The surface of the 18C nugget melted inductively revealed a star-shaped structure (see Fig. 5.39), which probably consists of unstable spinels, e.g. of type Cr_2MoO_4 (compare with Fig. 5.22). Such a star shaped morphology was only found on the surface of the inductively melted sample 18C, which was exposed for 1000 hours under metal dusting conditions. It was supposed that the star-shaped formation of oxides led to a wave-like appearance of metal dusting attacks (see Fig. 5.40). It could not be conclusively clarified that the star-shaped formation of oxides is linked to the dendritic structure.

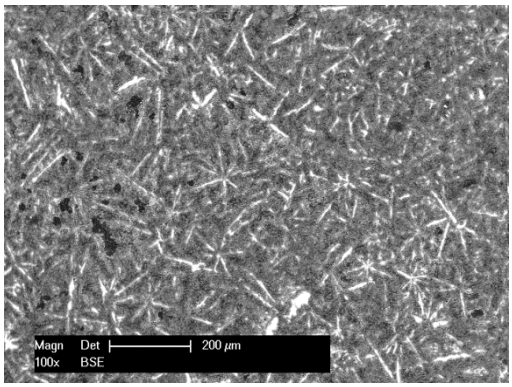

Figure 5.39: SEM micrograph of the star-shaped structure of the sample 18C, melted with an inductor

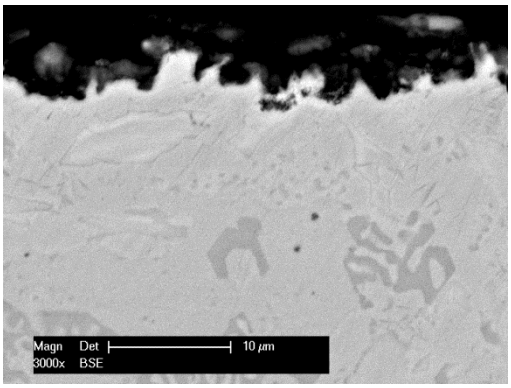

Figure 5.40: Cross section SEM micrograph of the inductively melted sample 18C after 1000 hours of exposure to metal dusting conditions

BUPT

Considering the oxide scale characteristics and the degree of pitting attack, the best results were again achieved with the flame fused 15E samples. The oxide scale grew further from a maximum thickness of 5 µm after 500 hours up to approximately 8 µm after 1000 hours in some areas (see Fig. 5.41). The average thickness of the Cr/Si oxide scale was 2 µm (see Fig. 5.42) and thus 0.5 µm thicker than that of the 15E sample after 500 hours. This observation can be simply explained due to the fact that once the oxide scale is already formed through prolonging the time of exposure, the sample would consequently follow the parabolic oxidation law (see chapter 2). Some oxide forming elements will not be able to contribute anymore to further oxide formation because the value for the oxygen partial pressure necessary for the respective oxide formation is too low.

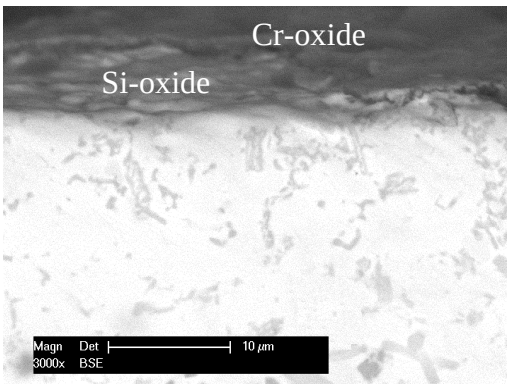

Figure 5.41: Cross section SEM micrograph of the flame fused sample 15E after 1000 hours of exposure to metal dusting conditions

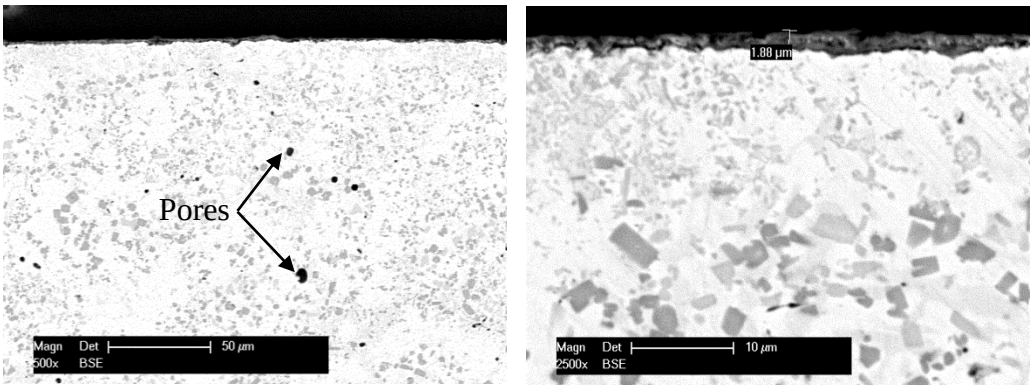

Figure 5.42: Cross section SEM micrograph of the flame fused sample 15E after 1000 hours of exposure to metal dusting conditions, observed at a magnification of 500x (left) and 2500x (right)

The oxide scale grown on the thermal sprayed and flame remelted 15E sample consisted of Cr- and Si-oxides (confirmed with the EDX-analysis). It is known that

BUPT

both oxides are formed at the beginning if the oxygen partial pressure is high enough (pO_2= min. 10^{-32}, see Ellingham-Richardson-diagram in chapter 2). After the epitaxial growth of the oxide scale, the oxygen partial pressure decreases at the interface between this scale and the alloy material. Due to this reason, only Si oxides are formed at this interface, because Si is still able to oxidize even at lower values for oxygen partial pressure, compared to Cr, which will not oxidize any more. As stated in chapter 2, when an ideal Cr-rich protective oxide scale can no longer be formed on the material surface, its microstructure becomes carburized. It seemed that especially the Si containing phases were responsible for the continuous formation of a dense, adherent, and almost defect free oxide scale on the whole surface of the thermal sprayed and flame fused sample, obtained from the feedstock powder 15E.

Through XRD-analysis for the thermal sprayed and flame fused sample 15E, compared with all other samples, it was established that this sample had the second highest amount of silicides (35 mass%), with the sample with the highest silicides content being the flame fused 18C (53 mass%). Nevertheless, out of the detected silicide phases, the flame fused sample 15E contained a high amount of Cr_3Si (20 mass%). Moreover, with respect to the Cr-Si phase diagram (see Fig. 5.43 [103]) it can be asserted that the amount of Si in the Cr_3Si-phase is between 13.6 – 16.2 mass% (framed).

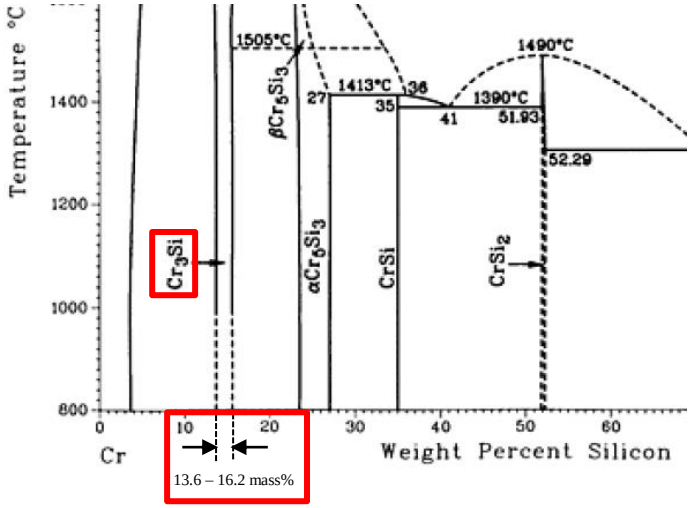

Figure 5.43: Section of a Cr-Si phase diagram

For the observation and analysis of the Si containing phases, a special colour etching method, described in chapter 3, was applied in order to assess the correlation between the formation of a dense, continuously formed oxide scale and the distribution of the Si containing phases before the exposure of the samples under metal dusting conditions. For that, the colored phases were first marked by means of hardness indentation (see the example in Fig. 5.44). With the help of the

BUPT

SEM combined with EDX analysis 1 and 2, the brown phases were identified as Si containing phases, whereas the EDX measurement no. 3 in the light grey matrix reflected no signal for Si (see Fig. 5.47).

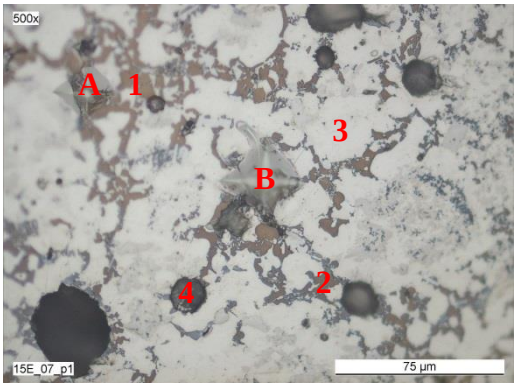

Figure 5.44: LM micrograph of a color etched sample with the hardness indentation A and B on it

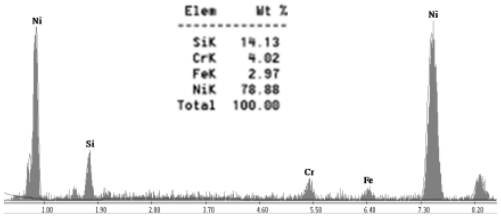

Figure 5.45: EDX-analysis 1 of the brown, color etched phases

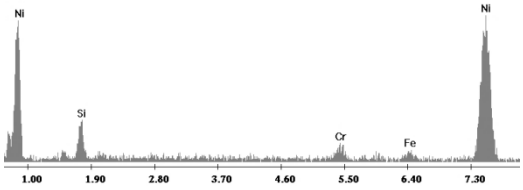

Figure 5.46: EDX-analysis 2 of the brown, color etched phases

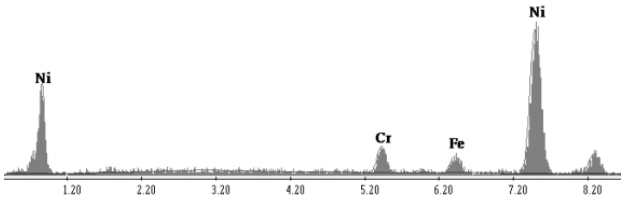

Figure 5.47: EDX-analysis 3 of the light grey matrix

BUPT

The EDX analysis no. 4 of the dark grey round shaped inclusion revealed the existence of oxides (see Fig. 5.48).

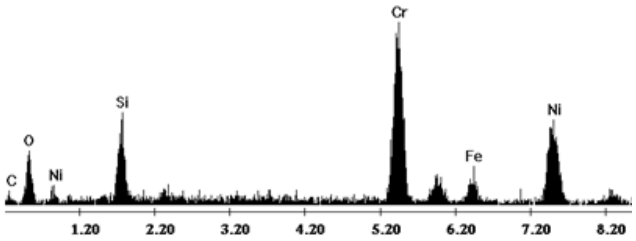

Figure 5.48: EDX-analysis 4 of the dark grey round shaped particles

Through the definite results of the color-etching test, the distribution of the Si containing phases can be compared and confirmed reliably with respect to the applied melting process and the chemical composition of all exposed samples. The investigations of the flame fused sample 15E revealed that this sample had a higher resistance to metal dusting atmosphere than the other tested samples. This behaviour is mainly attributed to the finely and homogenously distributed Si containing phases (see Fig. 5.49). In contrast to this, the melting process in the vacuum oven led to the growth of relatively coarse phases (see Fig. 5.50). As stated above, these two factors are detrimental for the formation of a dense and stable oxide scale. The structure of the Si containing phases of the samples, which were inductively melted, had a fine structure, but they were mostly agglomerated and not well dispersed.

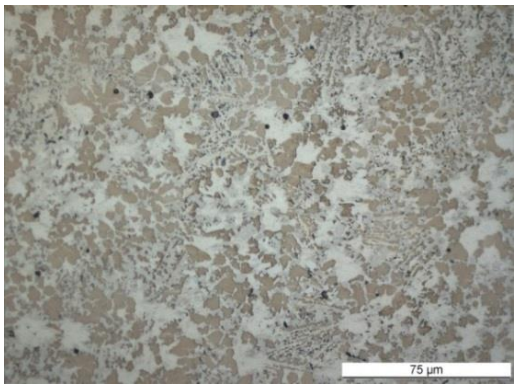

Figure 5.49: LM micrograph of the color etched flame fused sample 15E

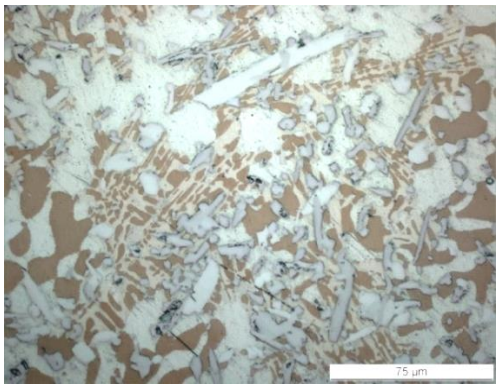

Figure 5.50: LM micrograph of the color etched vacuum oven melted sample 15E

As mentioned before, the dendritic structure, exhibited in the inductively melted sample 18C, also had an adverse effect on the resistance to metal dusting. In figure 5.51, it can be seen that the Si rich phases are distributed especially along the grain boundaries of the dendrites phases. It is assumed that during the exposure to metal

BUPT

dusting conditions the formation of the oxide scale of this sample takes place only locally.

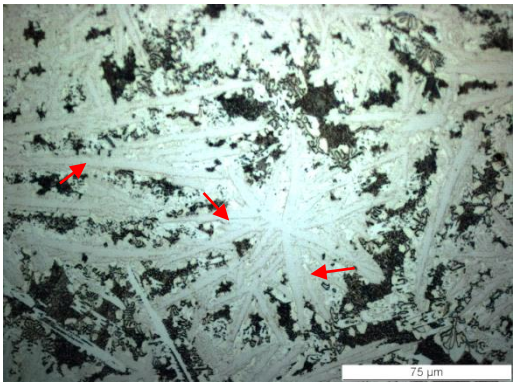

Figure 5.51: LM micrograph of the inductively melted color etched sample 18C

Comparing the color etching results with the behaviour of the samples under extreme carburizing conditions, it can be concluded that there is a direct correlation between the structure, especially the characteristics of the Si containing phases, and the metal dusting resistance. The flame fused sample 15E exhibited a better metal dusting resistance in comparison with the other materials investigated in this experimental work. It seemed that the finely dispersed Cr_3Si-phase was mainly responsible for the formation of a dense oxide scale underneath the initially grown Cr/Si oxide scale. Such oxidation behaviour even under strong carburizing conditions offers a better protection of the exposed alloy, and in addition, prevents the metal dusting attack for a longer exposure time.

BUPT

6. CONCLUSIONS AND OUTLOOK

6.1. Conclusions

The purpose of this work was the evaluation of different melted self-fluxing alloys considering their suitability under metal dusting conditions. Three alloys with a content of 3-4 mass% B and Si, respectively, and a Cr content of 16 to 18 mass% were studied: two alloys are Ni based (15E and 19E), the last one with W, Mo and Cu addition, and one is Co based (18C) also with Mo addition.

For the exposure of the self-fluxing alloys under (real) metal dusting conditions there was necessary to manufacture melted samples. Therefore available or accessible methods - also applied in the industry - were used. These included the thermal spray process and subsequent flame fusing as well as the complete melting of powders into nuggets in a vacuum furnace or with the aid of an inductor.

It was clearly pointed out that the achieved degree of compactness is very important for the direct comparison of all samples. Due to that reason, the value determined for the degree of internal porosity (of around 0.5%) for the thermal sprayed and flame fused samples was the benchmark for all other samples.

Furthermore, for the manufacturing of the nuggets in the vacuum oven, there was necessary to establish a certain melting interval, which was determined with the help of the differential thermal analysis (DTA). After the definition of the process temperature for each feedstock powder, the treatment time was optimized in order to guarantee a low porosity. About 120 minutes were necessary for the purpose to reach the reference value for all feedstock powders which were subjected to a temperature, which was about 50°C above the determined melting interval from the DTA-tests.

The inductive melting process was more difficult to perform because there were no accessible parameters (time and current) in the literature for the treatment of such self-fluxing powders in a graphite crucible. Therefore these parameters were empirically determined.

The coating and nugget microstructure after the melting processes was mainly characterized by means of scanning electron microscopy (SEM). The thermal sprayed and flame fused coatings obtained from the feedstock powders 15E or 18C provide the finest and most uniform microstructure. In contrast, the microstructure of the coating made of the feedstock powder 19E, was very coarse and inhomogeneous. A cluster of Ni- and Cr-borides as well as Cr- and W-precipitates were formed in the case of this sample.

It could be confirmed that the vacuum as well as the inductive melting of all feedstock powders led to a coarse microstructure. One of the crucial factors was the time, especially for the nuggets, which were manufactured in the vacuum oven. With respect to the inductive melting processes, there was another essential factor, namely the temperature. In comparison with the both afore-mentioned processes,

BUPT

the temperature during the inductive heating was probably up to 800°C higher. This explains the formation of a coarse microstructure, although the exposure time was just about 1-3 seconds.

One of the most important challenges of this PhD thesis was the reconstruction of the high temperature corrosion test rig for the subsequent exposure of the samples under metal dusting conditions. After the compilation of the test rig, the melted samples were exposed in a equimolar gas mixture consisting of carbon monoxide and hydrogen at 650°C for 513 hours (test 1) respectively 1019 hours (test 2).

The scanning electron microscopical investigations of the samples in cross section showed, that most of them were attacked more or less already after 500 hours. The samples showed either internal oxidation, which led to micro cracks evolution, or pitting attack with a diameter and a pit depth of 8 µm filled with fibrils. For all samples which could not form a dense protective oxide scale, it was assumed, that the continuous delivery of the oxide scale forming elements from inside out was blocked due to the presence of coarser phase components, mostly borides and carbides. Another reason for an incomplete protective oxide scale was the existence of unstable spinels.

The highest resistance to metal dusting showed the thermal sprayed and flame fused sample, made of the feedstock powder 15E, which formed an almost dense protective oxide scale on its surface. Especially the fine microstructure in combination with the chemical composition of this sample made possible the formation of a continuous oxide scale with an average thickness of 1.5 µm. The EDX analysis revealed that the protective oxide scale on these samples consists of Cr- and Si-oxides.

The observation of the samples after 1000 hours of exposure to metal dusting exhibited a similar effect like in the case of 500 h of exposure but clearly more intense. Especially the samples with a coarse microstructure were more or less attacked through pitting up to a depth of 50 µm. The supposed positive effect of the elements Mo and Cu was not demonstrated for the samples made out of the feedstock powders 18C and 19E. It is known that the phenomenon of a pitting attack occurs preferentially at the edges and corners. Therefore, Cu and Mo are often added in order to enhance the edge stability of self-fluxing alloys under metal dusting conditions. But such an improvement was not noticed. It seemed that the addition of these elements had even a negative effect, because of the very complex microstructure and the formed precipitates. Moreover, Mo in the self-fluxing alloy 18C, melted with the inductor, even resulted in the formation of spinels, as mentioned before. Their formation led to a significant volume expansion, which disrupted the material and resulted also in surface damages, described in chapter 5.

The best results were achieved again for the thermal sprayed and flame fused 15E samples. The oxide scale was almost completely dense and reached an average thickness of approximately 2 µm after 1000 hours (1.5 µm after 500 hours). No pits were observed on the sample surface. The grown oxide scale consisted of Cr- and Si oxides (confirmed with the EDX-analysis).

With the help of a special developed color etching process it was possible to confirm that there was a correlation between the formation of a dense, continuously formed oxide scale, therefore an acceptable metal dusting resistance, and the distribution of

BUPT

the Si containing phases. The light microscopy of the samples in cross section at a magnitude of 500x revealed that the silicides were very uniform distributed in the matrix. Furthermore, the XRD-analysis of this sample led to the assessment that it was the one with the highest amount of Cr_3Si (20 mass%).

Based on all investigations implemented in this work, it can be concluded that the thermal sprayed and flame fused 15E sample exhibited the best metal dusting resistance in comparison with the rest of the tested self-fluxing materials. The combination of a Ni based matrix, a very fine microstructure and the right amount of the proper oxide scale forming elements makes this material suitable for the exposure under metal dusting conditions.

6.2. Outlook

The present work dealt with the morphological study of three differently melted self-fluxing materials considering their suitability under metal dusting conditions. It was possible to obtain fundamental knowledge about the behaviour of such materials with different chemical compositions. The focus was on the phase structure, especially on the Si containing phases and their influence on the metal dusting resistance. It was confirmed that a thermal sprayed and flame fused coating is able to protect the component (made of steel) against metal dusting attack up to 1000 hours.

Based on the results of this experimental work some further research directions might be outlined as follows:

- Investigation of the metal dusting behaviour of pre-oxidized self-fluxing alloys
- Coating of components for the exposure under real metal dusting conditions in a field test
- Investigation of the required coating thickness of the self-fluxing material
- Melting and exposure of further self-fluxing materials, e.g. with Al in the chemical composition
- Investigation of laser-cladded self-fluxing materials exposed to metal dusting

BUPT

References

1. H. VENVIK. "Metal dusting corrosion initiation in conversion of natural gas to synthesis gas," Gas Technology Conference presentation, (2011).
2. J. ALVAREZ et al. "Protective coatings against metal dusting," Surface and Coatings Technology, Vol. 5-7, 422–426 (2008).
3. E. PIPPEL et al. "Micromechanisms of metal dusting on Fe-base and Ni-base alloys," Materials and Corrosion, Vol. 49, 309–316 (1998).
4. L. GIL and M. RODRIQUEZ. "Wear resistance of post heat treated HVOF coatings based on cermet - nickel based alloys mixture," 9th Latin American and Caribbean Conference for Engineering and Technology proceedings, 12, (2007).
5. N. Y. SARI and M. YILMAZ. "Improvement of wear resistance of wire drawing rolls with Cr–Ni–B–Si+WC thermal spraying powders," Surface and Coatings Technology, Vol. 13, 3136–3141 (2008).
6. P. HEIMGARTNER et al. "New fused coatings for combined wear and corrosion resistance," EUROMAT 97 proceedings, 109–113 (1997).
7. Y. L. CHENG et al. "The preparation and properties of iron base self-fluxing alloy spray-welding coatings with different rare earths and chromium content," JOURNAL OF MATERIALS SCIENCE, Vol. 37, 4589–4595 (2002).
8. Z. IŽDINSKÁ et al. "The structure and mechanical properties of NiCrBSi coatings prepared by laser beam cladding," Materials Engineering, Vol. 17, 2010, No. 1 (2010).
9. V. I. POKHMURS'KYI and O. S. KALAKHAN. "Plasma coatings and their ability to protect titanium alloys against corrosion fretting-fatigue fracture," Materials Science Vol. 33, No.3 (1997).
10. G. G. PAJONK and H.-D. STEFFENS. "Corrosion behaviour of coated materials," Fresenius J Anal Chem, Vol. 358, 285–290 (1997).
11. I. A. PODCHERNYAEVA et al. "Protective Coatings on Heat-Resistant Nickel Alloys (Review)," Powder Metallurgy and Metal Ceramics Vol. 39, Nos. 9-10, 434–444 (2000).
12. L. BELL. "The Chemistry of the Blast-furnace," Journal of the Chemical Society, Vol. 22, 203–254 (1869).
13. J. PATTINSON. "On Carbon and Other Deposits from the Gases of Blast Furnaces in Cleveland," 85-100 (1876).
14. A. AL-MESHARI. "Metal Dusting of Heat-Resistant Alloys," Doctoral Thesis, 344 p., University of Cambridge (2008).
15. P. SZAKALOS et al. "Patent WO2003072836A1 - Copper based alloy resistant against metal dusting and its use," (current as of May. 14, 2014).
16. P. SZAKÁLOS. "MECHANISMS OF METAL DUSTING," Doctoral Thesis, (2004).
17. E. CAMP. "Corrosion of 18-8 alloy furnace tubes in high temperature vapour phase cracking service," Corrosion, Vol. 1, 149–160 (1945).
18. C. R. BRANAN. "Rules of Thumb for Chemical Engineers," Handbook, Fifth Edition, ISBN-10: 0123877857 (2012).
19. G. HAN et al. "Metal dusting and coking of alloy 803," Corrosion Science, Vol. 2, 443–452 (2004).

20. C.-H. CHANG and W.-T. TSAI. "Metal dusting behavior of 321 stainless steel: Effects of edge and corner," Met. Mater. Int. (Metals and Materials International), Vol. 2, 267–273 (2011).
21. D. J. YOUNG and J. ZHANG. "Metal Dusting: Catastrophic Corrosion by Carbon," JOM, Vol. 64, No.12, 1461–1469 (2012).
22. J. ZHANG et al. "Metal Dusting of Alumina-Forming Creep-Resistant Austenitic Stainless Steels," Oxid Met (Oxidation of Metals), Vol. 3-4, No.77, 167–187 (2012).
23. C. M. CHUN and T. A. RAMANARAYANAN. "Metal-Dusting Corrosion of Low-Chromium Steels," Oxidation of Metals, Vol. 62, Nos. 1/2, p 71-92 (2004).
24. J. C. NAVA PAZ and H. J. GRABKE. "Metal dusting," Oxidation of Metals, Vol. 39, Nos. 5/6, p 437-456 (1992).
25. Y. NISHIYAMA et al. "Metal dusting behaviour of Cr–Ni steels and Ni-base alloys in a simulated syngas mixture," Corrosion Science, Vol. 8, No. 48, p 2064–2083 (2006).
26. H. J. GRABKE. "Metal dusting," Materials and Corrosion, Vol. 10, No. 54, p 736-746 (2003).
27. A. AGÜERO et al. "Metal Dusting Protective Coatings. A Literature Review," Oxid Met (Oxidation of Metals), Vol. 1-2, No. 76, p 23-42 (2011).
28. H. J. GRABKE et al. "Metal dusting resistance of high chromium alloys," Materials and Corrosion, No. 11, 54, 860 (2003).
29. K. VOISEY et al. "Inhibition of metal dusting of Alloy 800H by laser surface melting," Applied Surface Science, 252, 3658–3666 (2006).
30. R.F. HOCHMAN (ED.), Proceedings of the 5th Metallic Corrosion Conference (1972).
31. R.F. HOCHMAN (ED.), Proceedings of the Electrochemical Society, Vol. 77, p.715 (1976).
32. W. BRANDL et al. "Prevention of metal dusting on Ni-based alloys by MCrAlY coatings," Corrosion Science, 49, p 3765–3771, 10 (2007).
33. "HUAYING YIN et al. "Effect of gas composition on coking and metal dusting of 2.25Cr–1Mo steel compared with iron," Corrosion Science 51, p 2983-2993 (2009).
34. B. A. BAKER. "Alloy Solutions to Metal Dusting Problems in the Chemical Processing Industry," (2002).
35. H. J. GRABKE. "Mechanisms and Prevention of Corrosion in Carbonaceous Gases," MSF (Materials Science Forum), 369-372, p 101–108 (2001).
36. H. J. GRABKE. "Carburization, carbide formation, metal dusting, coking," MTAEC 9, 36(6)297 (2002).
37. H. J. GRABKE and M.-L. E. M. KRAJAK. "Metal dusting of high temperature alloys," Werkstoffe und Korrosion 44, p 89-97 (1993).
38. H. J. GRABKE et al. "Role of sulphur in carburization, carbide formation and metal dusting of iron," Surf. Interface Anal. (Surface and Interface Analysis) 34, 1, 369 (2002).
39. H. J. GRABKE and E. M. MÜLLER-LORENZ. "Protection of high alloy steels against metal dusting by oxide scales," Materials and Corrosion 49, p 317-320 (1998).
40. R. BÜRGEL, Handbuch Hochtemperatur-Werkstofftechnik: Grundlagen, Werkstoffbeanspruchungen, Hochtemperaturlegierungen und -beschichtungen, handbook, ISBN 9783528231071, Vieweg, Wiesbaden (2006).
41. B. A. BAKER. "Metal dusting in a laboratory environment – alloying addition effects," Superalloys, p 41-50 (2008).

BUPT

42. C. M. CHUN et al. "Mechanisms of metal dusting corrosion of iron," Journal of The Electrochemical Society, 149 (7), p 348-355 (2002).
43. F. DI GABRIELE et al. "Metal dusting performance of nickel-base alloys," Materials Science Forum, 461-464, p 545-552 (2004).
44. C. GEERS. "AIF 15237N Abschlussbericht," (current as of Apr. 15, 2014).
45. H. J. GRABKE. "Mechanisms of Metal Dusting of Low and High Alloy Steels," SSP (Solid State Phenomena), Vol. 41, p 3-16 (1995).
46. C. M. CHUN et al. "Metal dusting corrosion of cobalt," Journal of The Electrochemical Society, 150 (2), p 76-82 (2003).
47. J. ZHANG and D. J. YOUNG. "Coking and Dusting of Fe–Ni Alloys in CO–H_2–H_2O Gas Mixtures," Oxid Met (Oxidation of Metals), 70, p 189-211 (2008).
48. K. VOISEY et al. "The Use of Plasma Sprayed Laser Remelted Corrosion Resistant Metallic Coatings to Inhibit Metal Dusting," MSF (Materials Science Forum) Vols. 461-464, p 553-560 (2004).
49. K. RÖHRIG. "Guss aus hochkorrosionsbeständigen Nickel-Basislegierungen," www.kug.bdguss.de (current as of Jul. 04, 2014).
50. J. WALMSLEY et al. "The evolution and oxidation of carbides in an Alloy 601 exposed to long term high temperature corrosion conditions," Corrosion Science 52, Vol. 12, p 4001-4010 (2010).
51. SPECIAL METALS CORPORATION. "A New Nickel-Base Alloy for Resisting Metal Dusting Attack," Trans. Indian Inst. Met., Vol. 56, No. 3, 327 (2002).
52. T. M. POLLOCK and S. TIN. "Nickel-Based Superalloys for Advanced Turbine Engines: Chemistry, Microstructure, and Properties," JOURNAL OF PROPULSION AND POWER, Vol. 22, No. 2, (2006).
53. J. DONG, Z. BI, N. WANG, X. XIE, Z. WANG. "Structure Control of a New-Type High-Cr Superalloy," TMS (The Minerals, Metals & Materials Society), p 41-50 (2008).
54. SPECIAL METALS CORPORATION. "INCONEL alloy 617," http://www.specialmetals.com (current as of Jun. 16, 2014).
55. Y. NISHIYAMA et al. "Improved Metal Dusting Resistance of New Sumitomo 696 Ni-Base Alloy for Synthesis Gas Environments," Nitrogen and Syngas proceedings, 129-138 (2011).
56. Y. NISHIYAMA et al. "A prominent Ni-Cr-Si-Cu alloy resisting in metal dusting," NACE Corrosion Conference proceedings (2011).
57. M. ETTLER. "Einfluss von Reoxidationszyklen auf die Betriebsfestigkeit von anodengestützten Festoxid-Brennstoffzellen," Schriften des Forschungszentrums Jülich, Vol. 36 (2009).
58. H.-J. CHRIST. "Werkstoffeinsatz bei hohen Temperaturen," University script, Siegen, Germany (2013).
59. P. ROBERGE, Handbook of Corrosion Engineering, McGraw-Hill Professional (1999).
60. C. M. CHUN and T. RAMANARAYANAN. "Corrosion Resistance of a High-Silicon Alloy in Metal-Dusting Environments," Oxid Met (Oxidation of Metals) 67, p 215-234 (2007).
61. C. CHUN and T. RAMANARAYANAN. "Metal dusting resistant alumina forming coatings for syngas production," Corrosion Science 51, p 2770–2776 (2009).
62. H. J. GRABKE and M. SPIEGEL. "Occurrence of metal dusting– referring to failure cases," Materials and Corrosion 54, No. 10, p 799-804 (2003).
63. S. STRAUß and H. J. GRABKE. "Role of alloying elements in steels on metal dusting," Materials and Corrosion 49, p 321-327 (1998).

BUPT

64. L. MELO-MÁXIMO et al. "Performance of Cr oxide coatings on 304 steel against metal dusting," Surface and Coatings Technology 237, p 39-50 (2013).
65. J. ALVAREZ et al. "Role of Al oxide PVD coatings in the protection against metal dusting," Surface and Coatings Technology 204, Vol. 6-7, p 779-783 (2009).
66. H. GRÜNLING and R. BAUER. "The role of silicon in corrosion-resistant high temperature coatings," Thin Solid Films, 95, p 3-20, (1982).
67. E. LANG et al. "The effectiveness of vapour-deposited SiO_2 coatings in preventing carburization of incoloy 800H," Materials Science and Engineering, 88, p 37-45 (1987).
68. A. RAHMEL et al., Materials and Corrosion, Vol. 49, p.221 (1997).
69. DIN DEUTSCHES INSTITUT FÜR NORMUNG E. V. "Thermisches Spritzen – Spritzen und Einschmelzen von selbstfließenden Legierungen, DIN EN ISO 14920:2012-09," (2012).
70. F. OTSUBO et al. "Structure and phases in nickel-base self-fluxing alloy coating containing high chromium and boron," Journal of Thermal Spray Technology, Vol. 9 (1), p 107-113 (1999).
71. NEUE TECHNOLOGIE SYSTEMLÖSUNGEN GMBH. "Nickelbasis-Hartlegierungen," www.nt-systemloesungen.de (current as of Feb. 11, 2014).
72. S. BUYTOZ et al. "Microstructural and Wear Characteristics of High Velocity Oxygen Fuel (HVOF) Sprayed NiCrBSi–SiC Composite Coating on SAE 1030 Steel," Arab J Sci Eng (Arabian Journal for Science and Engineering), 38, Vol. 6, p 1481-1491 (2013).
73. A. MOLNÁR et al. "Hardness test and microstructure analysis of NiCrBSi sprayed, laser remelted coatings," Production Processes and Systems, vol. 6., No. 1. pp. 35-46. (2013).
74. FIEHL + CREMER GMBH + CO. KG. "NiCrBSi," http://nicrbsi.de (current as of Dec. 21, 2013).
75. DOROZHKIN, N. N., KUZNETZOV, N. N. "Plasma spraying of self-fluxing alloys onto heated substrates," Poroshkovaya Metallurgiya, No. 12 (144), p 51-56 (1975).
76. Š. HOUDKOVÁ et al. "Properties of NiCrBSi coating, as sprayed and remelted by different technologies," Surface and Coatings Technology, vol. 253, p 14–26 (2014).
77. Š. HOUDKOVÁ et al. "Comparison of NiCrBSi coatings, HVOP sprayed, re-melted by flame and by high-power laser," Metal conference proceedings (2013).
78. POLEMA JOINT STOCK COMPANY. "Nickel and Fe self-fluxing alloys for coatings," http://www.polema-rus.com (current as of Jan. 16, 2014).
79. SULZER LTD. "Thermal Spray Materials Guide," http://www.sianco.com (current as of May. 23, 2014).
80. R. GONZÁLEZ et al. "Microstructural study of NiCrBSi coatings obtained by different processes," Wear 263, Vol. 1-6, p 619-624 (2007).
81. YU. S. BORISOV, I. N. GORBATOV. "Production and structure of flame-sprayed coatings based on Ni-Ci-B-Si alloys," Powder Metallurgical Materials, Parts, and Coatings (1986).
82. C. L. OU et al. "Brazing of 422 stainless steel using the AWS classification BNi-2 Braze alloy," J Mater Sci (Journal of Materials Science), 41, Vol. 19, p 6353-6361 (2006).
83. R. M. MRDAK. "Microstructure and mechanical properties of nickel - chrome - bor - silicon laser produced by the atmospheric plasma spray process," Vojnotehnicki Glasnik/Military Technical Courier, Vol. LX, No. 1, p 183-200 (2012).

BUPT

84. I. HEMMATI et al. "Electron Microscopy Characterization of Ni-Cr-B-Si-C Laser Deposited Coatings," Microsc Microanal (Microscopy and Microanalysis), 19, vol. 1, p 120-131 (2013).
85. T. LIYANAGE et al. "Influence of alloy chemistry on microstructure and properties in NiCrBSi overlay coatings deposited by plasma transferred arc welding (PTAW)," Surface and Coatings Technology, 205, vol. 3, p 759-765 (2010).
86. V. V. RODIONOV et al. "Change of the structure of wear resistant self-fluxing nickel base alloys in heat treatment," Poroshkovaya Metallurgiya, No. 8 (332), p 46-49 (1991).
87. A. DUDEK. "The change of NiCrBSi alloys' phase composition after plasma spraying," Archives of Foundry Engineering, Vol. 8 (2008).
88. H.-J. KIMA et al. "Assessment of wear performance of flame sprayed and fused Ni-based coatings," Surface and Coatings Technology, 172, p 262-269 (2003).
89. N. SERRES et al. "Microstructures of metallic NiCrBSi coatings manufactured via hybrid plasma spray and in situ laser remelting process," J Therm Spray Tech (Journal of Thermal Spray Technology), 20, vol. 1-2, p 336-343 (2011).
90. R. C. SCHUELER. "Hydrocarbon Processing," 73 (1972).
91. DREXEL. "EDS system," www.crf.coe.drexel.edu (current as of Jul. 31, 2014).
92. H.-J. BARGEL. "Werkstoffkunde," handbook, ISBN 3540261079 (2005).
93. PHILIPS INNOVATION SERVICES. "X-Ray Diffraction (XRD)," http://www.innovationservices.philips.com (current as of Mar. 16, 2014).
94. F. RICHTER. "Über die Silicierung von Eisen ein Beitrag zum Aufbau der Silicierungsschichten," Doctoral Thesis, University Wien (1948).
95. AMETEK. "Schema SpectromaXx," http://www.spectro.de/pages/d/p010212_spectromaxx_broschueren.htm (current as of Jan. 01, 2014).
96. J. SCHLIRF. "Thermische Analyse: Was ist thermische Analyse?," script University Hagen (current as of Jul. 22, 2014).
97. J. DICKMANN. "Aufbau eines Messsystems zur Erfassung transienter Temperatursignale beim Laserstrahlhartlöten," Bachelor Thesis, Westphalian University Gelsenkirchen (Germany) (2010).
98. ONE OMEGA DRIVE. "Thermocouple introduction and theory," http://www.omega.com/temperature/z/pdf/z021-032.pdf (current as of Aug. 16, 2014).
99. AIR LIQUIDE DEUTSCHLAND GMBH. "Equipment und Zubehör zur Gasnachreinigung," www.airliquide.de (current as of Apr. 01, 2014).
100. EAGLE ALLOY CORPORATION. "Kovar," www.eaglealloys.com (current as of Apr. 22, 2014).
101. FLAME SPRAY TECHNOLOGIES. "Flame Powder Spraying," www.fst.nl (current as of Nov. 08, 2013).
102. SULZER OERLIKON LTD. "Material Product Data Sheet," (2012).
103. ASM International (Ed.), Alloy Phase Diagrams: Volume 3, handbook, ISBN 0-87170-377-7, ASM International, Ohio (2007).
104. J. ZHANG et al. "Oxidation, carburisation and metal dusting of 304 stainless steel in CO/CO_2 and $CO/H_2/H_2O$ gas mixtures," Corrosion Science, 50, vol. 11, p 3107-3115 (2008).

BUPT

List of Publications

[1] Carsten Strübbe, Viorel-Aurel Şerban, "Prevention and controlling of metal dusting", Scientific Bulletin of the Politehnica University Timisoara, Romania, Mechanical Section, vol. 57 (71), ISSN 1224 – 6077, Iss. 1, 2012

[2] Carsten Strübbe, Viorel-Aurel Şerban, Gabriela Marginean, Waltraut Brandl, "High temperature thermocyclic behavior of a preoxidized Ni based superalloys 601 and HVOF sprayed Ni-Cr-B-Si and CoNiCrAlY coatings", Nanocon Conference, Brno, Czech Republic, Thomson Reuters, ISBN 978-80-87294-32-1, 2012

[3] Carsten Strübbe, Gabriela Marginean, Viorel-Aurel Şerban, Waltraut Brandl, "High temperature behavior of Ni-Cr-B-Si-coatings thermo cycled at 600°C, 700°C and 800°C", Metal Conference, Brno, Czech Republic, 2013

[4] Carsten Strübbe, Gabriela Marginean, Viorel-Aurel Şerban, "Influence of the Si-Content on the High Temperature Oxidation Behaviour of NiCrBSi-Coatings", Solid State Phenomena Vol. 216, p. 79-84, Trans Techn Publications, Switzerland, 2014

Appendix

Surface morphology of the exposed samples 15E after 1000 hours

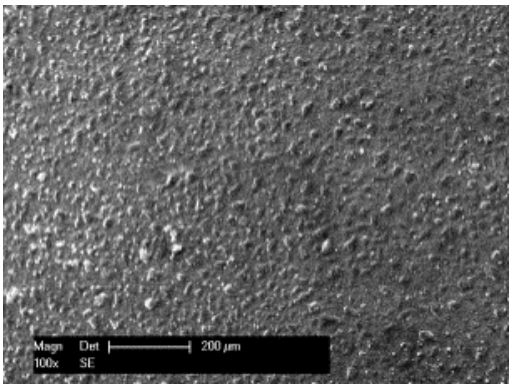

Thermal sprayed and remelted with flame

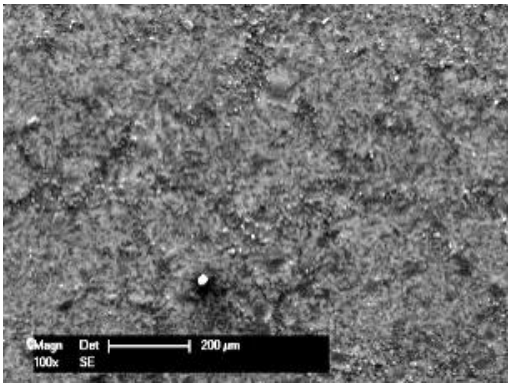

Vacuum melted

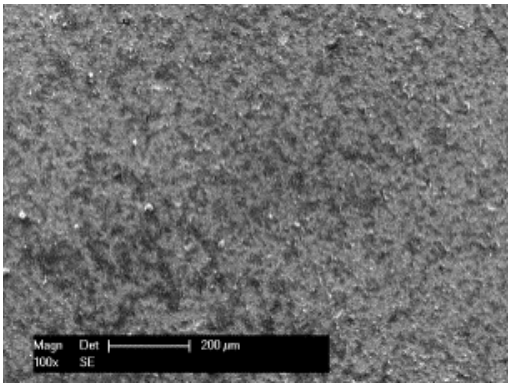

Inductively melted

Surface morphology of the exposed samples 18C after 1000 hours

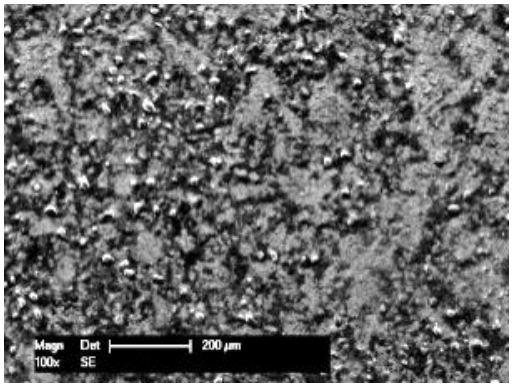

Thermal sprayed and remelted with flame

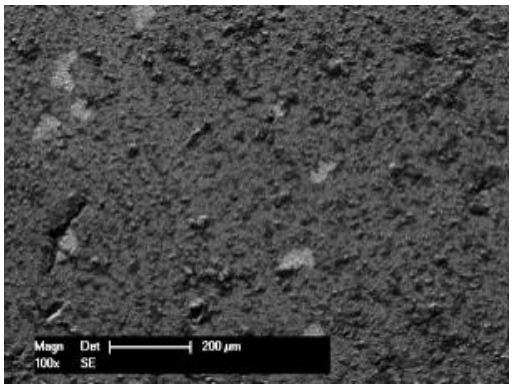

Vacuum melted

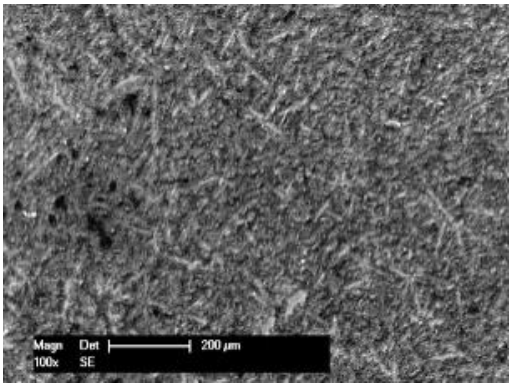

Inductively melted

Surface morphology of the exposed samples 19E after 1000 hours

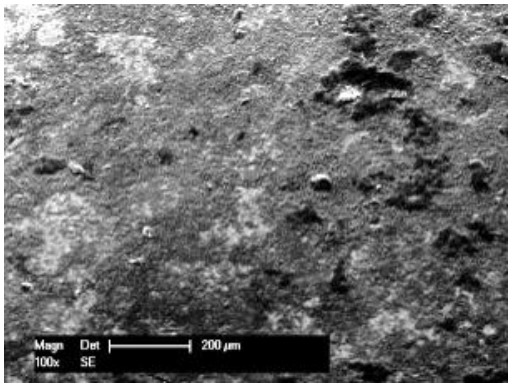

Thermal sprayed and remelted with flame

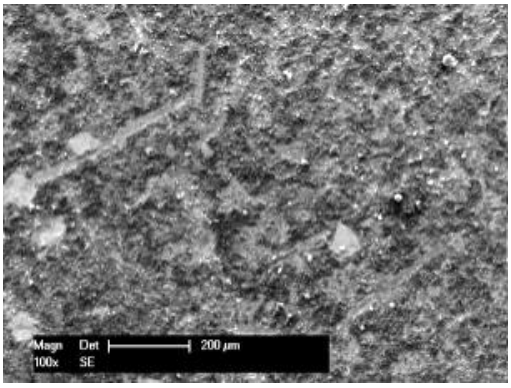

Vacuum melted

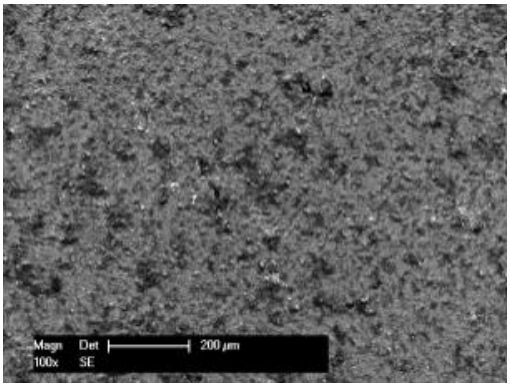

Inductively melted

Cross section SEM micrograph of the exposed samples 15E after 500 hours

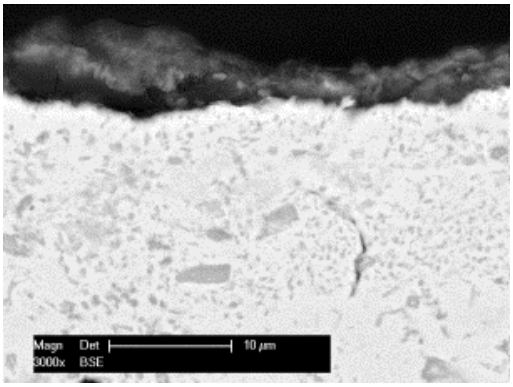

Thermal sprayed and remelted with flame

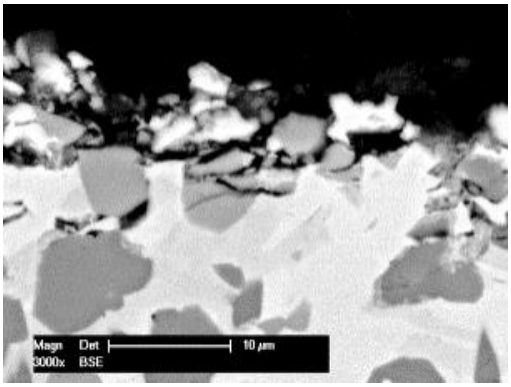

Vacuum melted

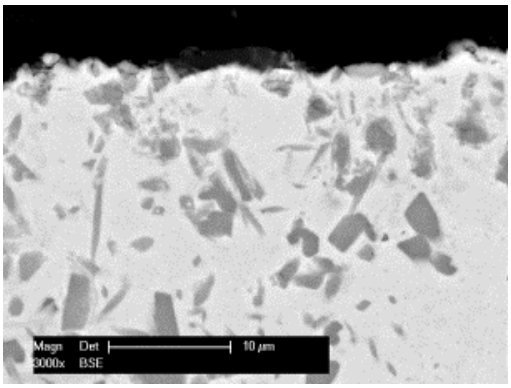

Inductively melted

Cross section SEM micrograph of the exposed samples 18C after 500 hours

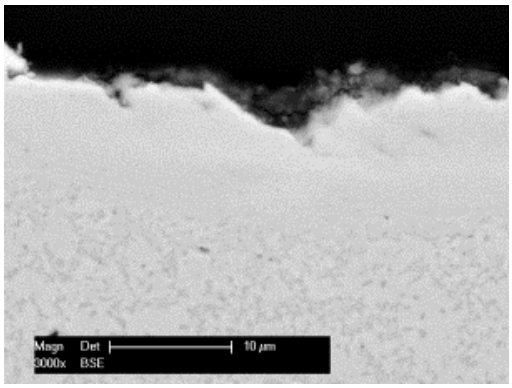

Thermal sprayed and remelted with flame

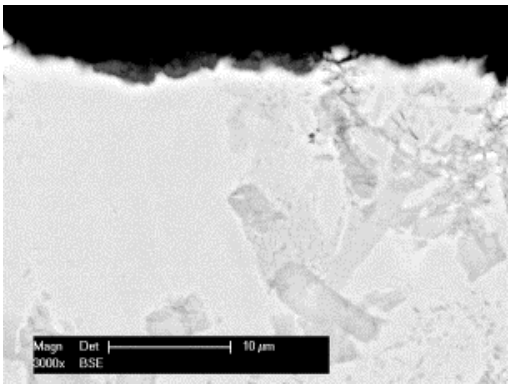

Vacuum melted

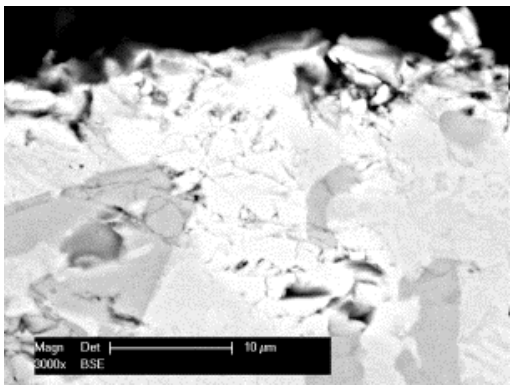

Inductively melted

Cross section SEM micrograph of the exposed samples 19E after 500 hours

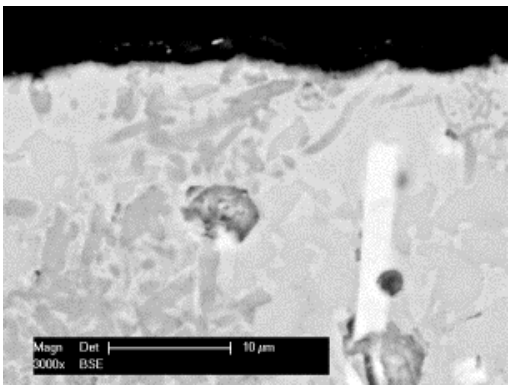

Thermal sprayed and remelted with flame

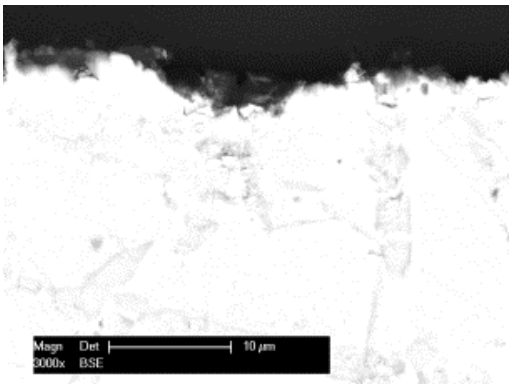

Vacuum melted

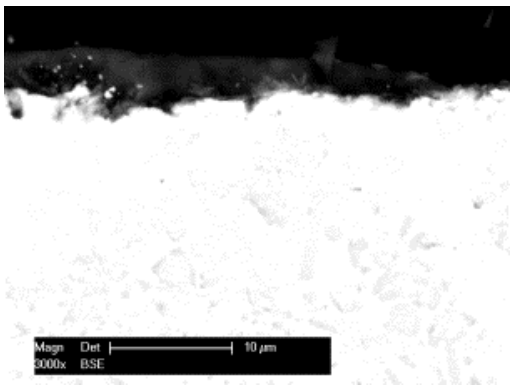

Inductively melted

Cross section SEM micrograph of the exposed samples 15E after 1000 hours

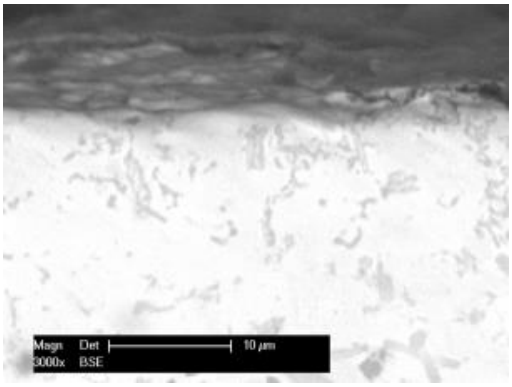

Thermal sprayed and remelted with flame

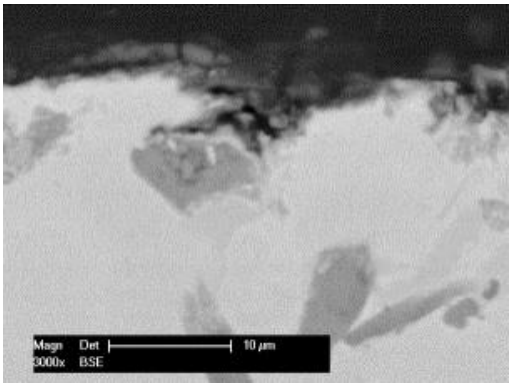

Vacuum melted

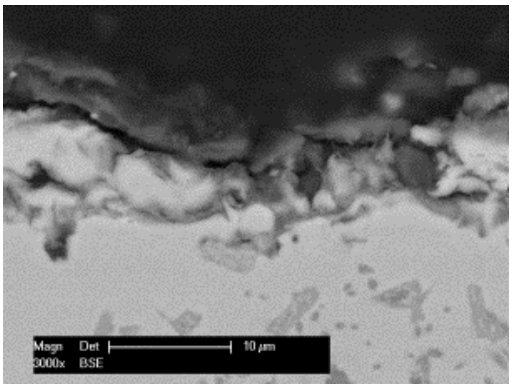

Inductively melted

Cross section SEM micrograph of the exposed samples 18C after 1000 hours

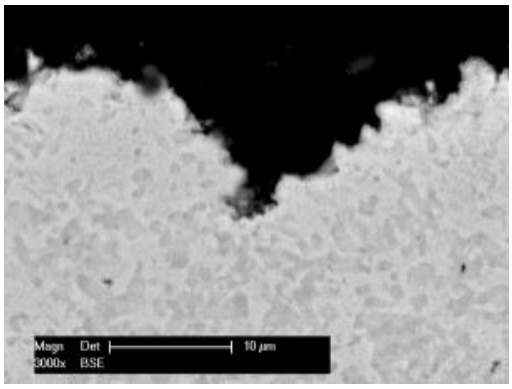

Thermal sprayed and remelted with flame

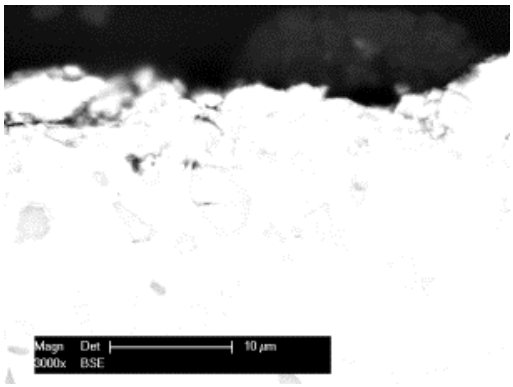

Vacuum melted

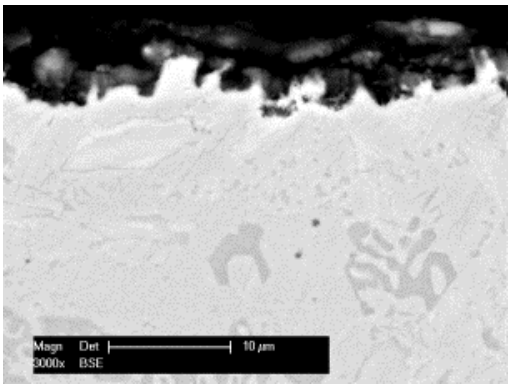

Inductively melted

Cross section SEM micrograph of the exposed samples 19E after 1000 hours

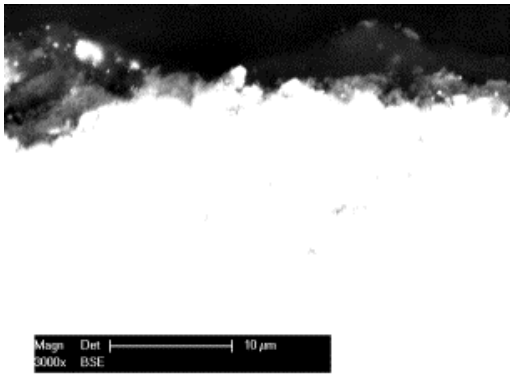

Thermal sprayed and remelted with flame

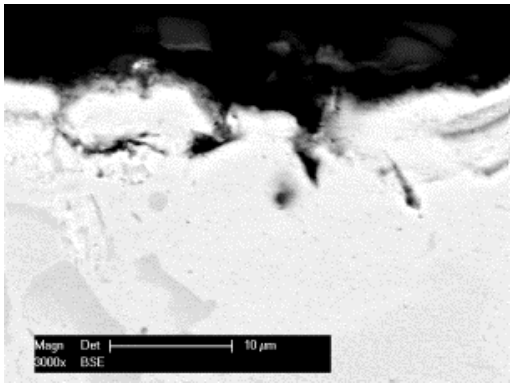

Vacuum melted

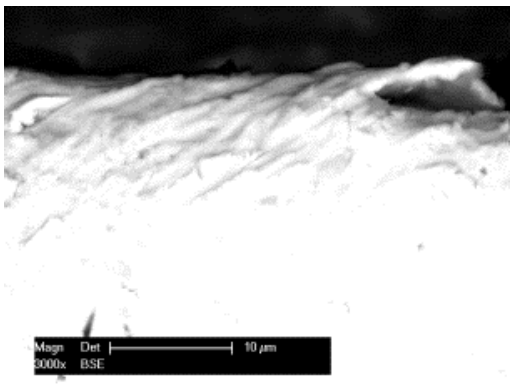

Inductively melted

Colour etching results of the exposed samples 15E after 1000 hours

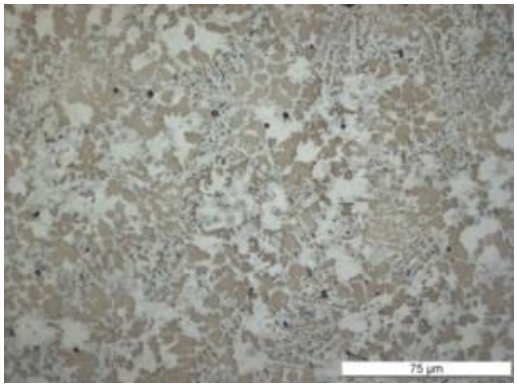

Thermal sprayed and remelted with flame

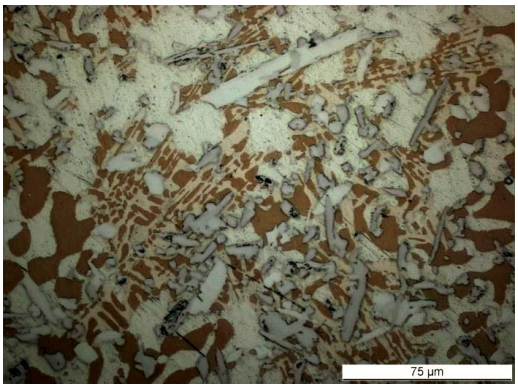

Vacuum melted

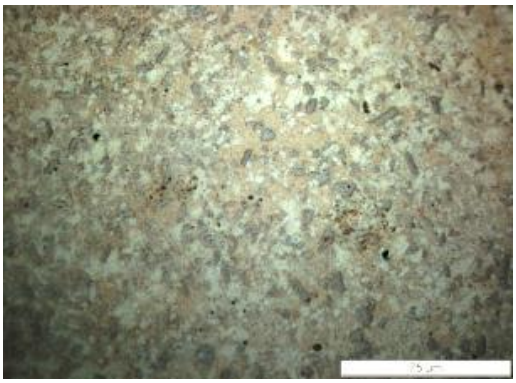

Inductively melted

BUPT

Colour etching results of the exposed samples 18C after 1000 hours

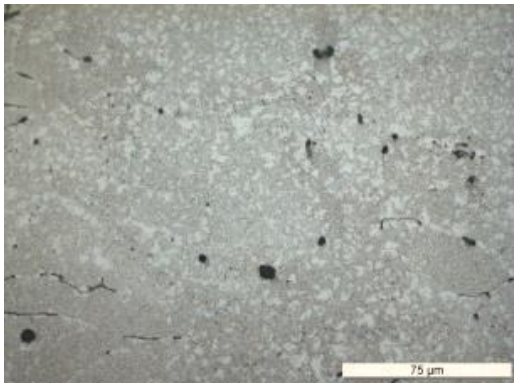

Thermal sprayed and remelted with flame

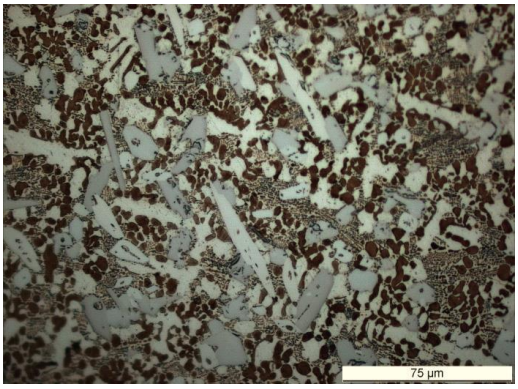

Vacuum melted

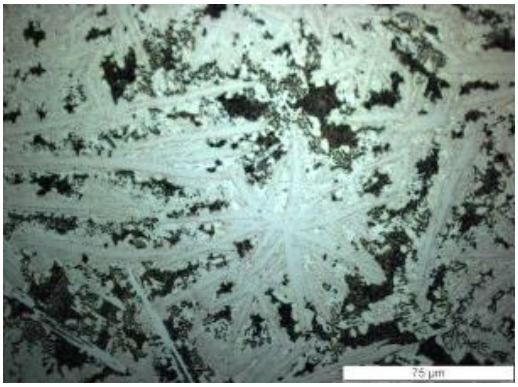

Inductively melted

Colour etching results of the exposed samples 19E after 1000 hours

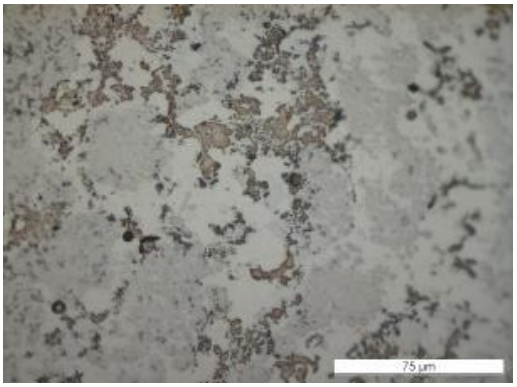

Thermal sprayed and remelted with flame

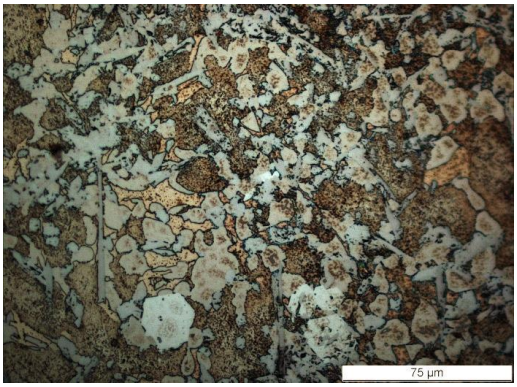

Vacuum melted

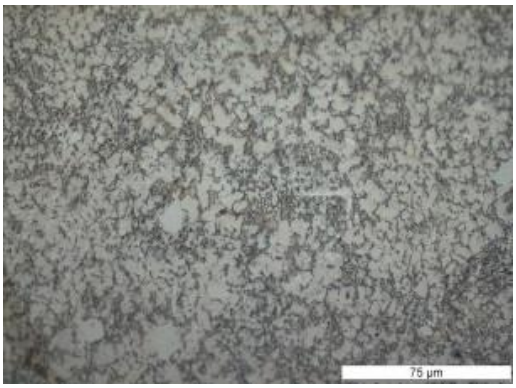

Inductively melted

BUPT

Curriculum Vitae

PERSONAL DETAILS

NAME	Carsten Strübbe Son of Sigrid Strübbe (Broschk) and Norbert Strübbe
ADDRESS	Vehrenbergstrasse 127, 45968 Gladbeck, Germany
DATE OF BIRTH	08/03/1977
PLACE OF BIRTH	Gelsenkirchen, Germany
NATIONALITY	Germany
E-MAIL	c.struebbe@hotmail.de
MARITAL STATUS	Married, 1 child

WORK EXPERIENCE

11/08 – Present	Scientific assistant at the Department of Materials Science and Testing of Materials, University of Applied Sciences Gelsenkirchen, Germany
01/2000 – 07/2001	Skilled worker in assembly line production and quality control at the company Adam OPEL AG in Bochum, Germany

EDUCATION AND TRAINING

02/2015	Completion of the doctoral degree
10/2010 – 02/2015	PhD student at the Department of Materials Science and Engineering, Faculty of Mechanical Engineering, Politehnica University of Timisoara, Romania in cooperation with Westphalian University of Applied Sciences Gelsenkirchen, Germany
07/2010	Master of Science Degree
10/2008 – 07/2010	Master student at the Faculty of Mechanical Engineering, Politehnica University of Timisoara, Romania
10/2008	Diplom-Engineer (FH) Degree
09/2002 – 10/2008	Student at the Faculty of Mechanical Engineering, University of Applied Sciences Gelsenkirchen, Germany
06/2002	Graduation: Technical diploma (vocational baccalaureate diploma)
07/2001 – 06/2002	Student at the technical college BTG in Gelsenkirchen, Germany
01/2000	Graduation: skilled worker's certificate (cutting machine operator)
09/1996 – 01/2000	Apprentice at the company Adam OPEL AG in Bochum, Germany

LANGUAGE SKILLS

German	native speaker
English	fluent (spoken and written)

BUPT